

**CIMREx**

**CIMR Airborne Arctic campaign**

**Deliverable 4**

# Final Report

---

Intercomparison of airborne observations with satellite passive microwave and infrared camera measurements

**ESTEC Contract No:** 4000125503/18/NL/FF/gp

Issue / Revision: 1 / 0

Date: 4 September 2019

Prepared by:

Gunnar SPREEN, Raul SCARLAT, Marcus HUNTEMANN  
University of Bremen

Juha LEMMETYINEN  
Finnish Meteorological Institute, Finland

René FORSBERG and Andreas STOKHOLM  
National Space Institute, Denmark

Samuli NYMAN  
Aalto University, Finland

Sampo SALO  
Harp Technologies Ltd., Finland



DTU Space  
National Space Institute



*This page is intentionally left blank.*

## ESA STUDY CONTRACT REPORT

ESTEC Contract No: <b>4000125503/18/NL/FF/gp</b>	Subject: <b>CIMR Airborne Arctic campaign</b>		Contractor: FMI
ESA CR ( )No:	Star Code:	No of volumes: 1 This is volume no: 1	Contractor's Ref:
<p><b>ABSTRACT:</b></p> <p>The airborne campaign CIMREx was initiated by ESA to support the EU Copernicus High Priority Polar Candidate Mission, Copernicus Imaging Microwave Radiometer (CIMR), to sample the sea ice microwave emissions from various sea ice regimes around Svalbard and Greenland. The measurements were carried out with the HUTRAD 2.0 radiometer, refurbished for the purpose of the campaign. HUTRAD measured the brightness temperature from the sea ice at 6.8, 10.65 and 18.7 GHz at vertical and horizontal polarizations, providing basic information on the ability for high-resolution measurements of sea ice concentration and related snow/ice properties for the future CIMR satellite. Refurbishment of HUTRAD was performed as a part of the CIMREx activities by Harp Technologies Ltd. In addition to the side-looking HUTRAD passive microwave measurements, also infrared and visual imaging was carried out, along with precise aircraft navigation with geodetic GPS and inertial navigation units.</p> <p>The CIMREx campaign took place between February 28-March 11, 2019. The first data were collected during initial transitions from Akureyri, Iceland, via Greenland, to the main campaign site at Svalbard. Three dedicated data collection flights were carried out around Svalbard on March 7 and 8.</p>			
<p>The work described in this report was done under ESA Contract. Responsibility for the contents resides in the author or organisation that prepared it.</p>			
<p>Authors: Gunnar SPREEN, Raul SCARLAT, Marcus HUNTEMANN, Juha LEMMETYINEN, René FORSBERG, Andreas STOKHOLM, Samuli NYMAN and Sampo SALO.</p>			
ESA Study Manager: Michael Kern		ESA BUDGET HEADING	

## Document change log

Issue/ Revision	Date	Observations
1.0	04 September 2019	1 <sup>st</sup> issue

*This page is intentionally left blank.*

# Table of Contents

<b>1</b>	<b>INTRODUCTION</b>	<b>7</b>
<b>2</b>	<b>METHODS AND DATA</b>	<b>9</b>
<b>2.1</b>	<b>METHODS</b>	<b>9</b>
2.1.1	AIRBORNE MEASUREMENTS	9
2.1.2	COMPARISON WITH SATELLITE Tb MEASUREMENTS	10
2.1.3	ANALYSIS OF COMBINED HUTRAD Tb MEASUREMENTS AND THERMAL CAMERA DATA	11
<b>2.2</b>	<b>DATA</b>	<b>12</b>
2.2.1	AMSR2	12
2.2.2	CIMR	12
2.2.3	HUTRAD	13
2.2.4	THERMAL CAMERA	14
<b>3</b>	<b>ANALYSIS OF HUTRAD MEASUREMENTS</b>	<b>15</b>
<b>3.1</b>	<b>HUTRAD CALIBRATION UNCERTAINTY</b>	<b>15</b>
3.1.1	CALIBRATION PROCEDURE	15
3.1.2	EFFECT OF PHYSICAL TEMPERATURE	17
3.1.3	ESTIMATION OF ABSOLUTE ACCURACY	20
<b>3.2</b>	<b>AMSR2 vs HUTRAD Tbs - FOR ALL SCIENCE FLIGHTS</b>	<b>21</b>
3.2.1	EXPLANATION OF GRAPHIC	23
3.2.2	COMMENTARY AND INTERPRETATION	23
<b>3.3</b>	<b>AMSR2 vs HUTRAD Tbs - FOR ALL TRANSFER FLIGHTS</b>	<b>24</b>
3.3.1	EXPLANATION OF GRAPHIC	25
3.3.2	COMMENTARY AND INTERPRETATION	26
<b>3.4</b>	<b>COMPARISON OF HUTRAD OBSERVATIONS FROM FORWARD AND BACKWARD TRANSECTS</b>	<b>27</b>
<b>3.5</b>	<b>USING HUTRAD MEASUREMENTS TOGETHER WITH THERMAL CAMERA DATA</b>	<b>30</b>
3.5.1	IR BASED SURFACE TYPE CLASSIFICATION AND COMPARISON WITH HUTRAD BRIGHTNESS TEMPERATURES.	31
3.5.2	HUTRAD Tbs COMPARED WITH IR BASED ICE SURFACE TEMPERATURE	33
3.5.3	MODEL SUPPORT FOR INTERPRETATION OF HUTRAD DATA COMPARED TO THERMAL IR DATA	35
3.5.4	CASE STUDY - HUTRAD Tbs OF THIN ICE	37
3.5.5	CONCLUSIONS ON COMBINATION OF HUTRAD AND INFRARED CAMERA	38
<b>4</b>	<b>CONCLUSIONS AND RECOMMENDATIONS</b>	<b>40</b>
<b>5</b>	<b>REFERENCES</b>	<b>43</b>

# 1 Introduction

This document provides the final report of the ESA project Copernicus Imaging Microwave Radiometer Arctic Airborne campaign (CIMREx; 4000125503/18/NL/FF/gp).

CIMREx was designed to support the EU Copernicus High Priority Polar Candidate Mission, Copernicus Imaging Microwave Radiometer (CIMR), to sample the sea ice microwave emissions from various sea ice regimes around Svalbard and Greenland. The measurements were carried out with the newly refurbished Finnish HUTRAD 2.0 radiometer, measuring the brightness temperature from the sea ice at various frequencies (6.8, 10.65 and 18.7 GHz) at vertical and horizontal polarizations, providing basic information on the ability for high-resolution measurements of sea ice concentration and related snow/ice properties for the future CIMR satellite. Refurbishment of HUTRAD was performed as a part of the CIMREx activities by Harp Technologies Ltd. In addition to the side-looking HUTRAD passive microwave measurements, also infrared and visual imaging was carried out, along with precise aircraft navigation with geodetic GPS and inertial navigation units.

The CIMREx campaign took place between February 28-March 11, 2019. The first data were collected during initial transitions from Akureyri, Iceland, via Greenland, to the main campaign site at Svalbard. Three dedicated data collection flights were carried out around Svalbard on March 7 and 8. The campaign ended with a transfer flight back to Akureyri on March 10.

Previous deliverable documents, which are included as an appendix to this report, include

- **Appendix 1: System readiness and test report (Uusitalo et al., 2019):** the document gives details on HUTRAD refurbishment for CIMREx including performance of the refurbished measured in laboratory conditions
- **Appendix 2: Campaign Implementation Plan (Lemmetyinen et al., 2019):** the document provides the campaign plan, including plans for installation, test areas, logistics, instrument calibration etc.
- **Appendix 3: Data Acquisition Report (Forsberg et al., 2019):** the document gives the details of the conducted airborne experiment, including applied instrumentation, conducted flight operations, data formats, aspects related to ground operations (mainly radiometer calibrations).

This final report provides an analysis of the data collected during the campaign. The collected airborne radiometer measurements are compared with collocated AMSR-2 footprints for each common channel. The supporting infrared (IR) camera measurements helped to identify

different ice surface types. The HUTRAD radiometer measurements were compared for these surface types.

The document contains:

- An overview of the objective of the study, which, in brief, is to sample the sea ice microwave emissions from various sea ice regimes around Svalbard and Greenland
- A comparison of the airborne measured brightness temperatures with corresponding AMSR2 satellite measurements in order to understand differences and sub-footprint scale variability of the AMSR2 data from the HUTRAD 2.0 instrument.
- An analysis of HUTRAD 2.0 calibration uncertainties during the campaign
- An analysis of the transects flown in forward and backward direction.
- An analysis of the measured brightness temperatures combined with infrared data which allows for identifying different sea ice types and the corresponding passive microwave brightness temperatures.
- Conclusions and recommendations

## 2 Methods and Data

### 2.1 Methods

#### 2.1.1 Airborne measurements

Instrument installation began on Akureyri airport on February 28. After installation and ground performance checks of all instruments, the system was ready for a test flight on March 3. During the test flight, in particular the capability of the HUTRAD system to maintain receiver internal temperatures was assessed. Transfer to Svalbard was performed in three legs from Mar 4 to Mar 5. After bad weather on Mar 6, two science flights (test sites B and C) were sampled on Mar 7, with a landing for refuelling and calibration between the flights. The last designated test site (test site D) was sampled on Mar 8. After prohibitive flying weather on Mar 9, the transfer flight back to Akureyri (two legs) was done on Mar 10.

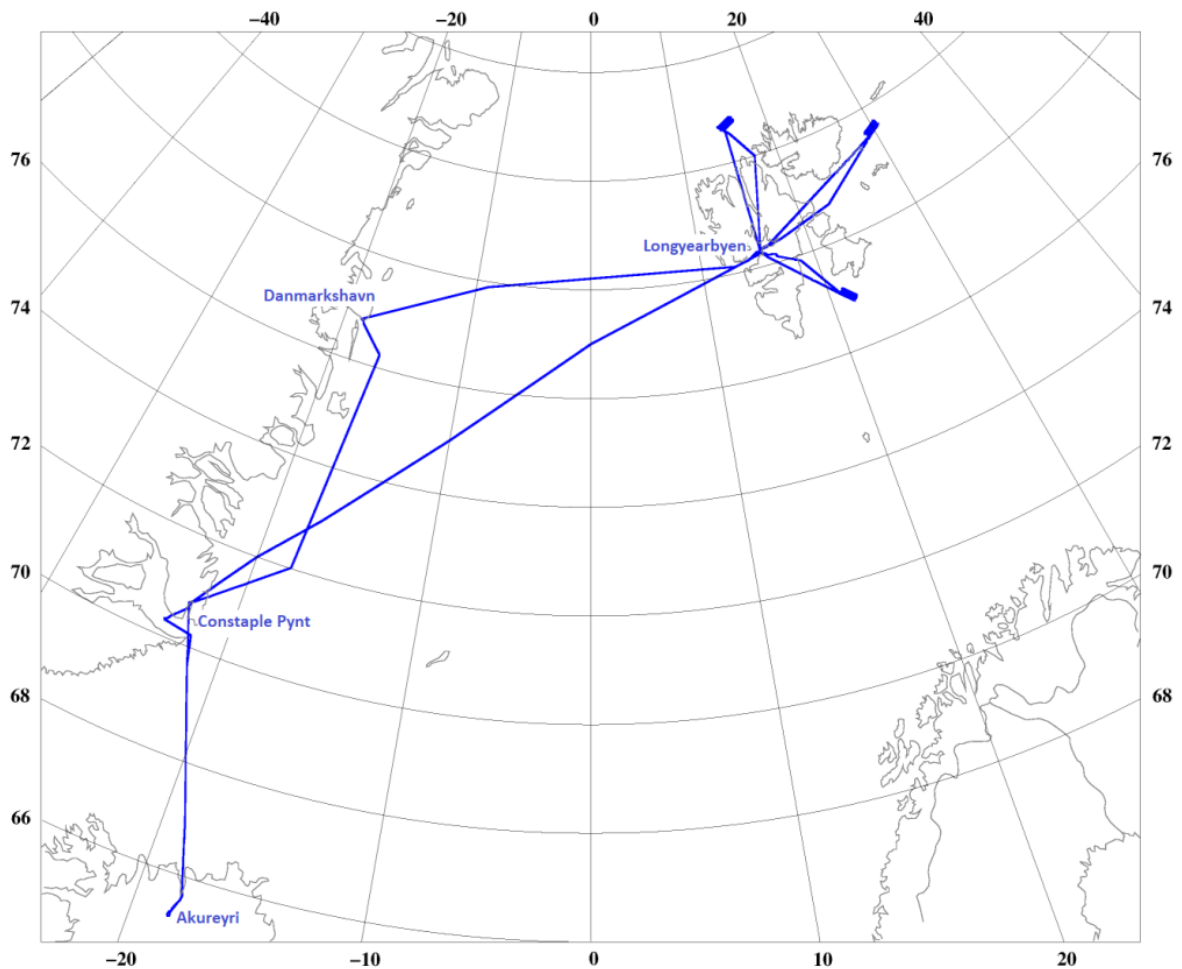


**Figure 1:** CIMREX-2019 flight tracks.

**Figure 1** depicts all flight transects including the transfer flight to and from Svalbard. An original plan to make more profiles across the NE Greenland marginal ice zone had to be modified, due to daylight constraints for VFR flights to Danmarkshavn weather station (DMH). Also, for the return flight from Svalbard to Constable Point airport (CNP), no measurements were possible due to the extremely long transit, necessitated by recent

Schengen border control issues. Measurements were resumed for the last leg from Constable Point to Akureyri.

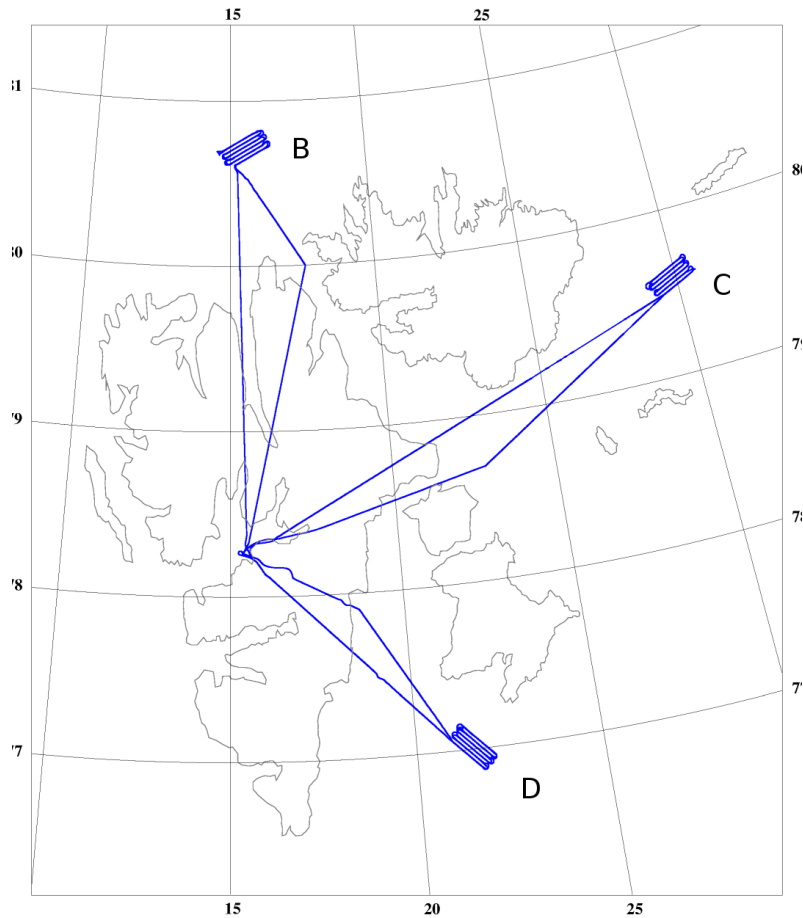


**Figure 2:** Svalbard flight tracks March 7-8. The test sites were labeled B, C and D.

**Figure 2** shows the tracks sampled during the three main science flights. The science flights had the primary objectives to collect relatively low (320 m) profiles over sea ice and higher level (1050 m) profiles in dedicated “mow-the-lawn” patterns, where an equidistant  $\sim 20$  km long line pattern were flown both in “forward” and “backward” directions, with a line spacing ( $\sim 2.5$  km) designed to give optimal coverage of brightness temperature variations over the pattern. The mow-the-lawn areas were selected to have a different degree of open water and floes of first year (FY) or multi-year (MY) ice.

For a more detailed account of the measurement flights, instrumentation, collected data including data formats etc, consult the Data Acquisition Report (Forsberg et al., 2019)

### 2.1.2 Comparison with satellite Tb measurements

In order to understand the small scale, sub-satellite footprint variability and determine the accuracy of the HUTRAD Tb measurements, these were compared to satellite observations at the same channel frequencies and polarization modes. The airborne measurements from the three science flights as well as the initial transfer flights was compared with collocated Tb observations from AMSR2 L1B swath data. The airborne data including aircraft position parameters are consolidated together with the collocated AMSR2

measurements, land flags, distance and time stamps into datafiles corresponding to each science and transfer flight for further analysis.

For each HUTRAD data point the closest AMSR2 swath pixel is found. Given the large footprint of satellite measurements, particularly at the HUTRAD instrument frequencies, one AMSR2 pixel can correspond to a large number of airborne observations. All three science flights as well as the transfer flight measurements were collocated with the corresponding satellite data. The maximum allowed time difference for the collocation is 6 hours but the average time difference for all science flights is around 2.6 hours while for the transfer flights it is 3 hours. In order to find a corresponding satellite footprint no hard limit was set on the maximum spatial difference; the closest satellite pixel being always chosen. The mean distance for the science flights is around 37 km while for the transfer flights this mean goes down to 11 km. This means that each HUTRAD measurement has an associated satellite observation. This is the dataset made available together with this study. However, for the analysis presented in this document much more rigid conditions for the HUTRAD to AMSR2 correspondence are used. The following filters are applied to the data:

- A land mask based on the GSHHS (Global Self-consistent, Hierarchical, High-resolution Geography Database; <https://www.soest.hawaii.edu/pwessel/gshhg/>) coastline polygons is used to filter out the land pixels from the airborne data.
- Aircraft movement can be a factor that influences the accuracy of the radiometer measurements as the footprint is influenced by the viewing angle. The aircraft roll value is used to flag data that could be corrupted by such maneuvers. For the data analysis only pixels with a roll value below 2° are used.
- In order to exclude data points which are too far away from the satellite footprint, for each frequency a distance filter is implemented. All pixels which are farther away than the 35, 24 and 14 km, respectively, from the center coordinates of an AMSR2 6.9, 10.65 and 18.7 GHz footprint, are excluded from the analysis. On average for the science flights the HUTRAD pixels included in the analysis are within 2.5 km of the closest AMSR2 footprint, i.e. completely within the AMSR2 footprint.
- For the analysis of the science flights data, only the mow-the-lawn pattern measurements are considered. For the transfer flights, an analysis for all data and one specifically for observations taken over open water are performed.

These filtering criteria are selected in order to preserve as much of the airborne data for analysis as possible. Depending on the desired accuracy, more strict filters could be used based on the spatial and temporal distance between the airborne and the satellite measurement, aircraft flight parameters (roll, pitch, yaw and altitude) or surface conditions based on ancillary data (from the thermal camera for example). All these parameters are stored in the data output file and are available for further analysis.

### 2.1.3 Analysis of combined HUTRAD Tb measurements and thermal camera data

Thermal images (IR) were collected by an Infratec VarioCAM HDx collocated with the HUTRAD measurements. To compare IR with the HUTRAD data, first the IR images were reprojected on Earth based on the used incidence angle (nominal 55°, however adapted here to best fit the data). Within the projected IR images the center of the HUTRAD footprints were determined by a maximum correlation analysis. After the best

geometrical setting was identified, all IR data was processed together with the HUTRAD data with a 2 second time resolution.

## 2.2 Data

### 2.2.1 AMSR2

The JAXA satellite "Shizuku" (GCOM-W1) that carries AMSR2 has been launched successfully on May 18, 2012. These data are widely used in sea ice research and for navigation within sea ice. For example, the University of Bremen is providing sea ice concentration maps from these data since 2 July 2012 ([www.seaice.uni-bremen.de](http://www.seaice.uni-bremen.de)) and for AMSR-E from from June 2002 to October 2011.

For comparing with HUTRAD measurements, individual swath files of the AMSR2 L1B product were used. Level 1B (L1B) products contain brightness temperatures which are converted from the Level 1A raw observation count values.

### 2.2.2 CIMR

Copernicus is a European system for monitoring the Earth. It includes earth observation satellites (notably the Sentinel series developed by ESA), ground-based measurements and services to processes data to provide users with reliable and up-to-date information through a set of Copernicus Services related to environmental and security issues.

The candidate missions for future Sentinel satellites consider with high priority the inclusion of the global multi-frequency imaging microwave radiometry CIMR, with a focus on high-latitude regions in support of European Union Arctic Policy. It is part of the expansion of the current Copernicus Space Component (CSC) capabilities described in the CSC Long Term Scenario to address the User Requirements expressed by the European Commission. The proposed channel structure of the CIMR instrument as well as a comparison with other passive microwave radiometers is shown in **Figure 3**.

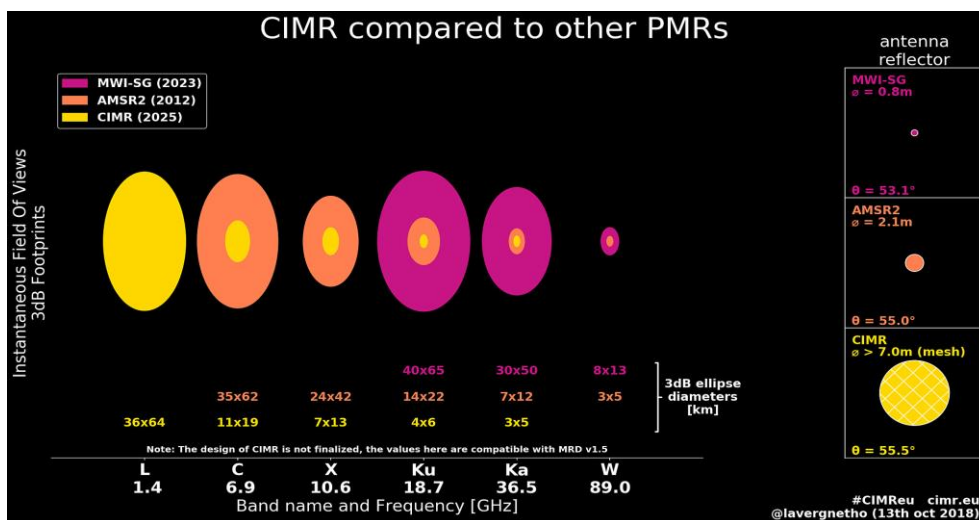


**Figure 3:** Channel structure of the CIMR instrument compared to existing passive microwave radiometers (PMRs). Original figure form Lavergne (2018).

The aim of a Copernicus Imaging Microwave Radiometry (CIMR) Mission is to provide high-spatial resolution microwave imaging radiometric measurements and derived products with global coverage and sub-daily revisit in the Polar regions to address Copernicus user needs. The primary objectives of the CIMR mission are to:

1. measure all-weather Sea Ice Concentration (SIC) and Sea Ice Extent (SIE) at a spatial resolution of <5 km, with a standard uncertainty of <5 %, and sub-daily coverage of the Polar Regions and daily coverage of Adjacent Seas
2. measure all-weather Sea Surface Temperature (SST) at an effective spatial resolution of ~15 km, with a standard uncertainty of ~0.2 K and focusing on sub-daily coverage of Polar Regions and daily coverage of Adjacent Seas
3. ensure improved continuity of AMSR-type capability in synergy with other missions (e.g. MetOp-SG(B))

### 2.2.3 HUTRAD

The HUTRAD2.0 instrument was refurbished in Task 1 of CIMREx. For the campaign (Uusitalo et al., 2019), the refurbished system with receivers at 6.8, 10.65 and 18.7 GHz was installed in the cargo compartment of a de Havilland DHC-6 Twin Otter aircraft, with radiometer aperture facing outward from the left side cargo door. The nominal incidence angle at level flight was 55° from nadir. The installation, as well as on-ground performance verification of the system, was performed in the premises of Norlandair in Akureyri, Iceland. The main characteristics of the HUTRAD instrument are described in **Table 1**.

**Table 1:** Main characteristics of the refurbished HUTRAD2.0 system.

Frequency (GHz)	6.825		10.65		18.7	
	V	H	V	H	V	H
Bandwidth (MHz)	310	310	120	120	750	720
Sensitivity <sup>1)</sup> (K)	0.11	0.09	0.22	0.24	0.1	0.09
$\theta_{3\text{dB}}$ (deg) <sup>2)</sup>	14.8	11.2	9.1	6.6	5.2	3.9
$\theta_{9\text{dB}}$ (deg) <sup>2)</sup>	25.0	18.5	15.1	10.8	8.6	6.4

1) Theoretical radiometric resolution for Dicke-type radiometer with 300 K antenna temperature and 0.5s integration time

2) Simulated beamwidth with refurbished antennas.

### 2.2.4 Thermal camera

A thermographic Infratec VarioCAM HDx head 600 camera was installed in the bay under the HUTRAD radiometer system. The VarioCAM HDx 600 is based on an uncooled microbolometer FPA detector with 640 × 480 IR pixels. It has a wide temperature measuring range that makes it suitable for universal measuring and monitoring tasks, including aerial thermography. It has an industrial-grade light metal housing (IP67), which makes operation possible in harsh environments. The camera is powered either by 12 to 24V DC or by a 230V AC adapter. Data is recorded by an industrial mini-PC ICS POC-320. The camera can be remotely operated by a notebook connected by Ethernet (preferred) or WiFi. Characteristics of the camera are given in **Table 2**

**Table 2:** Main characteristics of the VarioCAM HDx head 600 infrared camera.

Spectral range	(7.5 ... 14) μm	
Detector	Uncooled microbolometer focal-plane array	
Detector format (IR pixels)	(640 × 480)	
Temperature measuring range	(-40 ... 600) °C	
Measurement accuracy	± 2 °C or ± 2%	
Temperature resolution (@ 30 °C)	Up to 0.03 K	
Frame rate	Full-frame: 30 Hz (640 × 480), sub-frame: 60 Hz (384 × 288)	
Lens		<i>Alternative:</i>
Focal length	10 mm	<i>20 mm</i>
Field of view	57.1° × 44.4°	<i>30.4° × 23.1°</i>
Focus	Motor-driven, automatic or manual, accurately adjustable	
Dynamic range	16 bit	
Power supply	AC adapter, or (12 ... 24) V DC, or PoE	
Storage and operation temperature	(-40 ... 70) °C, (-25 ... 55) °C	
Protection degree	IP67, IEC 60529	
Impact strength, vibration resistance in operation	25 G (IEC 68 - 2 - 29), 2 G (IEC 68 - 2 - 6)	
Dimensions, weight	(221 × 90 × 94) mm, 1.15 kg	
Further functions	Camera internal emissivity correction, shutter free operation	

## 3 Analysis of HUTRAD Measurements

### 3.1 HUTRAD calibration uncertainty

#### 3.1.1 Calibration procedure

During CIMREx, the absolute calibration of the HUTRAD system was performed using a two-point calibration. Absorptive material at ambient temperature was used to cover the entire aperture of antennas to create a ‘hot’ calibration target. The ‘cold target’ was achieved using similar material cooled to  $\sim 77$  K using liquid nitrogen. In practice, metal containers with microwave absorbing material on the bottom surface were applied – these were lifted manually in front of the radiometer antenna aperture (**Figure 4**) and kept in place for a sufficient time to achieve a reliable calibration measurement; during CIMREx, a one minute calibration time was applied. The physical temperature of the ‘hot’ target was measured using a precision thermometer, and assuming the absorber acts as a perfect blackbody, this gives directly the brightness temperature. Similarly, the ‘cold’ target is assumed to be at the boiling point temperature of liquid nitrogen (77 K under nominal pressure conditions).



**Figure 4:** Calibration of HUTRAD receiver using a calibration target (metal container containing absorptive material) in front of the antenna aperture. Two targets are used; one is kept at ambient temperature, the other is cooled with liquid nitrogen prior to calibration. S. Salo (Harp Technologies Ltd.) performing the calibration.

The HUTRAD system does not include a possibility for internal receiver calibration; therefore, emphasis has been placed on the thermal stabilization of the receivers in order to minimize receiver gain and noise temperature variations in between calibrations. In order to verify the stability of the instrument, calibrations have been performed optimally before and after a science flight. In previous studies (e.g. Lemmetyinen et al., 2009; Lemmetyinen et al., 2015) the absolute accuracy, estimated from pre- and post flight calibrations, was estimated to be better than 2 K for the low frequency systems. During CIMREx, a full calibration with the ‘cold’ target was not possible on every occasion, due to logistical difficulties in arranging liquid nitrogen in remote locations. On those occasions, a verification of instrument stability was made using the ‘hot’ calibration load. **Table 3** summarizes the calibrations (with and without LN2) made during CIMREx. The flight to which each calibration is applicable is indicated; while it is technically possible to apply any calibration parameters to any flight data as long as receiver temperatures have been identical, it is preferred to use unique parameters for each mission due to small changes in the final stabilization temperature after each

warm-up of the receivers. The exception is Transfer flight 4, when LN2 calibration was not possible; calibration parameters from Mar 8 are applied.

After verification of calibrations made on Mar 5 and Mar 6, a notable amount of RFI was found on the 6.8 GHz observations. This possibly has possibly affected calibration accuracy at 6.8 GHz on those dates, as well as the calibration in the morning of Mar 7 before Science flight 1. After landing from Science flight 1, the aircraft orientation on the platform of Longyearbyen airport was altered by 180 degrees (radiometers facing North instead of South). The level of RFI was seen to decrease notably (to below detection level). The possible source of RFI were KSAT and EISCAT installations to the South of Longyearbyen airport; significant RFI peaks at 6.8 GHz appear also in the flight data in the vicinity of the airport when facing South.

Another feature detected in post processing of calibration parameters was that parameters for 18.7 GHz, H-pol, were out of the expected range for the morning calibrations made on Mar 7 and Mar 8. It is possible this is due to insufficient heating and stabilization times, which has affected some components of the 18.7 GHz receiver. As a consequence, the morning calibration parameters were not applied for the 18.7 GHz receiver calibration. The present L1 data have been calibrated with the Mar 7 noon parameters (Science flight 1), the average of noon and evening parameters (Science flight 2) and the evening parameters of Mar 8 (Science flight 3). As a precaution, the morning parameters were not applied for any receiver, although calibration parameters were within expected bounds for all other channels than 18.7 GHz H-pol.

**Table 3:** Summary of HUTRAD calibrations and instrument verifications

Date / time of calibration	Location	Applicable flight	LN2 (yes/no)	Comments
Mar 4	Akureyri	Transfer 1 (Transfer 2)	yes	Calibration parameters used also for transfer 2 due to lack of later LN2 calibration
Mar 4	Constable Point	Transfer 1, Transfer 2	no	
Mar 4	Danmarkshavn	Transfer 2	no	
Mar 5	Danmarkshavn	Transfer 3	no	
Mar 5	Longyearbyen	Transfer 3	yes	RFI detected at 6 GHz
Mar 6	Longyearbyen	NA	yes	Multiple calibrations at different receiver temperatures
Mar 7 (morning)	Longyearbyen	Science 1	yes	Calibration parameters at 18.7 GHz H-pol out of expected range; possible insufficient stabilization time
Mar 7 (noon)	Longyearbyen	Science 1, Science 2	yes	
Mar 7 (evening)	Longyearbyen	Science 2	yes	
Mar 8 (morning)	Longyearbyen	Science 3	yes	Calibration parameters at 18.7 GHz H-pol out of expected range; possible insufficient stabilization time
Mar 8 (evening)	Longyearbyen	Science 3	yes	
Mar 10	Danmarkshavn	Transfer 4	no	No possibility for LN2 calibration upon departure
Mar 10	Akureyri	Transfer 4	no	No possibility for LN2 calibration upon departure

### 3.1.2 Effect of physical temperature

Internal physical temperature of the receivers affects drastically the calibration of HUTRAD Dicke-switch receivers. To monitor internal temperature, the receivers have four thermistor sensors each; one on the Dicke switch of the receiver for both polarizations, one on the supporting metal plate, and one measuring air temperature inside the receiver enclosure. Temperature control is based on the air temperature sensor reading. In order to anticipate for possible loss of temperature control and to investigate HUTRAD overall performance (testing during refurbishment had been limited due to time constraints), calibrations during CIMREx were performed at various receiver internal temperatures ranging from 0 to 12 °C. In addition, several extra calibrations at different temperatures were made during the March 6 weather day at Svalbard. A variation in internal temperature was also necessary to compensate for different ambient temperatures expected in Iceland, Greenland and Svalbard. However, all three science flights were conducted with similar internal temperature settings. The following figures depict the two point calibration parameters (receiver Gain and Offset) as a function of receiver internal temperature. For the 6.8 and 10.65 GHz receivers, an almost linear dependence can be found. In the case of the 18.7 GHz receiver, calibrations occasionally deviate from the “expected” linear behaviour. This may be due to receiver designs, as well as uncertainty in stabilization of the receiver internal temperature. The calibration events showing the most deviation from expected values occurred on the mornings of science flight on Mar 7 and Mar 8. As a consequence, these parameters were not used in calibration of science flight data.

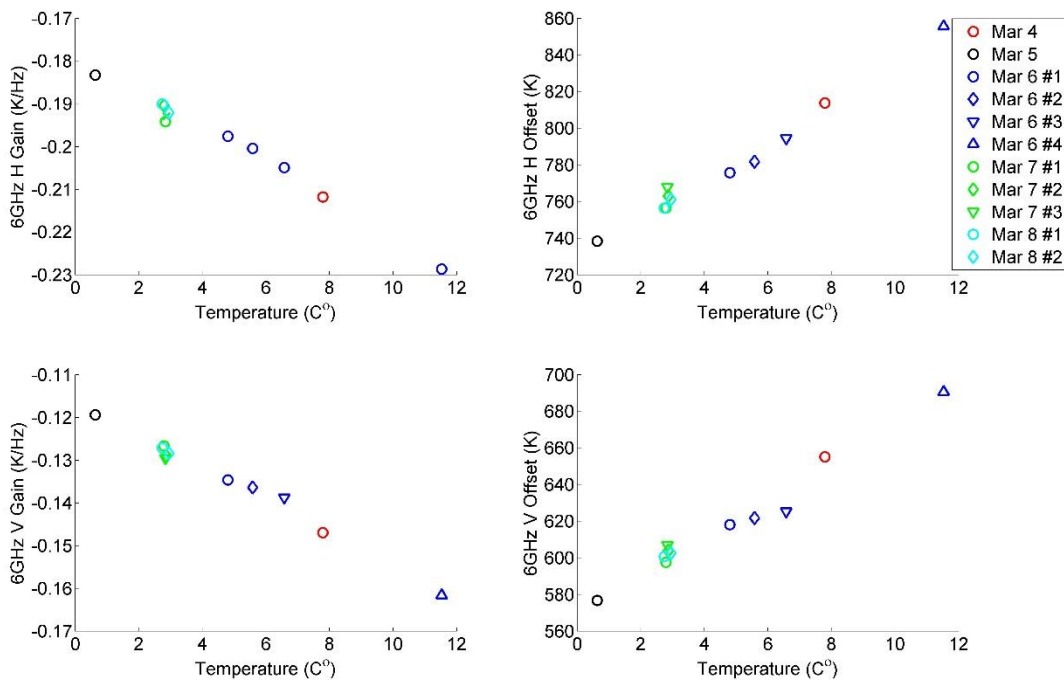


**Figure 5:** Calibration parameters (Gain and Offset) for HUTRAD 6.8 GHz receiver in different receiver internal temperatures.

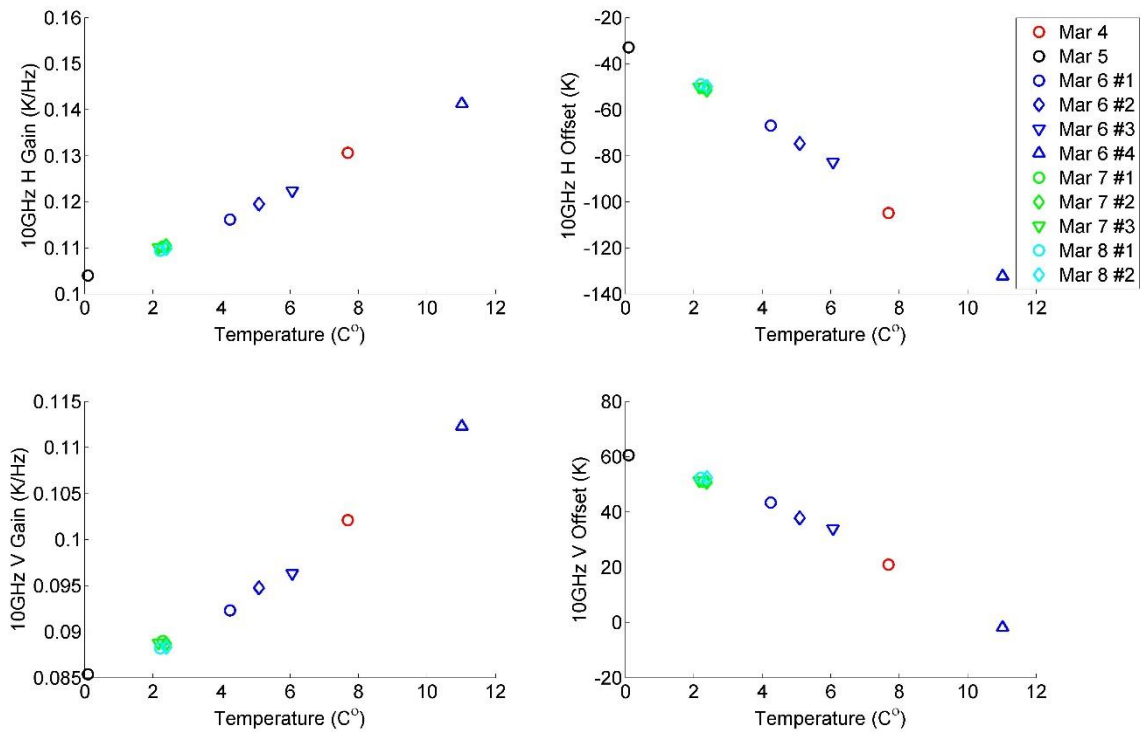


**Figure 6:** Calibration parameters (Gain and Offset) for HUTRAD 10.65 GHz receiver in different receiver internal temperatures.

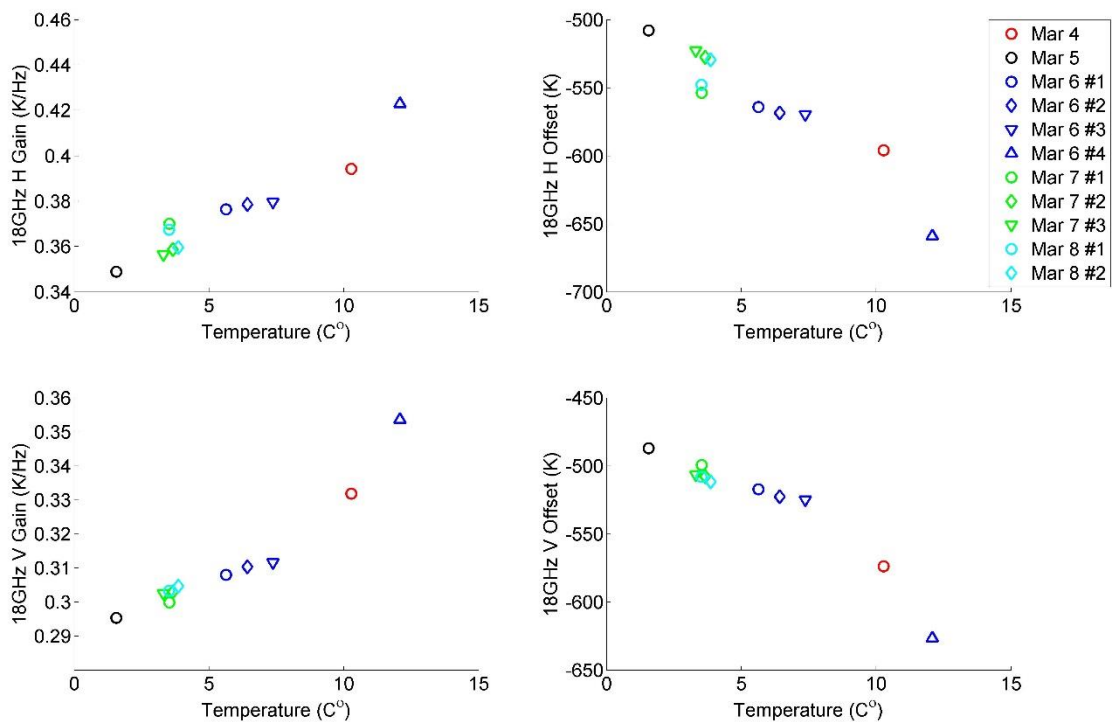


**Figure 7:** Calibration parameters (Gain and Offset) for HUTRAD 18.7 GHz receiver in different receiver internal temperatures.

The quasi-linear behaviour of the calibration parameters allows to estimate the expected error induced in measurements in case of loss of temperature control. This is demonstrated in **Figure 8**, where an expected

error in the calibrated antenna temperature  $\Delta T_B$  is calculated for the horizontally polarized receivers of the 6.8, 10.65 and 18.7 GHz radiometers as a function of deviation from calibration temperature ( $\Delta T$ ). As the effect depends also on the target temperature, three exemplary target brightness temperatures are used (150, 200 and 250 K). These calculations indicate that a deviation of  $\pm 1^\circ\text{C}$  from the calibration temperature would induce an error of up to 3K in the measured brightness temperature, when the target is radiometrically cold (150 K). However, in the case of the 6.8 and 10.65 GHz receivers, this error would be smaller for brighter targets. In the case of the 18.7 GHz receivers, expected errors are limited to less than 1 K with  $\pm 1^\circ\text{C}$  deviation from calibration temperature.

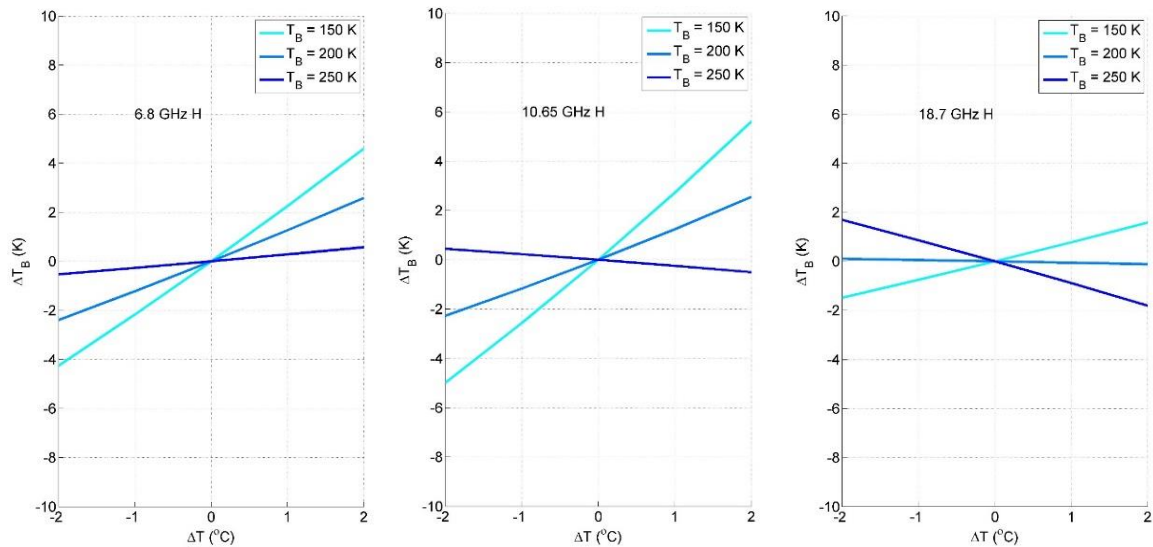


**Figure 8:** Expected sensitivity of calibrated antenna temperature error to receiver internal temperature variations.

The goal of HUTRAD temperature stabilization was to keep internal temperatures within  $\pm 1^\circ\text{C}$  of the specified temperature. During most transfer flights and during all science flights this goal was achieved. On some transfer flights (e.g. transfer flight #3, **Figure 9**) temperature variations exceeded this limit for some sensors, typically for one of the Dicke switch thermistors. However, temperature remained within  $\pm 1^\circ\text{C}$  for the reference sensor (housing air temperature).

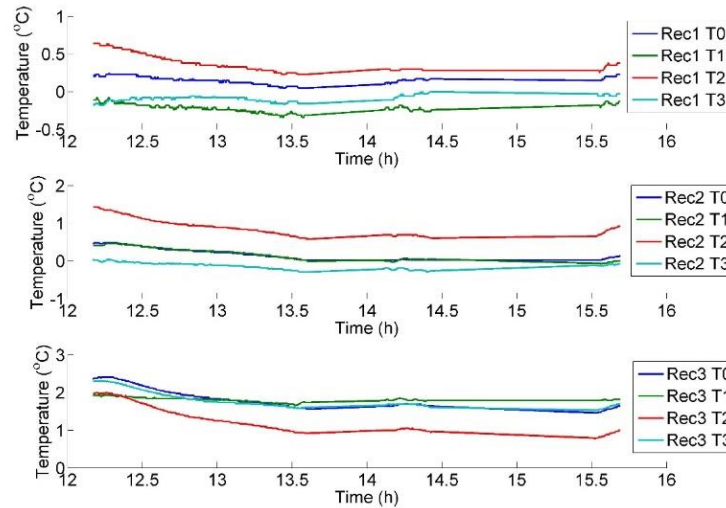


**Figure 9:** Internal physical temperatures of HUTRAD receivers during Transfer flight #3. Temperature stability specification ( $\pm 1^\circ\text{C}$ ) exceeded for Receiver 3 sensor T2 (10.65 GHz, H-pol Dicke switch sensor).

As the receiver internal temperature stability criterion was mostly met during the campaign, no attempt was made to recalibrate flight data based on the measured small variations in temperature. In the future, recalibration attempts could be done based on e.g. variations in the Dicke switch temperature. However, the induced difference in flight data TB is expected to be small ( $< 3\text{K}$ ).

### 3.1.3 Estimation of absolute accuracy

An estimate of absolute calibration accuracy was made based on a comparison of calibration measurements before and after each measurement flight. In essence, the deviation ( $\Delta$ ) from the expected brightness temperature of calibration targets, when applying calibration parameters for a given flight, was analysed. For example, during Science flights the calibration parameters were calculated from an average of pre- and post-flight parameters;  $\Delta T_B$  values thus indicate a “worst case” calibration drift for targets at ambient temperature ( $T_{B,HOT}$ , about 250-260K) and at the temperature of liquid nitrogen ( $T_{B,COLD}$ , 77K). **Table 4** lists the  $\Delta T_{B,HOT}$  and  $\Delta T_{B,COLD}$  values for each science flight and  $\Delta T_{B,HOT}$  for each transfer flight. Note that for transfer flights,  $\Delta T_{B,COLD}$  could not be obtained due to lack of liquid nitrogen for cooling. The Average MAE for all flights was  $< 2\text{K}$  on all channels. Errors during science flights were somewhat larger for  $T_{B,COLD}$ ; thus, somewhat larger errors may be expected for cold targets (e.g. open water) during transfer flights.

**Table 4:** Deviation ( $\Delta T_B$ ) from reference targets during CIMREx.

Flight	Event	Reference target	6.8 GHz K		10.65 GHz		18.7 GHz	
			H (K)	V (K)	H (K)	V (K)	H (K)	V (K)
Transfer 1	After flight verification	$\Delta T_{B,HOT}$	-2	-1.8	0.6	0.1	1.1	2.2
		$\Delta T_{B,COLD}$	-	-	-	-	-	-
Transfer 2	After flight verification	$\Delta T_{B,HOT}$	0.4	0.2	1.3	0.9	2.1	3.4
		$\Delta T_{B,COLD}$	-	-	-	-	-	-
Transfer 3	Preflight verification	$\Delta T_{B,HOT}$	0.1	-2.2	2.8	3.3	0.6	0.3
		$\Delta T_{B,COLD}$	-	-	-	-	-	-
Science 1	Preflight calibration	$\Delta T_{B,HOT}$	-1.9	-1	-0.2	-0.4	1.5	-0.3
		$\Delta T_{B,COLD}$	-1.3	-1.4	-0.3	-0.1	6.8	-1.2
	After flight calibration	$\Delta T_{B,HOT}$	0.2	-0.2	0.2	0.4	0	0.3
		$\Delta T_{B,COLD}$	1.4	1.3	0.3	0.1	0	1.3
Science 2	Preflight calibration	$\Delta T_{B,HOT}$	0.8	0.7	0.1	0.4	0	0.2
		$\Delta T_{B,COLD}$	0.3	0.2	0.4	0.3	0.6	0.3
	After flight calibration	$\Delta T_{B,HOT}$	-0.6	-1	0	-0.2	-0.1	0
		$\Delta T_{B,COLD}$	1.9	1.6	-0.4	-0.4	-1.2	0.7
Science 3	Preflight calibration	$\Delta T_{B,HOT}$	-0.4	-0.7	0.1	0.1	1.1	-0.1
		$\Delta T_{B,COLD}$	-1.3	-1.6	-0.2	0	5	-0.5
	After flight calibration A	$\Delta T_{B,HOT}$	0.2	0.8	-0.2	-0.5	0.1	0.3
		$\Delta T_{B,COLD}$	2.2	2.5	0.5	0.6	-0.1	0.8
	After flight calibration B	$\Delta T_{B,HOT}$	0.3	0.7	0.3	-0.4	-0.1	-0.1
		$\Delta T_{B,COLD}$	1.4	1.5	0.6	-0.4	0	0.2
	After flight calibration C	$\Delta T_{B,HOT}$	-0.3	-0.2	-1	0.1	0.2	0.1
		$\Delta T_{B,COLD}$	0.4	0.8	-0.3	-0.2	0.1	0.3
Transfer 4	Preflight verification	$\Delta T_{B,HOT}$	2.1	1.6	1.5	3.2	2.9	3.2
		$\Delta T_{B,COLD}$	-	-	-	-	-	-
	After flight verification	$\Delta T_{B,HOT}$	-0.1	-0.5	-0.4	1.4	-0.3	0.4
		$\Delta T_{B,COLD}$	-	-	-	-	-	-
Summary	Science flights	$\Delta T_{B,HOT}$	<b>0.6</b>	<b>0.7</b>	<b>0.3</b>	<b>0.3</b>	<b>0.4</b>	<b>0.2</b>
	MAE (K)	$\Delta T_{B,COLD}$	<b>1.3</b>	<b>1.4</b>	<b>0.4</b>	<b>0.3</b>	<b>1.7</b>	<b>0.7</b>
	Transfer flights	$\Delta T_{B,HOT}$	<b>0.9</b>	<b>1.3</b>	<b>1.3</b>	<b>1.8</b>	<b>1.4</b>	<b>1.9</b>
	MAE (K)							

### 3.2 AMSR2 vs HUTRAD Tbs - for all science flights

Here we analyze the measurements of all science flights together. All science flights were carried out at a nominal flight altitude of 305 m and thus have comparable footprint sizes. The ice cover during the science flights was diverse with different ice classes and ice thickness varying on small (<km) scale. Thus, the limited number of HUTRAD measurements within the AMSR footprint likely will not be fully representative for the complete AMSR2 footprints. The three mow-the-lawn patterns flown at the end of the transect largely

mitigate this problem. However, due to ice drift during the flight and the time difference to the satellite acquisition also here differences can be expected for such a diverse ice cover.

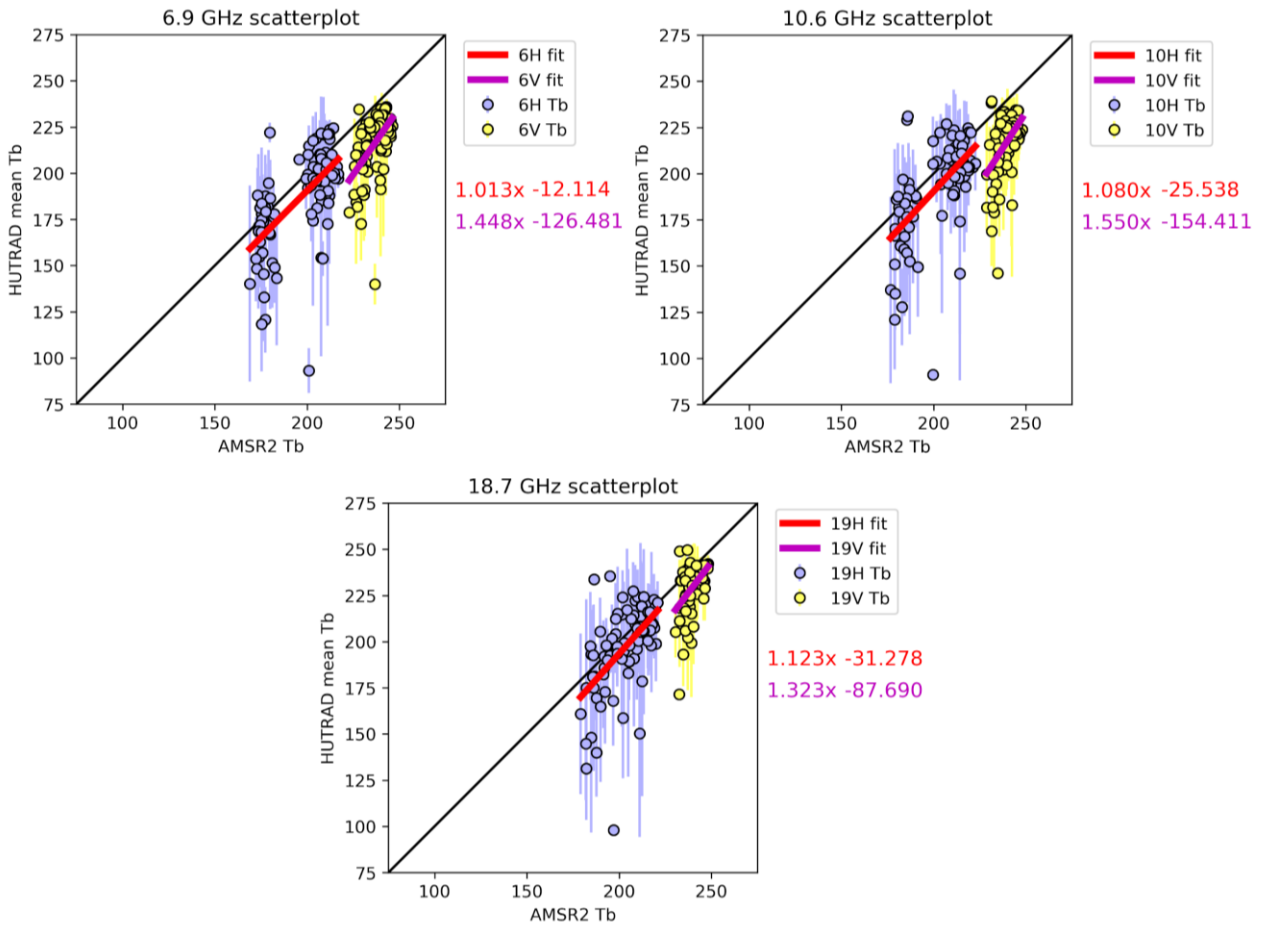


**Figure 10:** Scatter plots of HUTRAD measured (y-axis) and collocated AMSR2 (x-axis) brightness temperatures for all three CIMREx science flights at 6.9, 10.65 and 18.7 GHz respectively.

**Table 5:** Statistics for the comparison of HUTRAD and collocated AMSR2 brightness temperatures for all three CIMREx science flights. All values are shown in Kelvin.

		6.9 V	6.9 H	10.65 V	10.65 H	18.7 V	18.7 H
Mean	AMSR2	237.5	197.1	239.6	201.6	239.9	203.5
	HUTRAD	217.4	187.6	217.0	192.2	229.7	197.4
Bias (HUTRAD - AMSR2)		-20.1	-9.5	-22.6	-9.5	-10.3	-6.1
Standard deviation of the difference		13.6	19.8	14.3	21.0	11.0	19.7

### 3.2.1 Explanation of graphic

The data point colors represent the polarisation with yellow for the V polarised and purple for the H polarised Tbs. We refer to the C-band channel here and in the following as 6.9 GHz, which is the center frequency of AMSR2 while for HUTRAD it actually it actually is 6.8 GHz. The other two center frequencies agree between AMSR2 and HUTRAD.

Most AMSR2 footprints are covered by several HUTRAD measurements. On average for the mow-the-lawn patterns during the science flights, 261 airborne measurements match one satellite footprint. In such cases the mean of the HUTRAD observations is shown with their standard deviation represented as the error bars in the plot.

There are two fit lines, magenta for the V polarization and red for the H polarization points. The corresponding linear fit coefficients are listed to the right of the plot in the same colors as the fit lines. The identity line is represented in black.

The data has been filtered according to the aircraft roll values, the distance between airborne and satellite footprints (see Section 2.1.2), as well as erroneous HUTRAD measurements (Tbs < 10 K were discarded). Additionally, only the mow-the-lawn pattern observations from all three science flights are shown in this comparison.

### 3.2.2 Commentary and Interpretation

For both H and V polarizations the HUTRAD data points show a large spread of values. This is characteristic for the diverse ice cover in the study region. The range of Tb values for AMSR2 and HUTRAD largely overlap and have similar mean values with relatively large biases between 6 and 22 K. These values are shown in **Table 5**. The HUTRAD Tbs are underestimated when compared to AMSR2 ones, for both polarizations and at all frequencies with similarly large bias values (around 20 K for V and 9.5 K for H pol) at 6.9 and 10.65 GHz and a slight decrease (10 K for V and 6 K for H pol) at 18.7 GHz. Besides calibration differences between the instruments also the atmosphere, at least at 18.7 GHz, and the differences in surface area covered, i.e. spatial variability, can play a role for these differences. The slope of the fit at H polarization is close to one and very similar for all frequencies (range 1.0 to 1.1), i.e. AMSR2 and HUTRAD show the same sensitivity, which is good. The remaining difference could be indicative of a systematic bias over sea ice (but see Section 3.3 for water). At V polarization the slope of the fit is more variable (range 1.3 to 1.6). Which could be indicative for sub-footprint scale variability of the Tbs playing a role for the differences. The Tb scatter is large especially for H polarized data points, which again confirms the diverse ice situation. This is a typical situation in the marginal ice zone (MIZ) during winter ice growth conditions. The area of the MIZ with such diverse ice situation currently is and will continue to increase in the future. This highlights the demand to observe the sea ice cover at as high as possible spatial resolution. The current resolution of the AMSR2 instrument at the three evaluated frequencies certainly is not high enough to fully resolve the variability of the ice situation in the MIZ in winter as is demonstrated by the HUTRAD measurements.

There are two discernible clouds of data points at H polarization with a clear separation between them, which decreases with frequency. This behaviour is indicative of Tbs measured over sea ice, corresponding to the

cloud of higher Tb values, and open water or very thin ice which have much lower values. During the three science flights only small areas of open water were measured, which results in the limited number of low Tb values as shown in **Figure 10**. Mind also that the Tb values at H polarization for the open water cloud is much lower than the lowest Tb values at V polarization. This is indicative for the strong polarization of water at microwave frequencies and incidence angles around 50° with much lower emissivity at H than at V polarization.

### 3.3 AMSR2 vs HUTRAD Tbs - for all transfer flights

The transfer flights to Svalbard and back were carried out at a higher altitude of 1600 m. During the transfer flight back from Longyearbyen to Constable Pynt no measurements could be carried out (see Section 2). Also, no IR data are available for these flight (IR camera was out of focus). However, the sea ice in the East Greenland current contains more old, multiyear ice compared to the science flights around Svalbard. Also, ice that has passed Fram Strait is often deformed. In addition, these flights contain longer open water areas with no sea ice, which is useful for understanding systematic differences between HUTRAD and AMSR2. For open water the surface brightness temperatures Tb can be assumed to be homogeneous enough within an AMSR2 footprint that a HUTRAD transect through an AMSR2 footprint should be representative and comparable to the AMSR2 measurements. Atmospheric forced variability, however, like varying sea surface roughening by winds or cloud liquid water variability by clouds, which both affect the Tb, can still be present.

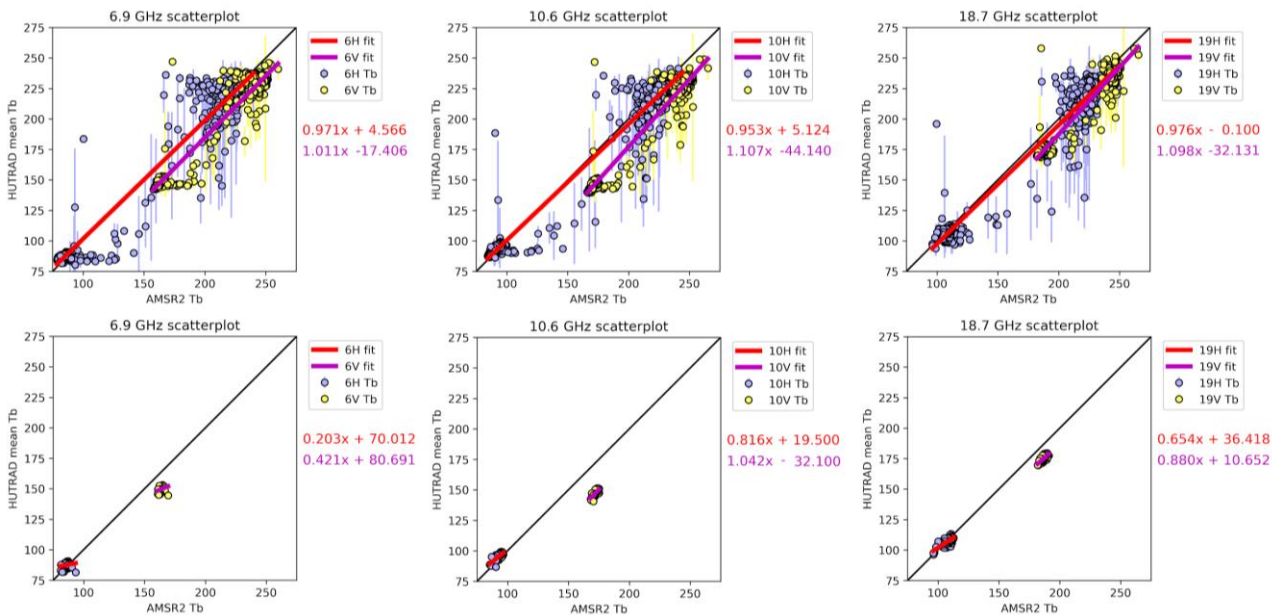


**Figure 11:** Scatter plots of HUTRAD measured (y-axis) and collocated AMSR2 (x-axis) brightness temperatures for the CIMREx transfer flights at 6.9, 10.65 and 18.7 GHz respectively. Top row panels show all data points from these transfer flights, while the bottom three panels show the open water data only.

**Table 6:** Statistics for the comparison of HUTRAD and collocated AMSR2 brightness temperatures for the transfer flights. All data points shown in the top row panels of **Figure 11** are included in this statistical analysis. All values are shown in Kelvin.

		6.9 V	6.9 H	10.65 V	10.65H	18.7 V	18.7H
Mean	AMSR2	212.2	164.3	216.7	169.3	222.1.5	176.5.0
	HUTRAD	197.1	164.0	195.7	166.6	211..7	172.2.1
Bias (HUTRAD - ASMR2)		-15.1	-0.3	-21.0	-2.8	-10.4	-4.3
Standard deviation of the difference		8.8	14.5	9.2	13.0	7.5	12.3

**Table 7:** Statistics for the comparison of HUTRAD and collocated AMSR2 brightness temperatures for the transfer flights. Only the open water filtered data points (bottom row panels of **Figure 11**) were included in this statistical analysis. All values are shown in Kelvin.

		6.9 V	6.9 H	10.65 V	10.65H	18.7 V	18.7H
Mean	AMSR2	164.1	86.1	172.4	92.9	187.5	108.0
	HUTRAD	149.8	87.5	147.6	95.3	175.7	107.1
Bias (HUTRAD - ASMR2)		-14.3	1.4	-24.8	2.4	-11.8	-1.0
Standard deviation of the difference		2.1	2.7	1.6	2.0	1.7	2.8

### 3.3.1 Explanation of graphic

These are the same type of plots as those shown in **Figure 10**, but applied to the data from the transfer flights. The top row plots show all valid data points from the transfer flights only excluding extreme roll values (larger than  $\sim 10^\circ$ ) and land pixels. For the bottom row plots, only the open water pixels have been kept (last part of transfer between Danmarkshavn and Longyearbyen and transects between Akureyri and Constable Pynt). When looking at all data from the transfer flights an average of 113 HUTRAD measurements are averaged inside one AMSR2 footprint, while for the open water only data points there are on average 95 airborne observations for one satellite measurement.

### 3.3.2 Commentary and Interpretation

When comparing the top row of **Figure 11** to the plots in **Figure 10**, the scatter of the Tbs is reduced and the fit lines are much closer to the identity line, with near perfect slopes for both polarizations between 1.0 and 1.1. At H also the intersects are at or below 5 K and the bias is between 0.3 and 4.3 K. At V polarization again, a significant negative bias between 15 and 21 K for the HUTRAD C and X-band can be observed, respectively. For K-band the bias is at 10 K. While on average the airborne measurements fit well with the satellite observations as shown by the fit lines, the scatter is large especially for H polarized data points (standard deviation of about 13 K). There are again two discernible clouds of data points with a clear separation between them. This behaviour is indicative of Tbs measured over sea ice, corresponding to the cloud of higher Tb values and open water which have much lower values (see also last section).

When looking at the open water pixels only (bottom three panels of **Figure 11**), there is much smaller scatter both for HUTRAD as well as for AMSR2. Therefore, there is little information in the fit lines as the Tb values from both HUTRAD and AMSR2 measurements show very little variation within the same frequency. This is consistent with passive microwave measurements over calm ocean conditions. While the mean values and standard deviation of the difference between the airborne and satellite observations have decreased to about 2 K due to the homogenous open water surface, the bias values are very similar to those for the whole dataset including sea ice scenes (see **Table 6** and **Table 7**). This indicates that the bias sources (atmospheric influences and footprint size disparities) are the same in both cases. For H polarization the absolute bias is between 1 and 2.4 K, which is in the range of what can be expected from the HUTRAD radiometric resolution and not considering the atmosphere and changes in surface roughening between the two acquisitions. However, at V polarizations the bias over open water remains between -12 and -25 K, which could be indicative of a systematic bias. However, as the fit lines are close to one the same sensitivity of Tb is found for HUTRAD and AMSR2.

Due to the larger flight altitude the transfer flights provide larger HUTRAD footprints. The agreement between HUTRAD and AMSR2 gets much improved for these flights even without the dedicated mow-the-lawn pattern. The larger number of open water points together with a, while deformed, but regarding ice types more homogenous sea ice cover in the East Greenland Current (EGC) provides a much better correspondence between satellite and airborne measurements. Compared to the MIZ ice cover presented in **Figure 10** the standard deviation (error bars in **Figure 10**, **Figure 11**) of HUTRAD measurements within the AMSR2 footprint got reduced (mean STD science flights 19.1 K for H and 10.4 K at V polarization, while for the transfer flights it decreased to 3.5 K at H and 2 K at V polarization for all frequencies and surface types). This again confirms that the Tb surface variability during the transfer flights was smaller than during the science flights (however, mind the different flight altitudes). The ice situation in the EGC with significant amount of multiyear ice can be considered more typical for the past Arctic sea ice conditions, which were dominated by old, multiyear ice. The new Arctic consists of predominantly first-year ice and the diverse winter ice conditions found during the science in the MIZ (Section 3.2) can be considered more typical for a larger part of the Arctic in the future. The MIZ is also the region where most of the commercial traffic and offshore activities can be expected. These are the target regions for CIMR.

In conclusion, the HUTRAD measurements demonstrate the high spatial variability of sea ice Tbs in the MIZ around Svalbard during winter conditions. Different stages of ice growth together with matured first-year ice provide conditions with high sub-footprint Tb variability for the three AMSR2 C-, X-, and K-band frequencies.

Atmospheric influence cannot be neglected at K-band. But as the variability and differences between AMSR2 and HUTRAD are similar at the two lower frequencies, surface Tb variability caused by the diverse ice situation in the MIZ can be considered the main cause for the high HUTRAD standard deviations within the AMSR2 footprints and also for the differences in mean and linear regression between HUTRAD and AMSR2.

However, the transect flights with a significant larger fraction of open water, which can be considered radiometrically more homogenous, shows that there is a potential bias between 14 - 25 K for the vertical Tb values at C and X-band between AMSR2 and HUTRAD. At horizontal polarisation the bias is much reduced and less than 2.5 K. Considering the radiometric uncertainties and differences in footprint coverages such a difference can be expected.

**Another possibility for the bias may be reflections or distortions in the antenna beam pattern caused by the aircraft hatch.** The fact that the bias is strongest at V-pol indicates possible reflection of the cold sky from the hatch floor. This possibility was not tested during the campaign due to limited time. For future campaigns, it would be necessary to explore this possibility with dedicated measurements.

### 3.4 Comparison of HUTRAD observations from forward and backward transects

During the mow-the-lawn patterns of all three science flights some transects were flown in forward and backward direction with only a small time difference of on average 7.7 minutes.

**Figure 12** shows an example from science flight 3. For each of the three patterns five out of the seven transects were overflown in both directions, i.e. a total of 15 transects. The footprints of the forward and backward transects lay close together but seldom overlap. Figure 4-3 shows the worst case for the highest frequency channel (18.7 GHz), which has the smallest footprint. For the lower frequencies the overlap is better. Anyway, the forward and backward transects allow to observe similar ice conditions from two different viewing angles, i.e. shifted by 180°.

In the following all comparisons are done with a maximum distance of 450 m between the observations of the forward and backward transect. The mean distance is 372 m and minimum distance 60 m. Which means that most footprints from the forward and backward transect do not overlap. Also, all observations with a roll of the aircraft above 5° were removed. In addition, please mind that within the average 7.7 minutes time difference the ice can have drifted 50–10 m. The mean ice drift direction was perpendicular to the transect direction. This can have moved the sea ice in the footprints closer together. Anyway, in the following we have to assume that the forward and backward transects measure similar but not the same ice conditions.

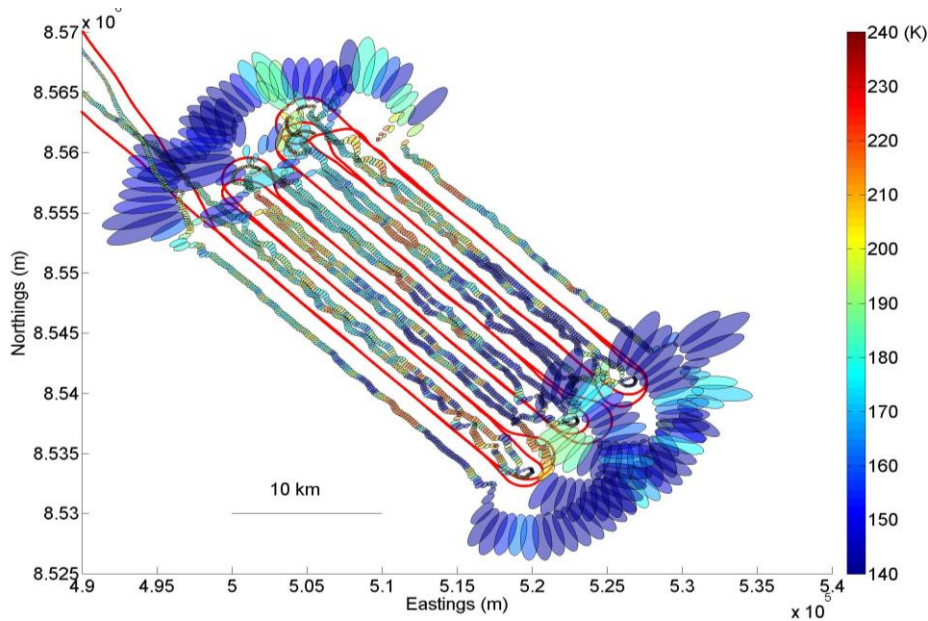


**Figure 12:** Mow-the-lawn flight pattern during science flight 3 on 8th March 2019 south-east of Storfjorden. Red shows the flight track of the airplane and the colored ellipses are the HUTRAD 9 dB footprints at 18.7 GHz H. Mind the five forward and backward transects, which lay close together but seldom overlap.

In **Figure 13** the data of all 15 forward-backward transects are shown together as one time series. Because of the high brightness temperature variability from one measurement to the next the time series are smoothed with 100 measurements running mean. First, we can observe that all three frequencies behave very similar regarding the difference between the forward and backward transect. We can see the expected polarization difference between H and V and that both forward and backward Tbs covary. Overall the Tbs of the forward and backward flight tracks agree very well. There are only a few instances like at about measurement 1050 where forward and backward observations do not agree. Besides that, there is high co-variability with a correlation of 0.84.

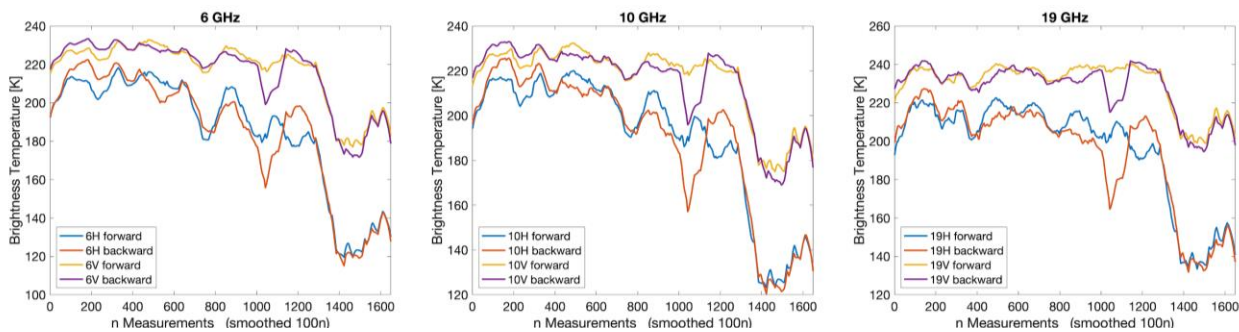


**Figure 13:** Brightness temperatures  $T_b$  from all 15 forward and backward transects from all three science shown as one time series and smoothed with a 100 measurements running mean. Left: C-band, middle: X-band, and right: K-band data.

**Figure 14** shows the  $T_b$  scatter plots of forward versus backward transects for all frequencies and polarisations. **Table 8** summarizes the statistics for the comparison. We can observe that for both polarizations H and V the bias and standard deviations increase with frequency while correlation decreases. This can be attributed to the decreasing footprint size with frequency and a similar effect can be expected

for CIMR. For a smaller footprint the likelihood that the two footprints are not aligned or overlap on the forward and backward flight and thus the sea ice cover is different will increase. This, as expected, increases the standard deviation and decreases the correlation. The bias does not necessarily need to be affected by this but in our case also the bias increases with frequency. In accordance with the statistics the scatterplots show that the variability of the H polarization measurements is higher than for V polarization (19 K vs. 12 K standard deviation). The bias between forward and backward flight transects is with 0.8 K and 1.3 K similar for H and V polarization, respectively.

In conclusion, we find biases in the order of 0.5–2 K and standard deviation above 10 K between the forward and backward flown transects. These differences are higher than the expected radiometric resolution of <0.3 K of the HUTRAD radiometer (**Table 1**), while being within the expected calibration accuracy (**Table 4**). The ice cover in the study region was very diverse (see next section) with different ice types and ice thicknesses. The footprints of the forward and backward transects do not or only partially overlap. Already small changes in the open water/thin ice fraction within the footprint between the forward and backward flight will have large effects on the measured brightness temperature. This is also expressed by the higher standard deviation for H polarization because here the  $T_b$  difference between open water and ice is larger than at V polarization. Based on the ice velocity maps from OSISAF we estimate an average ice drift of 50 to 100 m between a forward and backward acquisition (mean time difference is 7.7 minutes). This will either add or reduce the on average 372 m difference in footprint location on the ground between the forward and backward transects. We attribute most of the differences and variability to the effects of not or not completely overlapping footprints in a diverse ice cover. Anisotropic effects from the 180° viewing angle difference likely only play a minor role. To evaluate anisotropic effects an experiment with non-moving, i.e. fast-ice, and much better pointing accuracy between the different directions would be needed.

**Table 8.** Statistics for the forward to backward transects comparison.

	<b>6.8 GHz H</b>	<b>6.8 GHz V</b>	<b>10.7 GHz H</b>	<b>10.7 GHz V</b>	<b>18.7 GHz H</b>	<b>18.7 GHz V</b>	<b>H</b>	<b>V</b>
<b>Bias</b>	0.2 K	0.7 K	0.5 K	1.3 K	1.7 K	1.9 K	<b>0.8 K</b>	<b>1.3 K</b>
<b>Standard Deviation</b>	16.8 K	10.1 K	18.7 K	12.1 K	22.7 K	12.6 K	<b>19.4 K</b>	<b>11.6 K</b>
<b>Correlation</b>	0.89	0.89	0.87	0.85	0.78	0.76	<b>0.85</b>	<b>0.83</b>

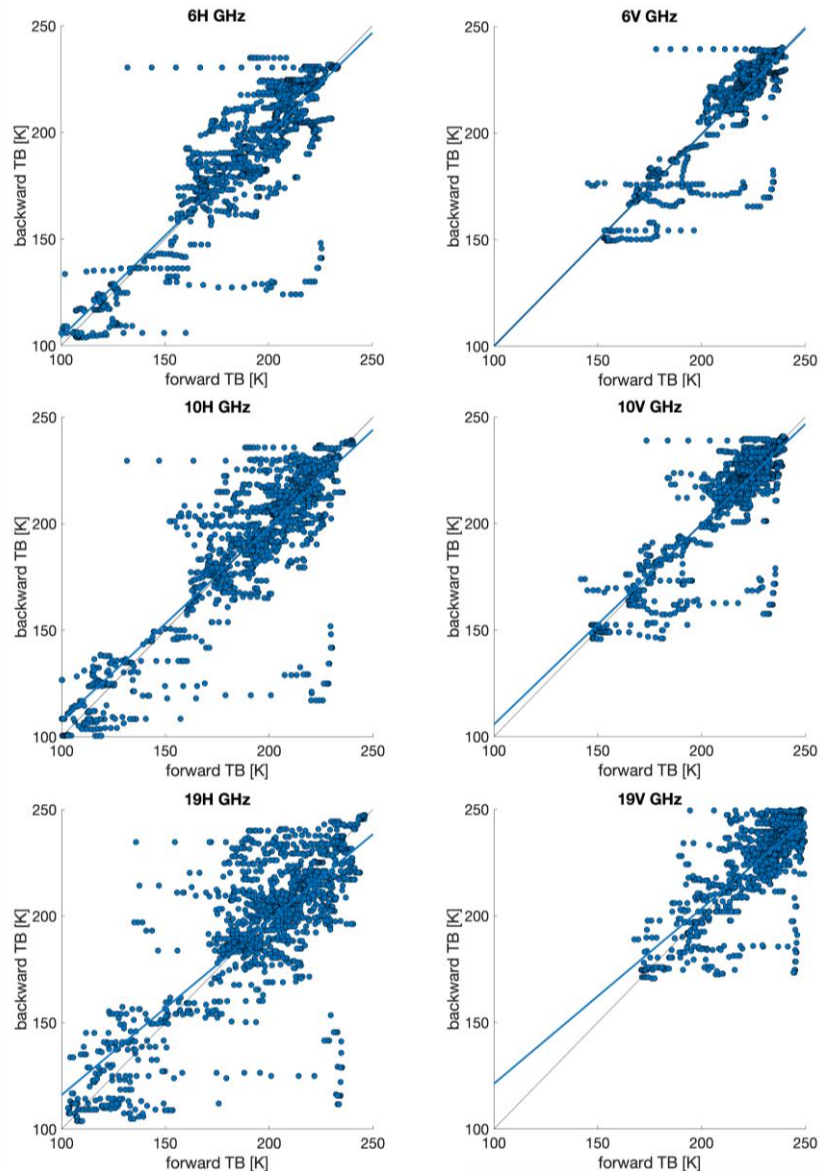


**Figure 14:** Scatter plots of Tbs from forward transects versus backward transects. Upper row shows the C-band data, middle the X-band, and lower the K-band data. Left plots are for horizontal polarization H and right for vertical polarization V.

### 3.5 Using HUTRAD measurements together with thermal camera data

During all three science flights IR camera data is available. While the radiometer covers individual footprints the IR camera acquires an entire image, which is larger than the HUTRAD footprints (**Figure 15**). Thus we can resolve the thermal infrared emission variability within the HUTRAD covered individual footprints.

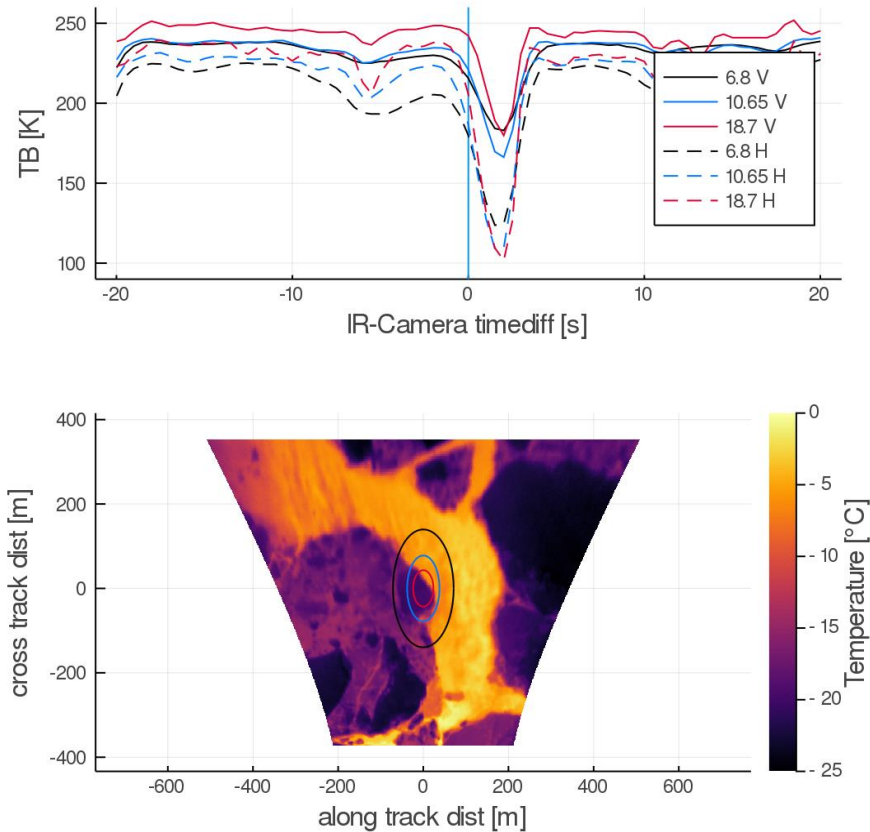


**Figure 15:** HUTRAD Tb measurements time series in combination with a thermal camera image during the first science flight on 7 March 2019.

**Figure 15** shows at the top the HUTRAD time series for all three frequencies and polarizations. At time 0 the thermal image (shown at the bottom) is taken. Inside the observation scene the concentric footprints of the HUTRAD radiometer channels are shown. The thermal image covers approximately +/- 5 seconds of the HUTRAD time series depending on the speed and height of the aircraft.

The different temperature regimes can be visually identified in the thermal camera images and are used for classification.

### 3.5.1 IR based surface type classification and comparison with HUTRAD brightness temperatures.

The classification of ice types is done for a joint comparison across all science flights (the mow-the-lawn-patterns) together with the HUTRAD brightness temperatures. Based on the IR measurements different ice classes were identified and analysed for their microwave radiometric signal. For the classification an infrared emissivity of 0.97 was assumed across all surfaces and under all observation angles. The three classes are shown in **Table 9**. The thresholds for the classes were empirically derived from a set of manually classified IR images.

**Table 9.** Ice classes identified in the thermal images with assumed emissivity of 0.97.

class (interpretation)	temperature condition
open water/thin (bare) ice	$T > 270 \text{ K}$
thin ice/moderate snow cover	$270 \text{ K} > T > 260 \text{ K}$
thicker ice/thicker snow cover	$260 \text{ K} > T$

For each ice class now the HUTRAD brightness temperatures are extracted. For a class to be valid, more than 70% of the HUTRAD footprint has to be covered by one ice type. The resulting brightness temperatures for each ice type and frequency are summarized by mean and standard deviations in **Figure 16**. The three panels showing the HUTRAD  $T_b$  observations at the three channel frequencies for three surface types identified from thermal camera measurements. The  $T_b$  data from all three science flight have been combined into these plots. The colors represent the channel polarisation with orange for vertical and blue for horizontal.

The open water observations have lowest  $T_b$ s and highest polarization differences between  $T_b$  V and  $T_b$  H. The open water class also shows small variabilities in horizontal polarization and even smaller in vertical polarization across all frequencies. Notably, the lowest variability, i.e. most stable, and lowest brightness temperature of open water is found at the lowest frequency of 6.8 GHz. The thin ice/snow class shows the highest variability across the classes again with higher variability in the horizontal channels and increasing with increasing frequency. For the thick ice/snow class, the variability at vertical polarization is small and much higher at horizontal polarization. Especially at H polarization the  $T_b$  for thick ice/snow is significantly higher than for the thin ice/snow class at all frequencies and also has a much lower polarization difference. This would allow separation of these two ice classes at all three frequencies. However, current sea ice concentration (SIC) algorithms do not account for this effect, which in the case of thin ice/snow would lead to an underestimation of SIC, because the radiometric properties of the thin ice/snow class lay between the open water and the thick ice/snow class.

The stability of the 6 GHz vertical polarization at the open water and thicker ice classes indicates a good sensitivity to the ice concentration while the high variability of the signal for thin ice can be seen as a source of potential underestimation of ice concentration using a 6 GHz based algorithm in the freeze-up period.

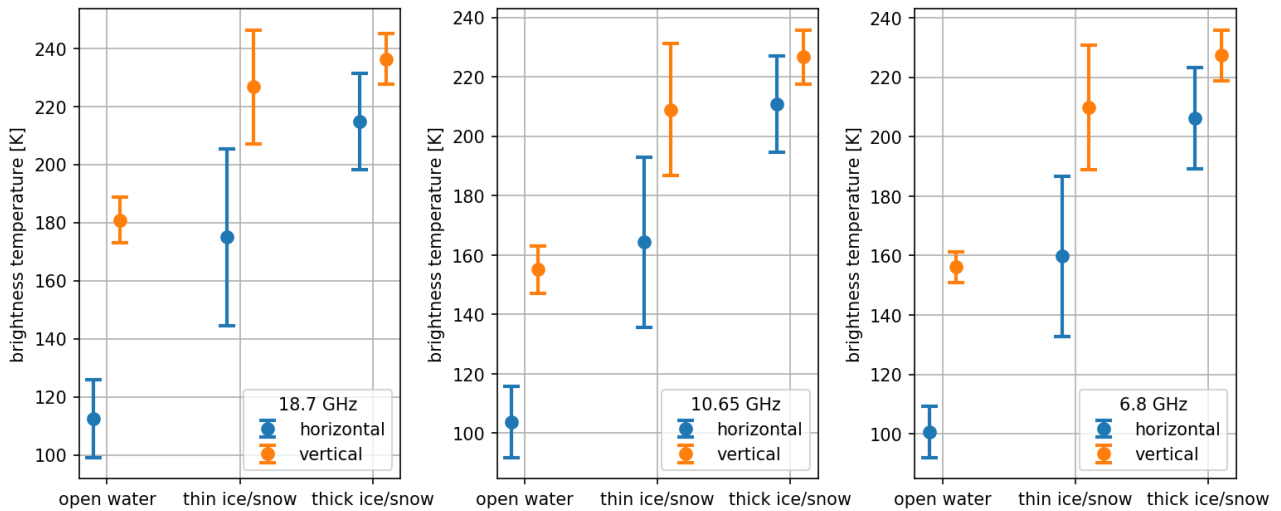


**Figure 16:** HUTRAD Tbs for different ice types identified from thermal camera measurements [at the three different frequencies](#).

### 3.5.2 HUTRAD Tbs compared with IR based ice surface temperature

The relation of HUTRAD brightness temperatures to infrared based ice surface temperatures are analyzed using several filters to reduce random noise. Only points with aircraft roll value below  $2^\circ$  and only points in the mow-the-lawn pattern area of the science flights are used to ensure better homogeneity of the surface conditions. Scenes where at least one of the HUTRAD footprints contains open water have also been excluded from this analysis. In the following, the three different science flights are discussed individually as they show different features.

**Figure 17** shows a scatter plot of the HUTRAD Tbs against the surface temperature determined by the infrared camera. The solid darker lines represent the mean value over 0.5 K bins. A large scatter of the data points at 18.7 GHz can be seen, even for the usually more stable signal at vertical polarization. This scatter decreases with frequency so that the 6.8 GHz channels data points present more solid clusters. The maximum Tb values measured at 6.8 and 10.65 GHz are also significantly lower than those at 18.7 GHz. This could be caused by a relatively thin variable snow cover which would introduce more variation of physical scattering at higher frequencies while maintaining a more stable signal at lower frequencies. Also the different footprint sizes might play a role for the lower scatter at lower frequencies. The very cold surface conditions indicate either an underestimation of the infrared surface emissivity (we use 0.97) for this surface type or a recent snowfall event. At low air temperatures this would isolate the ice cover well from the heat coming from the warm ocean. The sudden change of slope of brightness temperature with infrared temperature in Figure 4-8 at about 254 K surface temperature however supports the idea of a recent snowfall event. The higher temperatures then are related to even higher snow-ice interface temperatures which cause an increase of liquid brine leading to a drop in brightness temperature, especially at lower frequencies. In science flight 1, some sea smoke contaminated open water observation and also potentially the sea ice close to open water. Since the sea smoke appears mostly colder in the infrared images than water or also thin sea ice, some

inferred thin sea ice surface temperature might be lower than the actual sea ice temperature.

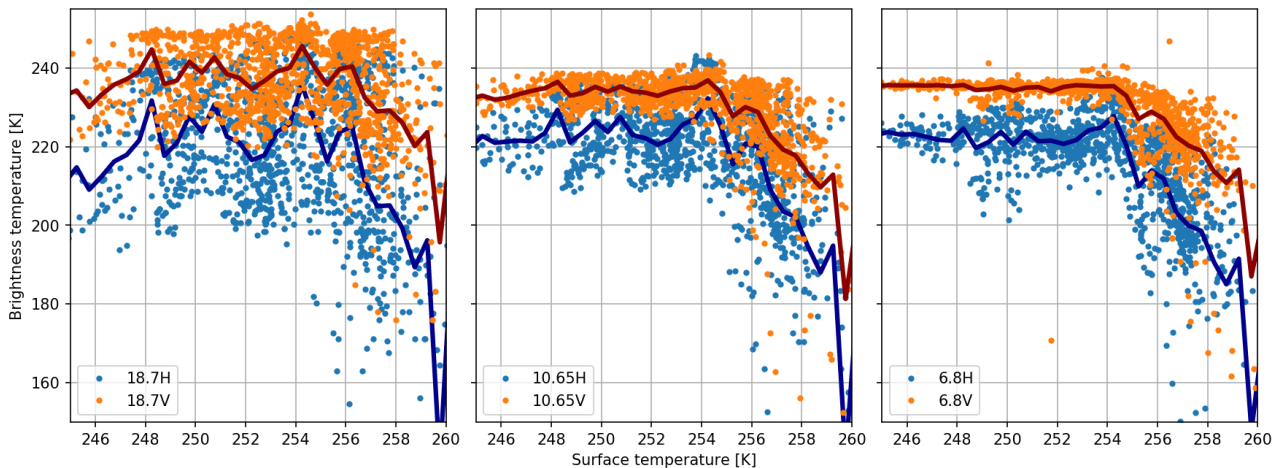


**Figure 17:** HUTRAD Tbs versus thermal camera ice surface temperature for the three different channel frequencies measured during science flight 1 on 7th March 2019 north of Svalbard.

**Figure 18** shows the same relations as **Figure 17** but for the data of science flight 2. The radiometer Tbs across all channels are more anticorrelated with the infrared surface temperatures compared to science flight 1. This could be explained with the influence of a saline snow-ice interface, as higher brine volume fractions are associated with the higher temperatures (see Section 3.5.3). This could also explain the higher polarization difference at higher surface temperatures for the 6.8 GHz channels compared to 10.65 and 18.7 GHz as the brine permittivity is higher at this lower frequency (Section 3.5.3). The Tbs at 18.7 GHz are about 10 K higher than at the lower two frequencies, similar to what is observed during science flight 1. Within the ranges 250K–254 K and 256K–258 K the Tb to ice temperature relation does not change a lot and is almost flat. This is the case at all frequencies and polarization and may be due to different ice types, e.g. less saline ice. Since the ice surface temperature span of science flight 2 is quite narrow with only 8K, also an instrument drift of the infrared camera between the 5 minute interval of NUC-calibrations may alter the interpretability of the relation in these narrow temperature ranges. The absolute accuracy of the IR camera is only 2 K. However, the precision is 0.03 K (see **Table 2**).

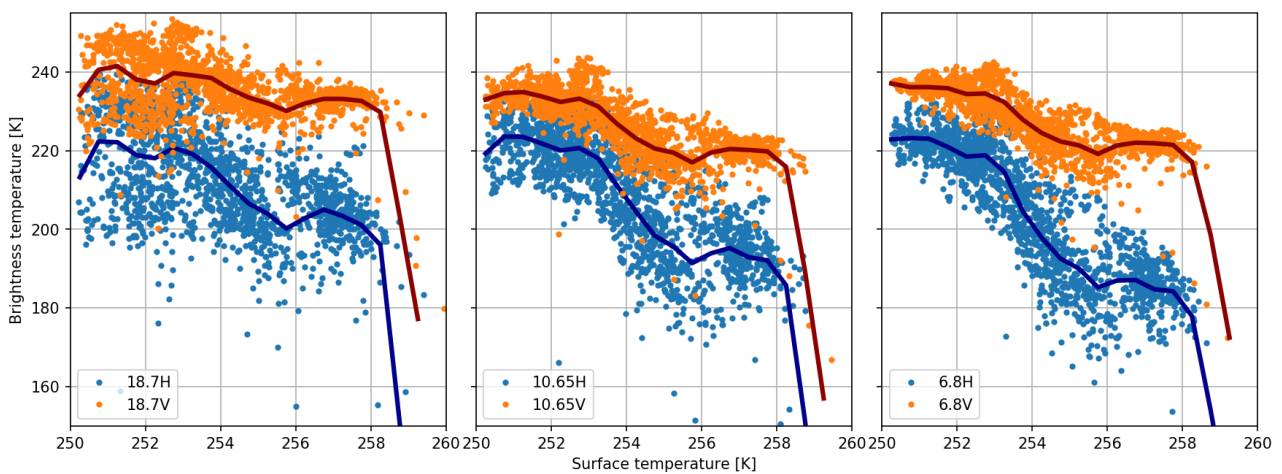


**Figure 18:** HUTRAD Tbs versus thermal camera surface temperature for the three different channel frequencies measured during science flight 2 on 7th March 2019 to the Barents Sea.

**Figure 19** a similar analysis for science flight 3. Much less data taken over entirely ice covered 6 GHz footprint sizes is available for this flight. The surface temperatures indicate relatively warm conditions compared to the previous two flights, which can be expected for the more southerly conditions and higher water temperatures of the region south-east of Storfjorden. The Tb scatter across all frequencies is reduced while the same anticorrelation and polarization difference behaviour of Figure 4-8 can be seen here as well. The pronounced steeper decrease of brightness temperatures at horizontal polarization compared to the decrease at vertical polarization with increasing temperatures can be associated also to the brine volume increase at the snow-ice-interface and the observation geometry: The incidence angle of the radiometer is close to the Brewster angle of the interface transition from ice through snow to air. Vertical polarized radiation passes this interface with significantly less reflection (see Section 3.5.3)

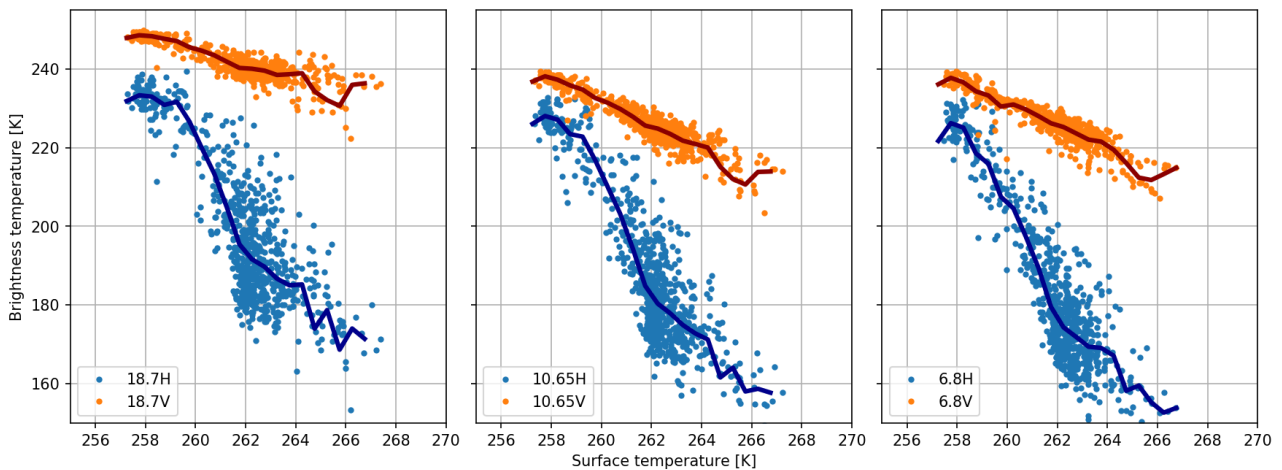


**Figure 19:** HUTRAD Tbs versus thermal camera surface temperature for the three different channel frequencies measured during science flight 3 on 8th March 2019 south-east of Storfjorden.

### 3.5.3 Model support for interpretation of HUTRAD data compared to thermal IR data

To explain some of the effects and anticorrelation between the microwave TBs and IR temperatures discussed in Section 3.5.2 we use a microwave emissivity model. Be reminded that we excluded all open water cases for the analysis in Section 3.5.2 and thus the Tb to IR relations have to be explained in the context of a sea ice-snow-air interface system.

A simple emissivity model is already suitable to explain some of the effects seen in the comparison of the HUTRAD data with the thermal images. First, the model consists of the Fresnel equations for modeling the interface transitions and the assumption of having neither emission nor volume scattering in the snow. As a general relation one can summarize that with higher permittivity difference between adjacent interfaces, the transmissivity of radiation (emissivity) decreases.

Since the permittivity plays such an important role for the emission, the second part is the modeling of the ice and snow permittivity. The brine volume fraction in the ice was found to be a well defined relation of temperature and salinity for the salt constituents of seawater [Assur, 1960] shown in **Figure 20** in the upper left. Brine volume fraction increases strongly with increasing temperature and salinity, which is more pronounced at both, higher temperatures, and higher salinity. While the permittivity of pure ice is pretty

constant across microwave frequencies (about  $\epsilon_{ice}=3.19$ ), the permittivity of brine is much higher (in the order of  $\epsilon_{brine}=10$  to  $\epsilon_{brine}=50$ ) and quite variable with frequency and temperature (**Figure 20** lower left). This variation causes a large part of the difference of microwave emission of sea ice at different frequencies. A dielectric mixture model is used to combine the ice and brine and to calculate the permittivity of sea ice. In this study a dielectric mixture model, assuming random needle shaped brine inclusions in the sea ice, is used. Note that the choice of the mixture model has a high impact on the resulting sea ice permittivity. However, for simplicity one single dielectric mixture model is used here. While the choice of the inclusion geometry is sort of arbitrary, the sea ice permittivity increase with temperature is independent of the inclusion geometry. Consequently, the emissivity of the sea ice and its relation to change in temperature can be calculated. **Figure 20** on the right shows this relation in the same manner as **Figure 17** to **Figure 19** for easier comparison but includes different salinity conditions of  $S=5\text{ppt}$  (representative for bulk sea ice) to  $S=20\text{ppt}$  (brine layer on top of sea ice). In contrast to **Figure 17** to **Figure 19**, here the sea ice-snow interface temperature is shown, which under cold air temperature conditions is higher than the snow-air-interface temperatures measured by the infrared camera. However, the modeled  $T_b$  to temperature relationship shows a similar behaviour as the measured  $T_b$  and IR temperatures:  $T_b$  and temperature are anticorrelated and  $T_b$  drops significantly above a certain temperature range. The decrease of brightness temperature with increasing temperature in the simulations is more pronounced in the higher temperature and higher salinity regime. In low salinity conditions, the dotted lines in **Figure 20**, the inverse relation of physical temperature to brightness temperature is only visible in the highest temperatures, especially at vertical polarization. In horizontal polarization at higher salinities, in contrast, the inverse relationship of temperature to brightness temperature is seen across the modeled temperature range  $>260\text{ K}$ .

Since the brine permittivity (and thus the sea ice permittivity) scales with frequency (**Figure 17** lower left), the lowest brightness temperatures can be seen at 6.8 GHz (right), similar as in the science flights in **Figure 18** and **Figure 19**. The relative variations of brightness temperatures with physical temperatures and frequencies can be described with this simple model only using the Fresnel equations and empirical models for the brine and ice permittivity. On the other hand, the absolute differences between the observed brightness temperatures and the modeled ones, show that a more sophisticated modeling study is required to get the particular microphysical details of the ice conditions. Currently missing effects and uncertainties comprise knowledge and modeling of snow-ice-interface temperature/snow thickness, brine inclusion geometry, surface scattering, volume scattering among other effects.

In conclusion, due to the strong dependence of brine volume fraction on temperature and the associated change in sea ice permittivity with temperature, an anticorrelation of microwave brightness temperature to physical temperature can be modeled and is also observed in the CIMREx data. This is counterintuitive to the basic definition of brightness temperature as  $T_b = \epsilon T$ , where  $T_b$  linearly depends on the physical temperature  $T$ , i.e. they are positively correlated. However, this equation omits the strong dependence of emissivity  $\epsilon$  on temperature  $T$ , which, as shown here, can result in a complex relationship between  $T_b$  and  $T$ .

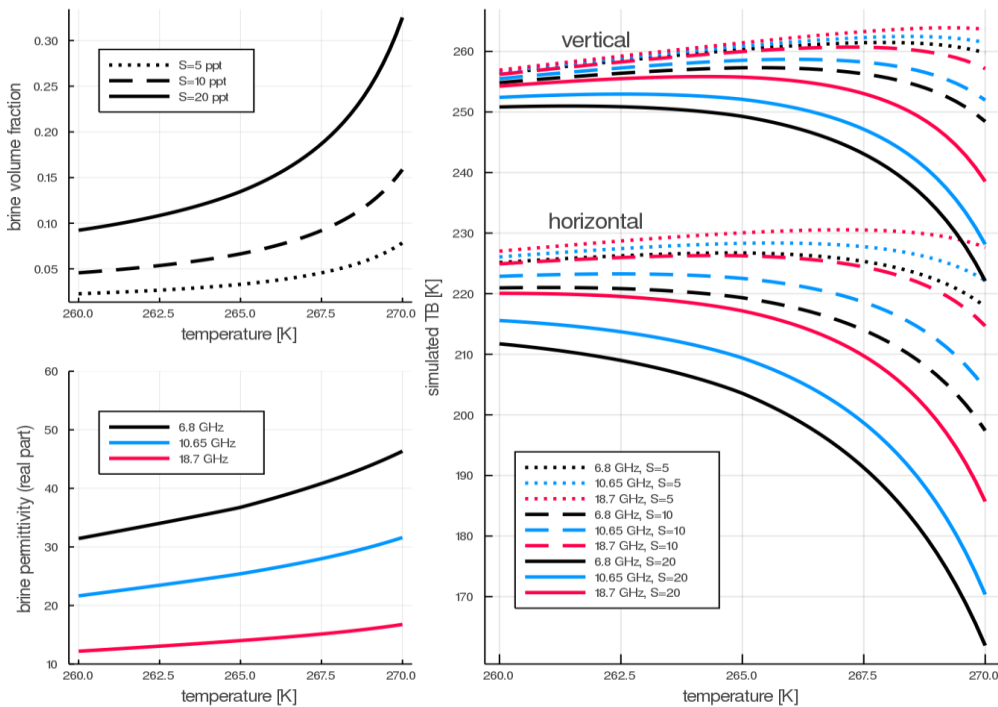


**Figure 20:** Model data showing the influences of the brine permittivity difference at the snow/ice interface on brightness temperatures at the three HUTRAD channel frequencies

### 3.5.4 Case study - HUTRAD Tbs of thin ice

In some of the flights, special cases can be found where an entire footprint is covered by a specific ice type. This case study picked one single infrared image and had a closer look at the infrared scene together with the brightness temperature measured by HUTRAD during the transfer flight 3 (**Figure 21**). Different types of ice are seen in the image; on the left and bottom right some older/thicker ice is seen with some already overfrozen leads and newly formed ice on the right. The warmest part is supposedly a relatively fresh lead of about 250 m width reaching from bottom left to top right of the infrared image. Close to the HUTRAD footprint, a gradient in temperature with increasing temperatures from left to right, i.e. in flight direction, is visible in the lead. This pattern is probably caused by a wind direction blowing from the right causing the water to cool down and accumulate ice towards the left part of the lead. This is a typical scene of ice formation in a polynya or, as seen here, in an open lead. While it is hard to estimate the given early ice type from the thermal image it is most likely a variant of grease ice or nilas, i.e. below 10 cm thickness. Most of the Tbs from HUTRAD drastically decrease on the step from the old thin ice into the thin ice area, mainly at the horizontal polarization. Interestingly this is not what is seen for the 18.7 GHz vertical polarization as it even increases slightly while its horizontal part already decreases. Continuing the track across the thin ice towards open water, finally also the 18.7 GHz vertical polarization drops. This effect is seen in a couple of other thermal images and HUTRAD combinations in similar situations. Traditionally a decrease of horizontal polarization while maintaining the vertical value is associated with a flat smooth surface with a high permittivity difference, however this would apply also to lower frequencies. Here the lower frequencies show a drop in vertical polarizations. This might be explained by saturation of radiation with increase of ice thickness: radiation penetrating from the water into the ice is higher at higher frequencies (lower permittivity

difference, **Figure 20** left) and also the emission within thin ice is higher for higher frequencies (smaller penetration depth). This special situation would be interesting to model and to understand how it may affect larger scale algorithms for ice concentration and snow thickness retrievals from satellites. However, on the scale of a satellite footprint it is unlikely to find homogenous areas of thin ice to exploit this effect and the higher spatial resolution observations from HUTRAD can be very beneficial to study such relationships and estimate their influence on larger scales.

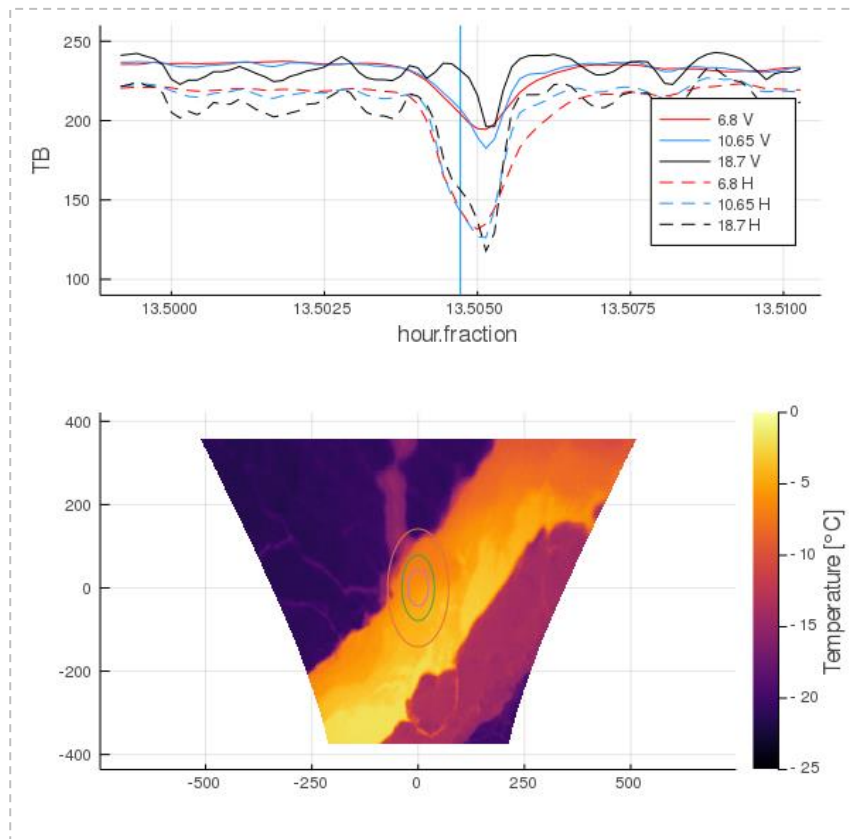


**Figure 21.** Case study: thin ice observed by HUTRAD and the infrared camera.

### 3.5.5 Conclusions on combination of HUTRAD and infrared camera

The combination of the HUTRAD radiometer together with the infrared camera enabled interesting comparisons of specific ice surface types and also allowed additional filtering for homogenous ice surface areas. A wide angle lens was chosen for the IR camera in order to see more of the ice surrounding the HUTRAD footprints. This will also help in case of a future manual classification of the dataset. The HUTRAD footprints are fixed within the infrared image which allows an easy comparison. The HUTRAD brightness temperatures are grouped by ice classes characterized by average physical temperature on the footprints estimated from the infrared images. The open water and thick ice class showed low variability on 6.8 GHz which encourages an ice concentration retrieval algorithm based on this frequency. The direct comparison of the infrared temperatures with the HUTRAD brightness temperatures showed anticorrelation on all channels, which can be explained e.g. by high salinity. In this experiment, sea smoke from open water areas potentially contaminated some of the infrared based surface temperature results. Thus some of the higher scatter of the HUTRAD brightness temperatures may be due to that for the intermediate ice classes and at lower surface

temperatures. A case study over thin ice found a surprisingly high vertical polarized radiation at 18.7 GHz while the horizontal brightness temperatures and the brightness temperatures of all other channels dropped when entering the thin ice area from thick ice as expected.

## 4 Conclusions and Recommendations

The Copernicus Space Component (CSC) Expansion programme includes six High Priority Candidate Missions (HPCM) for future new Sentinel satellites identified as priorities to be implemented in the coming years. One of the candidate missions is the Copernicus Imaging Microwave Radiometer (CIMR) mission (Kilic et al., 2018). CIMR is expected to deliver continuity and improvement on observations of key sea ice parameters (including sea ice extent, sea ice concentration, thin ice thickness, and ice drift) and sea surface temperature (SST). In order to meet these goals, CIMR would provide observations of brightness temperatures at L-, C-, X, Ku- and Ka-bands at high spatial resolution using a large real-aperture antenna (>7 m). Especially the C-band channels will provide sea ice concentration (SIC) at higher accuracy than available today while the Ku/Ka-band channels will provide SIC at below 5 km spatial resolution and at the same time keeping an accuracy below 5%. The L-band channel, which amongst other applications, will provide ability to estimate thin sea ice thickness. Compared to e.g. the Advanced Microwave Scanning Radiometer 2 (AMSR2), CIMR observations from C- to Ka-bands would be delivered at unprecedented spatio-temporal resolution and accuracy, while the L-band observations would provide continuity to present experimental L-band sensors on board the Soil Moisture and Ocean Salinity (SMOS) and Soil Moisture Active Passive (SMAP) missions.

In order ESA initiated the CIMR Arctic Airborne Campaign (CIMREx) to support CIMR geophysical retrieval algorithm development and to aid tradeoff analyses in instrument design. CIMREx was designed to provide quantitative reference information to help study trade-offs regarding the resolution of the space-borne system and mission complexity and cost. CIMREx aimed to support CIMR end-to-end simulation activities by providing realistic reference brightness temperature measurements over large areas of the Arctic at CIMR frequencies, finally enabling to document the total signal at spaceborne resolutions in terms of sub-pixel scale components. In order to achieve this, CIMREx operated airborne radiometers at 6.8, 10.65 and 18.7 GHz over the Arctic Ocean, capturing a variety of sea ice and ocean conditions.

The CIMREx campaign was conducted between February 28-March 11, 2019. The study region north of Svalbard and along the East Greenland Current included different ice types and snow conditions. A heritage instrument, the multi-frequency, dual polarization Helsinki University of Technology Radiometer (HUTRAD) was refurbished and refitted on a de Havilland Canada DCH-6 Twin Otter aircraft for the campaign. The aircraft sensor complement included also cameras and a high-definition thermal imaging instrument, providing quantitative reference of ice conditions.

This report provided a first analysis of data collected during CIMREx, including a comparison with collocated AMSR-2 footprints for each common channel, a comparison with HUTRAD brightness temperatures to ice types identified from thermal camera imagery, an analysis of the observed anticorrelation between HUTRAD Tb and thermal camera surface temperature, as well as an analysis of HUTRAD calibration uncertainties during the campaign. The following summarizes the main findings of this report:

Regarding HUTRAD data and calibration (Section 3.1):

- Temperature control of HUTRAD receivers, critical for calibration accuracy, was maintained to within +/- 1 °C for all science flights and for most transfer flights. Depending on the receiver, the fluctuation of temperature can cause an error of up to 3 K in calibrated antenna temperatures (**Figure 8**). It may be possible to correct for these fluctuations in processing of the data. However, this is not done in the currently delivered data, and more calibration tests would be preferable to determine the best post-processing method.

- During CIMREx science flights, pre- and post-flight calibration tests indicated that the MAE (mean average error) of HUTRAD was on average below 2 K for all channels, when considering the cold calibration target at 77 K. For ambient temperature calibration targets (closer to sea ice brightness temperatures), errors were below 1 K (**Table 4**). During transfer flights, calibration checks indicated an uncertainty of < 2K for the hot calibration loads.
- Calibration errors may not reveal the whole uncertainty of the collected airborne data. A large apparent bias at vertical polarization when comparing HUTRAD data to AMSR2 over open water (**Figure 11, Table 7**) may be an indication of distortion of the antenna beam patterns and/or reflections caused by the aircraft airframe. This possibility was not tested during the campaign due to lack of time and a suitable test environment. It should be noted that the routine two point calibration is not sensitive to the possible beam pattern distortions since calibration targets are placed directly in front of the antenna aperture (**Figure 4**)

Sections 3.2 and 3.3 provided a comparison of collocated HUTRAD data to AMSR2 brightness temperatures, and Section 3.4 a comparison of “forward and backward legs” measured during science flights:

- The high standard deviation of HUTRAD measurements during all flights demonstrate the high spatial variability of sea ice Tbs in the Marginal Ice Zone (MIZ) around Svalbard and also for the older, deformed ice in the East Greenland Current during winter conditions.
- While atmosphere may provide a contributing factor, surface Tb variability caused by the diverse ice situation in the MIZ can be considered the main cause for the high HUTRAD standard deviations within the AMSR2 footprints and also for the differences in mean and linear regression between HUTRAD and AMSR2.
- However, measurements over open water show (**Figure 11, Table 7**) that there is a potential bias between 14 - 25 K for the vertical Tb values at C and X-band between AMSR2 and HUTRAD. Considering the radiometric uncertainties and differences in footprint coverages such a difference can be expected. **However, reflections from the aircraft airframe may be a contributing factor**
- Biases in the order of 0.5–2 K and standard deviation above 10 K were apparent between the forward and backward flown transects (**Figure 13**). These differences are higher than the expected radiometric resolution of <0.3 K of the HUTRAD radiometer (**Table 1**), while being within the expected calibration accuracy (**Table 4**). However, already small changes in the open water/thin ice fraction within the footprint between the forward and backward flight, which did not always overlap, will have large effects on the measured brightness temperature. A better pointing accuracy to achieve overlap and non-moving, i.e. fast ice, would be required to fully assess the impact of observation geometry on Tb.

Section 3.5 provided an analysis of HUTRAD brightness temperatures against IR camera imagery.

- Different ice types derived from thermal camera imagery are also apparent in HUTRAD brightness temperatures across all channels (**Figure 16**)
- A strong negative correlation between Tb and IR surface temperature is noted across all channels (**Figure 17, Figure 18 and Figure 19**)
- While counterintuitive at first, this can be associated to the strong dependence of brine volume fraction on temperature and the associated change in sea ice permittivity with temperature, ~~and~~ which is confirmed with a simple emission model (Section 3.5.3)

Regarding possible future campaigns, it is recommended that:

- To fully exploit the capability of the HUTRAD system, the 36.5 GHz receiver should be added to the refurbished system, which would make HUTRAD comparable to CIMR (besides the L-band). This would enable further studies into, in particular, snow cover on seas ice and the Ku/Ka-band sea ice concentration algorithms.
- Possibilities to further improve HUTRAD temperature stabilization should be considered, as well as further tests assessing possibility to compensate for temperature changes in case of loss of thermal stability.
- The effect of the airborne platform on possible HUTRAD beam pattern distortions should be thoroughly explored. The possibility to locate the antennas outside the airframe proper (under a radome) should be considered.
- For optimal performance liquid nitrogen should be made available for calibration during all flights where science data collection is anticipated. Sufficient time for calibrations during e.g. refueling stops should be anticipated in the flight plans
- A scanning lidar instrument in addition to the IR and optical cameras would support analysis of ice conditions, providing an estimate of surface roughness and ice freeboard. Together these instruments would provide ancillary information about sea ice type and ice thickness, which would aid HUTRAD and thus CIMR data interpretation.

## 5 References

Assur, A. 1961. Composition of sea ice and its tensile strength U.S. Army Snow, Ice and Permafrost Research Establishment, Corps of Engineers, Wilmette, Ill..

Forsberg, R., A. Stokholm, J. Lemmetyinen, G. Spreen, S. Nyman and S. Salo, 2019. Data Acquisition Report. Issue 1 Revision 2, 29 August 2019.

Lavergne, T.: CIMR compared to other PMRs: Channels and Spatial resolution, <https://doi.org/10.6084/m9.figshare.7177730.v1>, [https://figshare.com/articles/CIMR\\_compared\\_to\\_other\\_PMRs\\_Channels\\_and\\_Spatial\\_resolution/7177730](https://figshare.com/articles/CIMR_compared_to_other_PMRs_Channels_and_Spatial_resolution/7177730), 2018.

Lemmetyinen J., C. Derksen, J. Pulliainen, W. Strapp, P. Toose, A. Walker, S. Tauriainen, J. Pihlflyckt, J-P. Kärnä, and M. Hallikainen, 2009. A comparison of airborne microwave brightness temperatures and snowpack properties across the boreal forests of Finland and western Canada. *IEEE Trans. Geosci. Remote Sens.*, 47(3): 965-978

Lemmetyinen, J., Derksen, C., Toose, P., Proksch, M., Pulliainen, J., Kontu, A., Rautiainen, K., Seppänen, J., and Hallikainen, M., 2015. Simulating seasonally and spatially varying snow cover brightness temperature using HUT snow emission model and retrieval of a microwave effective grain size. *Remote Sens. Environ.*, 156, 71-95.

Lemmetyinen, J., G. Spreen, R. Forsberg, R. Tonboe, 2019. D2: Campaign Implementation Plan. Issue 1, revision 0, 15 January 2019.

Uusitalo, J., H. Servomaa, S. Salo, H. Nguyen, J. Lahtinen and K. Havia, 2019. D1: System Readiness and Test Report. Issue 1, Revision 2, March 20, 2019, Harp Technologies Ltd.

Kilic, L., Prigent, C., Aires, F., Boutin, J., Heygster, G., Tonboe, R. T. et al., 2018. Expected performances of the Copernicus Imaging Microwave Radiometer (CIMR) for an all-weather and high spatial resolution estimation of ocean and sea ice parameters. *Journal of Geophysical Research: Oceans*, 123. <https://doi.org/10.1029/2018JC014408>

## Appendices

## **Appendix 1: System readiness and test report**

# CIMR Airborne Arctic Campaign (CIMREX)

## HUTRAD 2.0 Refurbishment ESA Contract no. 000125503

### D1: System Readiness and Test Report

---

The copyright of this document and all information in it is the property of Harp Technologies Ltd. Excluding any specific release conditions stated below, no part or whole of this document may be copied or reproduced without the written permission of Harp Technologies Ltd.

Specific Release Conditions: This document has been specifically intended for use by the European Space Agency and the Finnish Meteorological Institute and its subcontractors in ESA Contract no. 000125503. Therefore, its circulation shall be restricted to the members of the receiving organization. It may not be used or copied, in whole or part for any other Governmental, non-Governmental or commercial purpose without the written agreement of Harp Technologies Ltd.

This page is intentionally blank

## TABLE OF CONTENTS

<b>TABLE OF CONTENTS</b> .....	<b>3</b>
<b><i>DOCUMENT SIGNATURE TABLE</i></b> .....	<b>4</b>
<b><i>DISTRIBUTION LIST</i></b> .....	<b>4</b>
<b><i>DOCUMENT STATUS SHEET</i></b> .....	<b>4</b>
<b><i>MAIN CHANGES SINCE PREVIOUS ISSUE</i></b> .....	<b>4</b>
<b>APPLICABLE DOCUMENTS</b> .....	<b>5</b>
<b>REFERENCE DOCUMENTS</b> .....	<b>5</b>
<b>1. INTRODUCTION</b> .....	<b>7</b>
<b>2. ORIGINAL HUTRAD SYSTEM</b> .....	<b>8</b>
2.1 SYSTEM DESCRIPTION .....	8
2.2 STATUS OF HUTRAD LF .....	11
<b>3. REFURBISHMENT OF HUTRAD 2.0</b> .....	<b>13</b>
3.1 RECEIVERS .....	13
3.2 CONTROL PROCESSING UNIT .....	16
3.3 MONITORING WORKSTATION AND LOCAL AREA NETWORK .....	17
3.4 UNINTERRUPTIBLE POWER SUPPLY .....	17
3.5 CABLE HARNESS .....	17
3.6 SUPPORT FRAME.....	18
3.7 OVERALL SYSTEM .....	18
<b>4. TESTING</b> .....	<b>19</b>
4.1 RADIOMETRIC RESOLUTION AND STABILITY .....	19
4.2 TEMPERATURE STABILITY .....	21
4.2.1 <i>Stability Test in Cold Test Laboratory</i> .....	21
4.2.2 <i>Stability Tests in Room Temperature</i> .....	24
<b>5. CONCLUSIONS</b> .....	<b>28</b>

## Document Signature Table

	Name	Function	Signature	Date
<b>Author(s)</b>	Josu Uusitalo	Design Engineer		March 13, 2019
	Henri Servomaa	Design Engineer		March 13, 2019
	Sampo Salo	Design Engineer		March 13, 2019
	Huy Nguyen	Design Engineer		March 13, 2019
	Janne Lahtinen	Design Engineer		March 13, 2019
	Kimmo Havia	Design Engineer		March 13, 2019
<b>Verification</b>	Janne Lahtinen	Project Manager		March 20, 2019
<b>Approval</b>	Janne Lahtinen	Project Manager		March 20, 2019

## Distribution List

Name	Organization
Tânia Casal*	European Space Agency
Malcolm Davidson *	European Space Agency
Craig Donlon *	European Space Agency
Juha Lemmetyinen *	Finnish Meteorological Institute
Configuration Control *	Harp Technologies Ltd
Josu Uusitalo *	Harp Technologies Ltd
Janne Lahtinen *	Harp Technologies Ltd
Huy Ngueun	Harp Technologies Ltd
Sampo Salo	Harp Technologies Ltd
Henri Servomaa	Harp Technologies Ltd External

\* Electronic copy

## Document Status Sheet

Issue	Date	Comments
1.0	March 13, 2019	Initial issue
1.1	March 19, 2019	Initial issue, first revision
1.2	March 20, 2019	Initial issue, second revision

## Main Changes since Previous Issue

Section	Modified Parts
Cover Page	Deliverable number corrected (D1)

## Applicable Documents

N/A

## Reference Documents

- [RD-1] M. Hallikainen, M. Kemppinen, K. Rautiainen, J. Pihlflyckt, J. Lahtinen, T. Tirri, “Airborne 14-channel microwave radiometer HUTRAD,” *IEEE 1996 International Geoscience and Remote Sensing Symposium Proceedings*, pp. 2285-2287, Lincoln, USA, 1996.
- [RD-2] K. Rautiainen, “The design and construction the radio frequency unit of an airborne microwave radiometer system” (in Finnish, original title: “Lentokäyttöisen mikroaaltoradiometrin radiotaajuusosien suunnittelu ja toteutus”), *M.Sc. Thesis*. Helsinki University of Technology, Espoo, Finland, 1996.
- [RD-3] J. Lahtinen, “Development of a polarization radiometer for remote sensing” (in Finnish, original title: “Polarisaatoradiometrin kehittäminen kaukokartoitukseen”), *M.Sc. Thesis*. Helsinki University of Technology, Espoo, Finland, 1996.
- [RD-4] T. Tirri, “Lentokonekäyttöisen radiometrijärjestelmän tiedonkeruu- ja mittausohjelmisto” (in Finnish), *M.Sc. Thesis*. Helsinki University of Technology, Espoo, Finland, 1996.
- [RD-5] J. Lemmetyinen, “Kaukokartoitusradiometrin toiminnan arviointi ja jatkokehitys” (in Finnish), *M.Sc. Thesis*. Helsinki University of Technology, Espoo, Finland, 2004.
- [RD-6] J. Pihlflyckt, “Control and measurement system for multi-channel microwave radiometer,” *M.Sc. Thesis*. Helsinki University of Technology, Espoo, Finland, 2007.
- [RD-7] F. T. Ulaby, R. K. Moore, and A. K. Fung, *Microwave Remote Sensing: Active and Passive, Volume I*. Reading, Massachusetts, USA: Artech House, 1981.

## ACRONYMS

AD	Applicable Document
CPU	Control Processing Unit
DGPS	Differential GPS
GNSS	Global Navigation Signal System
GPS	Global Positioning System
HUTRAD	Helsinki University of Technology RADiometer
IMU	Inertial Measurement Unit
INS	Inertial Navigation System
LAN	Local Area Network
NTS	Network Time Server
RD	Reference Document
TBC	To Be Confirmed
TBD	To Be Decided
UPS	Uninterruptible Power Supply
WP	Work Package

## 1. Introduction

This document is the system readiness and test report of HUTRAD 2.0 radiometer system, which was refurbished within *CIMR Airborne Arctic Campaign (CIMREx)* activity of the European Space Agency. This document has been prepared by Harp Technologies Ltd. The prime contractor of the activity is the Finnish Meteorological Institute (FMI). As part of the activity, existing 6.8 GHz, 10.65 GHz, and 18.7 GHz channels of a legacy HUTRAD radiometer system were repaired and refurbished into HUTRAD 2.0 to be used in CIMREx.

This document has been organised as follows: Chapter 2 presents the original HUTRAD system and the conducted refurbishment work is presented in Chapter 3. Test results are presented in Chapter 4. Finally, conclusions are made in Chapter 5.

## 2. Original HUTRAD system

### 2.1 System Description

The HUTRAD (Helsinki University of Technology RADiometer) airborne radiometer system was developed in the Helsinki University of Technology (now: Aalto University), Laboratory of Space Technology from 1994 onwards. HUTRAD included lower and higher frequency profiling radiometer systems, an imaging radiometer and an interferometric radiometer (HUT-2D). In the current contents, only the lower frequency (LF) profiling system (including 6.8 GHz, 10.65 GHz, and 18.7 GHz channels) is of interest. The first measurements with LF system were performed in the beginning of 1995. The HUTRAD system was repaired and improved during the years and airborne measurements were conducted until February 2014. A photograph of the LF and High Frequency (HF) profiling systems, installed into Short SC7 Skyvan research aircraft, is presented in Figure 1. The radiometers were designed to be mounted in the rear cargo bay of the Skyvan aircraft, on the edge of the ramp where the antennas could have an unobstructed view to the ground. The key parameters of HUTRAD are presented in [RD-1].



*Figure 1. The HUTRAD profiling radiometers of Aalto University installed into the rear cargo bay of the Short SC7 Skyvan research aircraft. The lower frequency unit (LF) is on the left, the higher frequency unit (HF) on the right.*

The mechanical frame of the LF unit was a rack that incorporated vertically stacked, individually thermally insulated enclosures for 6.8 GHz, 10.65 GHz and 18.7 GHz receivers. Each receiver was built on an aluminium deck (or tray). The receivers (in their enclosures) were situated on top of a Control Processor Unit (of the LF unit) so that the LF unit formed a single rack module with the size of a small refrigerator (weight: 85 kg). The antennas that were applied were parabolic and mounted outside the LF rack. The antennas were mounted to have approx. 50° incidence angle when the LF rack was standing on its feet. A photograph of backside of the LF and HF units is shown in Figure 2.

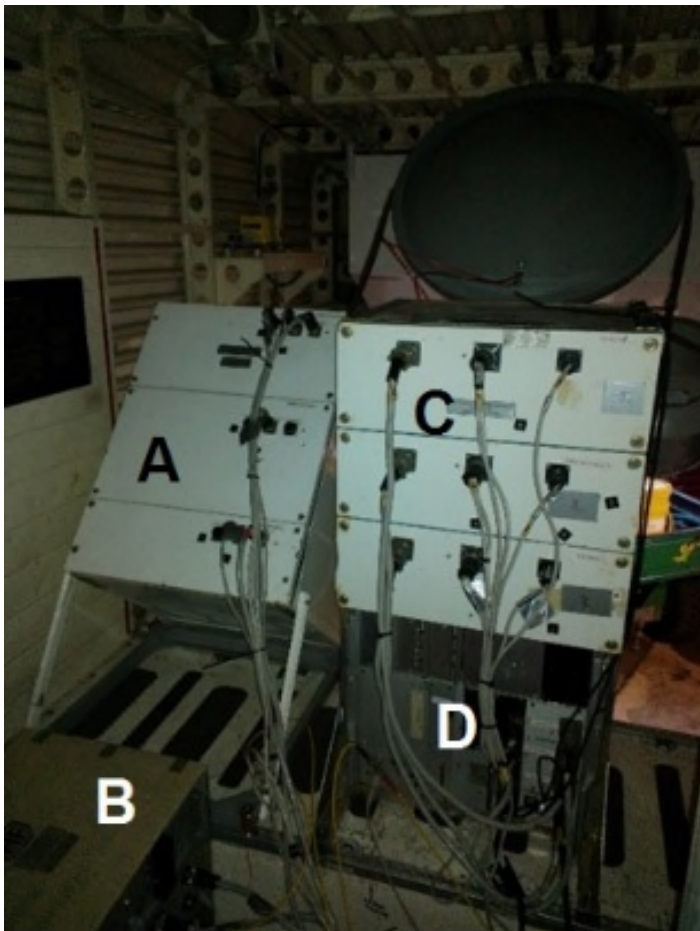


*Figure 2. A backside view of the HUTRAD profiling radiometers: A) the receiver rack module of the HF system, B) the Control Processor Unit rack module of the HF system, C) the receivers of the LF system, and D) the Control Processor Unit of the LF system.*

The main functions of the Control Processor Unit (CPU) were to collect the data from the receivers and to pass the data to the monitoring workstation to be stored. In practise, CPU was built around a 386-compatible PC card that applied MS-DOS operating system. In addition, the CPU generated all necessary secondary voltages for the receivers from the bus voltage of the aircraft. Also, it measured and controlled the physical temperatures of the receivers. The LF unit was connected with the monitoring workstation using a Local Area network (LAN). A schematic diagram of the (original) network of the HUTRAD system is presented in Figure 3. Please note that in the 2000s, the primary and secondary workstations,

running MS-DOS operating system and illustrated in Figure 3, were replaced with a single laptop computer (monitoring workstation) that applied Linux operating system. During measurements, the correct functionality of the radiometers could be observed with the monitoring workstation, which showed pseudo-calibrated radiometer data (retrieved with pre-determined calibration coefficients) and housekeeping data (receiver temperatures, temperature control data). The components of the HUTRAD measurement software are presented in Figure 4. Novell Netware protocol was used to synchronise the clocks of the CPU and the monitoring workstation. Therefore, the CPU had a Novell Netware client.

Beside the actual HUTRAD system, some supporting equipment were also needed: network time server, DGPS/INS localisation and attitude determination system, and 230 VAC inverter. The network time server provided the reference time for the system, obtained from GPS signal. Thus, the server needed a GPS antenna that it could be connected to. Also, a system to measure (and record) the location and attitude of the aircraft was needed. The latter was mandatory in order to compensate for the attitude changes of the aircraft in data post processing. Originally in Skyvan, a C-MIGITS DGPS/INS system of AISA instrument was used. Later on, it was replaced by another DGPS/INS system, which provided the location and attitude data. This data was stored in an additional laptop computer (i.e., not to the monitoring workstation of HUTRAD). The 230 VAC inverter was needed to generate the supply voltage for the time server, HUTRAD laptop, LAN hub, etc.

More details on the profiling radiometer system can be found in [RD-1], [RD-2], [RD-3], [RD-4], [RD-5], [RD-6].

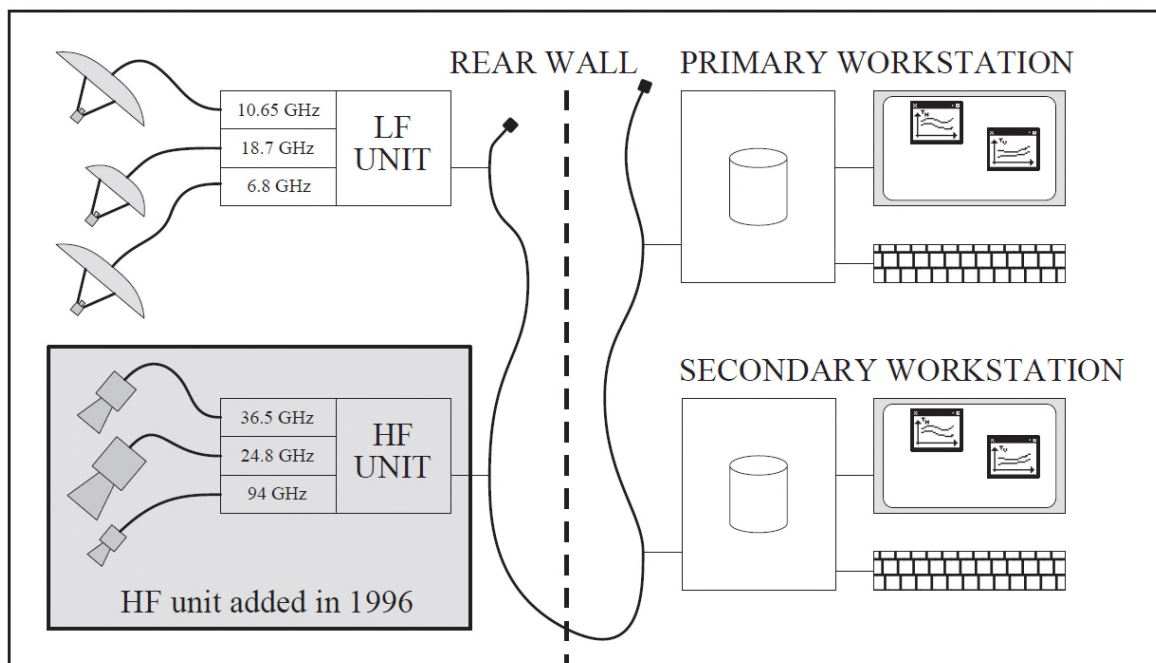


Figure 3. The (original) network of the HUTRAD system [RD-6]. Note that in 2000s, the primary and secondary workstations were replaced with a single laptop computer (monitoring workstation).

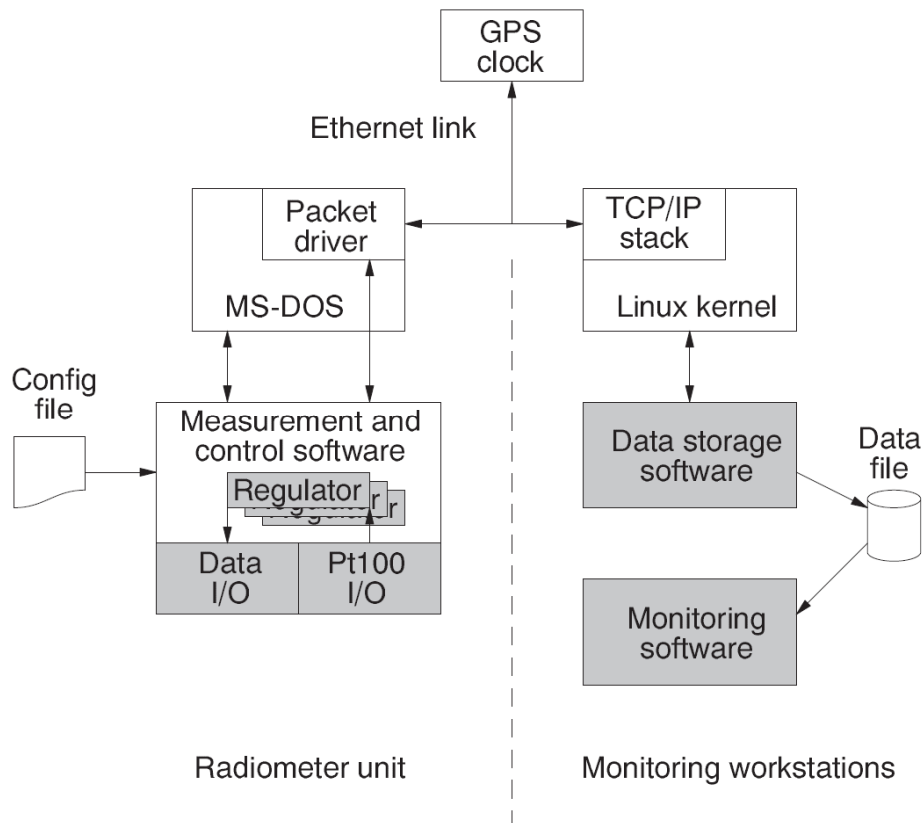


Figure 4. The components of the HUTRAD measurement software [RD-6].

## 2.2 Status of HUTRAD LF

The status of the HUTRAD LF system was tested in March 2018 by FMI and in June-September 2018 by Harp Technologies after the transfer of the system to company's premises. Combining these measurement results with earlier experiences, the following defects and problems could be identified:

### Receivers

- The Dicke switches of the 6.8 GHz receiver were not working properly (both V&H)
- The Dicke switches of the 18.7 GHz receiver were not working properly (both V&H)

### Antennas

- The parabolic antennas of the LF system were not compatible with the intended airborne platform (de Havilland DHC-6 Twin Otter)

### Control Processor Unit

- The Control Processor Unit of the LF system had several major problems: unreliable start-up, error messages, spontaneous booting, etc.

### Monitoring Workstation

- No direct problem was detected, but the workstation was a very old laptop (>10 years) and could fail any time due to old age

### **Local Area Network**

- Communication between the control processor units and monitoring workstation was unreliable and did not always start working.

### **Mechanical**

- The refrigerator type mechanical constructions of the LF system was not compatible with the intended airborne platform (Twin Otter)

### **Cable Harness**

- The cable harness was not long enough to be used in system configuration suitable for the intended airborne platform (Twin Otter). Also, some connector were working in unreliable manner (bad contact due to wear out).

### **Thermal Control**

- Unreliable functionality of the thermal control system.

### **Reference Time Generation**

- This system had been lost over the years (i.e., location could not be identified).

### **230 VAC Inverter**

- This system was lost (i.e., location could not be identified).

### **3. Refurbishment of HUTRAD 2.0**

As discussed in Chapter 2, the HUTRAD LF system was not mechanically compatible with the intended airborne platform (Twin Otter). In addition, several subsystems were not working or there are problems with their functionality. Also, some supporting systems were missing. Therefore, HUTRAD LF was refurbished as described below. This system is called HUTRAD 2.0.

#### **3.1 Receivers**

The receivers were inspected and disassembled to RF component level. The receivers were redesigned and completely rebuilt on new trays. Finally, the receivers were tested. Instead of the old single rack structure, the receivers were assembled into three 19" rack enclosures (height: 7U), one receiver in each. The enclosures were carefully thermally insulated. New dual-polarization (vertical and horizontal), lens loaded horn antennas were acquired and integrated with the receivers, i.e., they were accommodated inside the receiver enclosures. The receivers were assembled on a two-level tray that can be easily disassembled from the enclosure for receivers' repair and testing. For the receivers, the existing (old) RF components were applied, with the exception of Dicke-switches for 6.8 GHz and 18.7 GHz receivers. New switches were acquired and implemented and the control electronics was modified to produce the correct control voltages. Also, RF cable harness and wiring of the receivers was renewed.

The original components for the thermal stabilization were implemented in the new receiver enclosures. However, new Peltier elements were acquired and implemented. In addition, thermal heaters were implemented in each receiver to improve the thermal stabilization in very cold measurement conditions (-20°C and colder). These heaters can be switched on and off depending on conditions. CAD models of the designed 6.8 GHz, 10.65 GHz, and 18.7 GHz receivers are presented in Figure 5, Figure 6, Figure 7, respectively. Photographs of the assembled 6.8 GHz, 10.65 GHz, and 18.7 GHz receivers are presented in Figure 8, Figure 9, Figure 10, respectively.

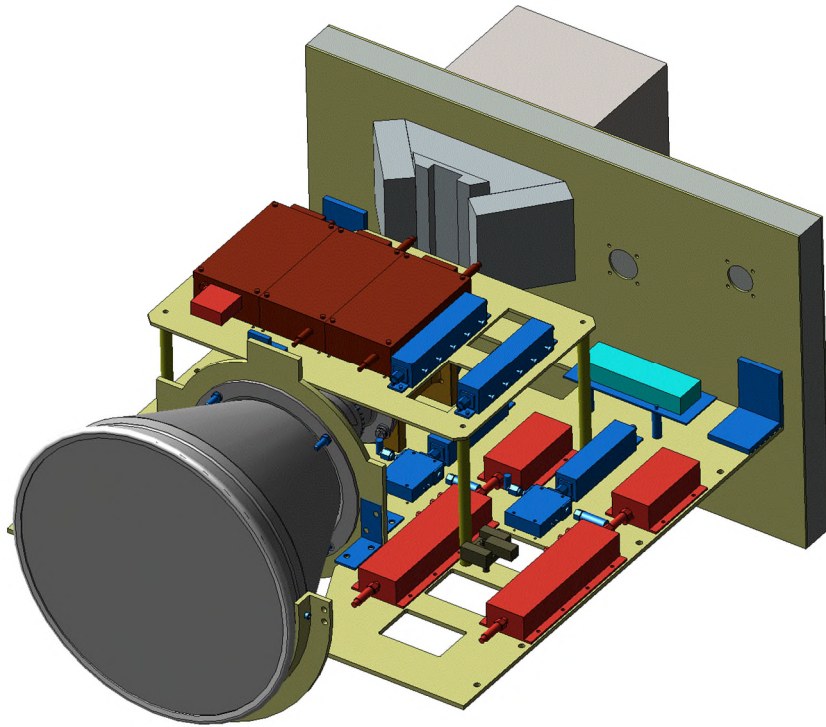


Figure 5. CAD model of the refurbished 6.8 GHz HUTRAD 2.0 receiver, without enclosure.

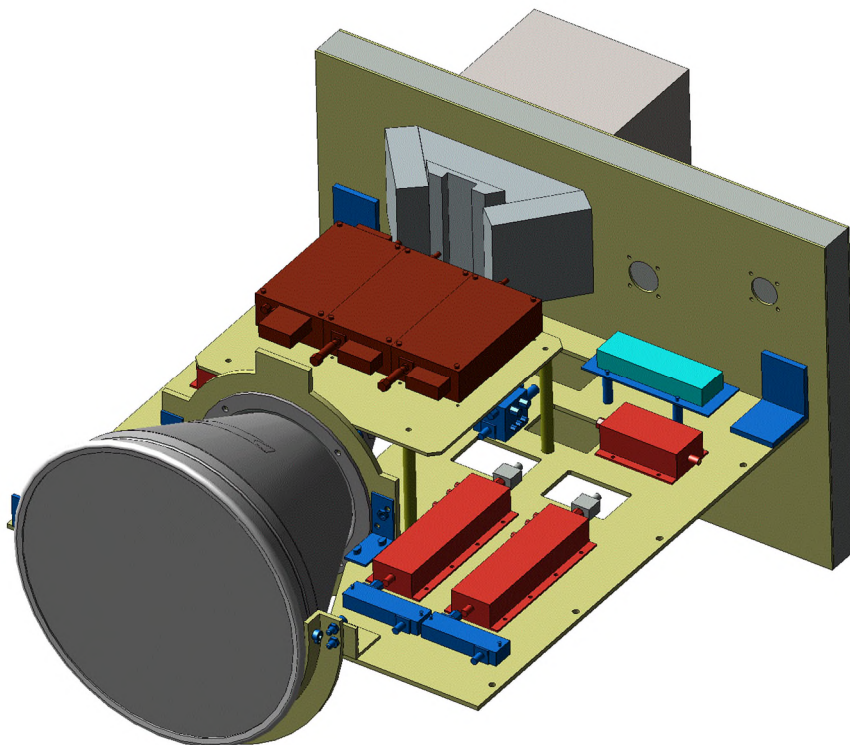
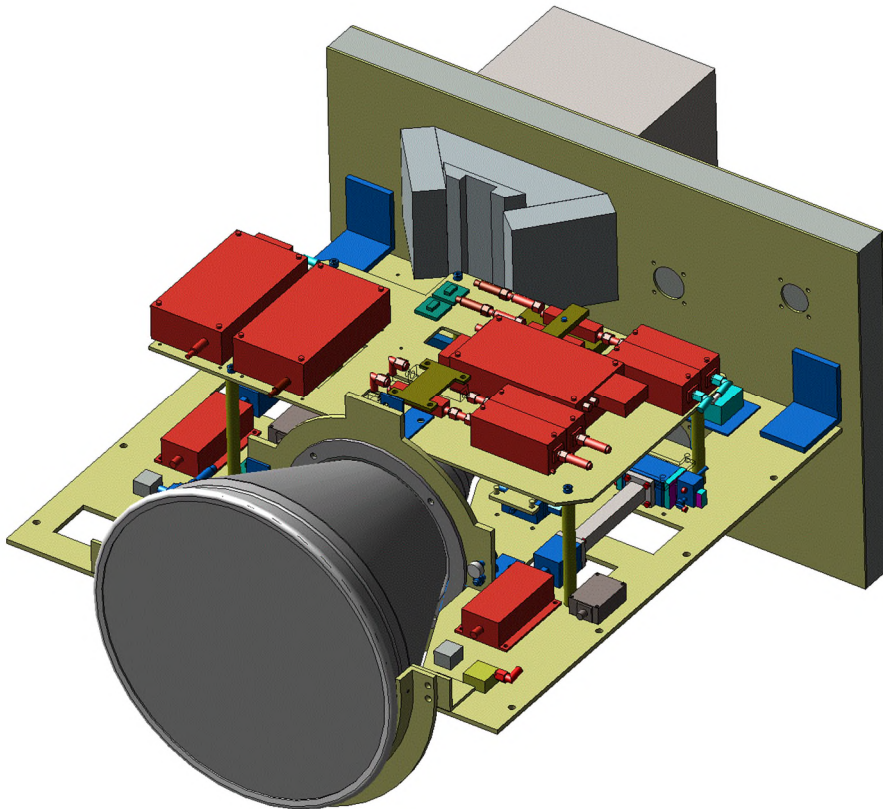


Figure 6. CAD model of the refurbished 10.65 GHz HUTRAD 2.0 receiver, without enclosure.



*Figure 7. CAD model of the refurbished 18.7 GHz HUTRAD 2.0 receiver, without enclosure.*

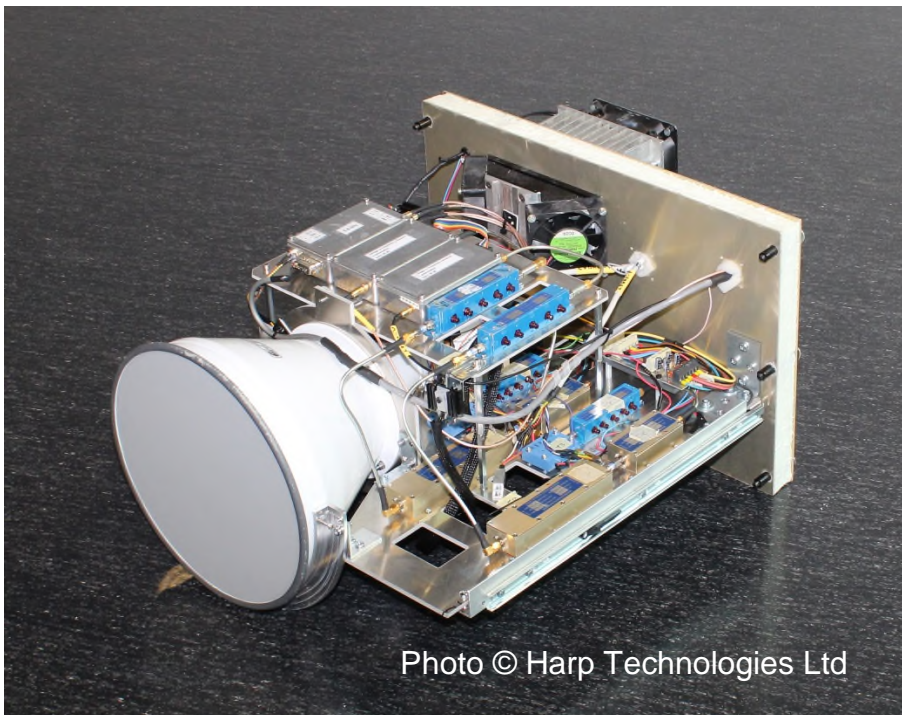
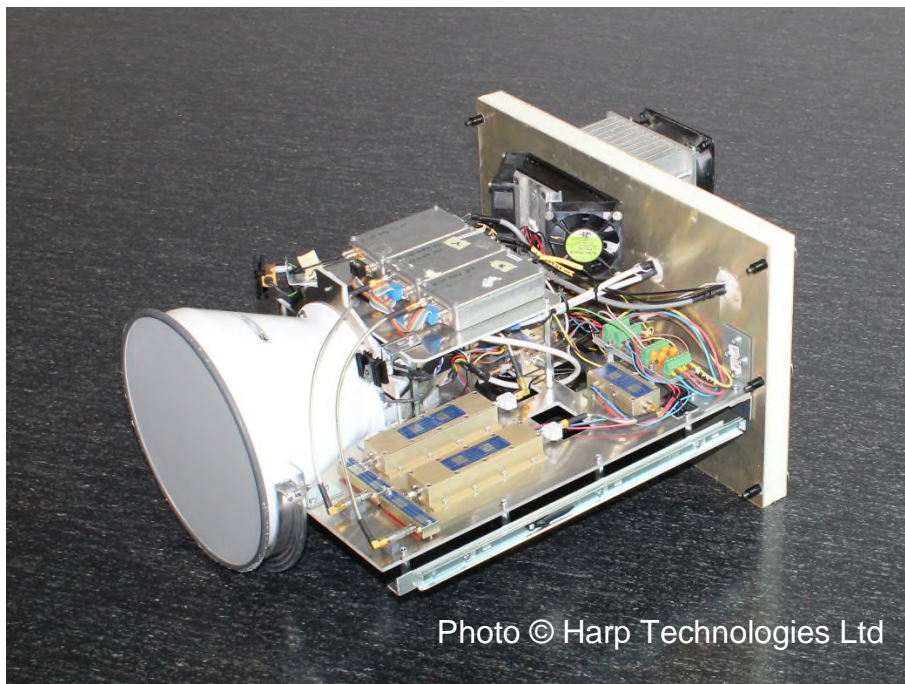
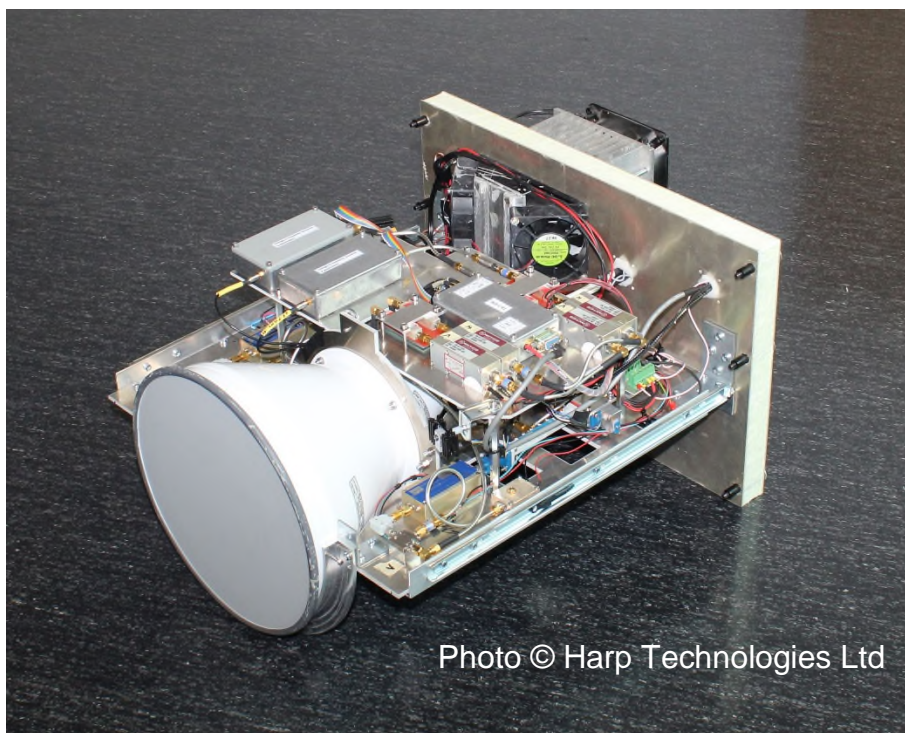


Photo © Harp Technologies Ltd

*Figure 8. Photograph of the refurbished 6.8 GHz HUTRAD 2.0 receiver, without enclosure.*



*Figure 9. Photograph of the refurbished 10.65 GHz HUTRAD 2.0 receiver, without enclosure.*



*Figure 10. Photograph of the refurbished 18.7 GHz HUTRAD 2.0 receiver, without enclosure.*

### **3.2 Control Processing Unit**

The Control Processing Unit (CPU) was thoroughly tested and inspected. The old mechanical housing was maintained but several modifications and repairs were

implemented. However, a 19" rack enclosure (height: 9U) was purchased to accommodate the mechanical housing of the CPU. A new power supply card was designed and implemented for the internal computer and the BIOS' battery of computer's motherboard was changed. Some repairs and re-configurations were done on the RTD cards, which are responsible for reading the radiometer and temperature data. Also, a GPS Network Time Server (NTS) and an ethernet switch were purchased and integrated into the CPU; in the original HUTRAD, these were external units that needed 230 VAC input. Also, the old CPU used old fashioned coaxial ethernet connector, while the new system enables to use (nowadays) standard RJ-45 connectors. Finally, cooling fans were implemented inside the CPU enclosure.

### **3.3 Monitoring Workstation and Local Area Network**

As discussed in Section 2.2, the functioning of the Local Area Network (LAN) was unreliable. Upon start-up, the connection between CPU and the monitoring workstation did not always establish. Re-starting did not typically help. The problem was investigated and it turned out to be related to the Novell Netware client used to synchronize the clocks between the CPU and the monitoring workstation. As discussed in Section 2.1, the original monitoring workstations using MS-DOS operating system were replaced by Linux-based system in 2000s. Novell Netware being a legacy system already in 2000s, full compatibility could not be achieved. Although this incompatibility could not be removed, a work-around was developed to start the network connection manually on the command line. This way, the network connection can be always established in a reliable way.

In addition, control and monitoring software of the monitoring workstation was transferred to a much newer laptop computer. Thus, two monitoring workstations are now on disposal: the new one (primary) and the old one (backup), which can be used if the primary laptop breaks.

### **3.4 Uninterruptible Power Supply**

During the development it turned out that unlike the old aircraft platform (Short Skyvan), the intended aircraft (Twin Otter) does not have batteries to power on the aircraft voltage bus while the engines are not running. Therefore, an Uninterruptible Power Supply (UPS) system was designed and developed. It is mountable into a 19" rack and it can support the HUTRAD in the time gap after the aircraft has been disconnected from the Ground Power Unit (GPU) and before the engines of the aircraft power on the aircraft voltage bus. The UPS includes two 1.3 Ah (24 V) batteries and it can support the operation of HUTRAD for more than five minutes after thermal stabilization has been reached.

### **3.5 Cable Harness**

The original cable harness was too short for the new instrument configuration. Also, temperature reading was not always reliable due to problems with the connectors. Therefore, a new cable harness was designed and manufactured to connect CPU and the receivers. In

order to improve reliability compared to the old system, robust full metal connectors (MIL connectors or similar) were selected as connectors.

### 3.6 Support Frame

The support frame is a mechanical structure that keeps the receivers in place and in correct orientation during measurements. The defined incidence angle for the antenna beams is 55° (from nadir). The frame was designed to be mounted on the floor of the aircraft, in the luggage compartment of the Twin Otter aircraft. Critical parts of the frame were manufactured from 4130 Cromo high strength steel while standard S235/S355 steel was used for non-critical parts. The frame was painted black to prevent corrosion.

### 3.7 Overall System

The overall HUTRAD 2.0 system is presented in Figure 11 below.

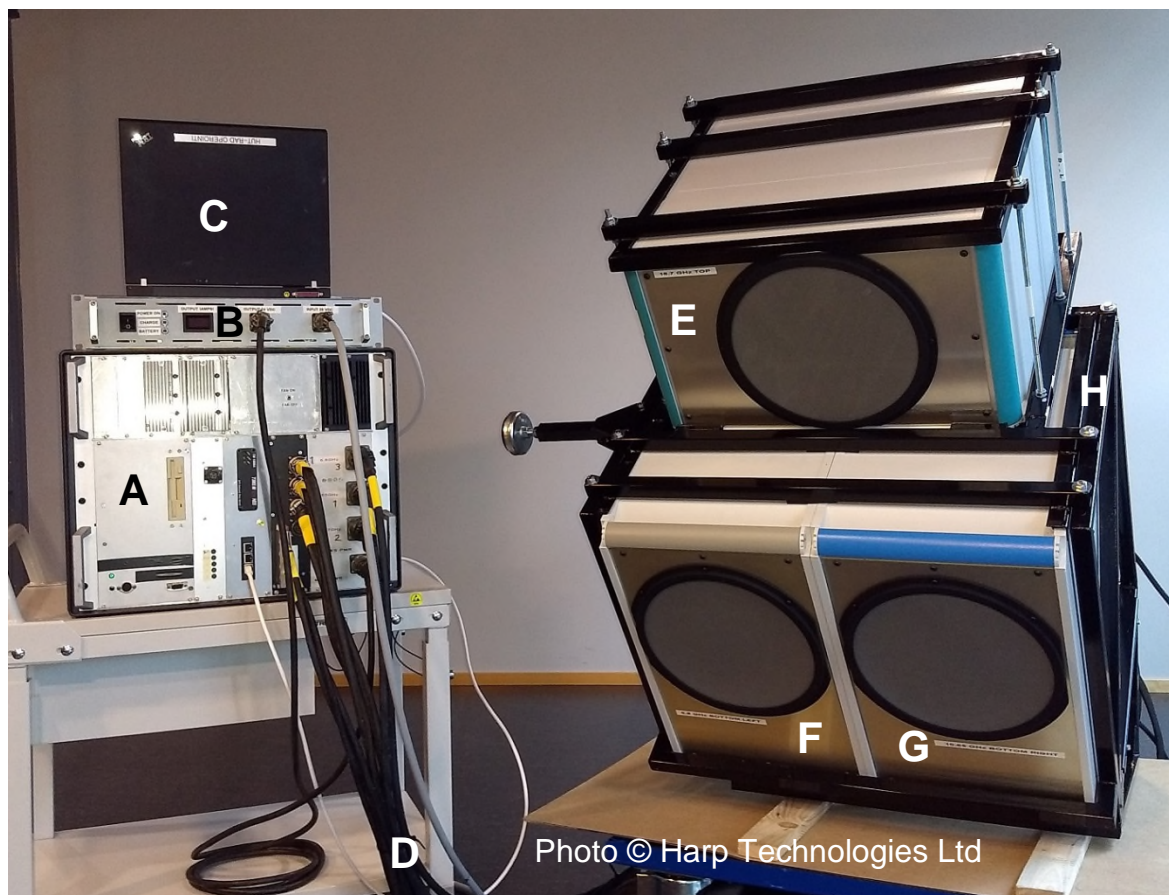


Figure 11. The overall HUTRAD 2.0 system: A) Control Processor Unit (CPU); B) Uninterruptible Power Supply (UPS); C) monitoring workstation; D) cable harness; E) 18.7 GHz receiver; F) 6.8 GHz receiver; G) 10.65 GHz receiver; H) support frame.

## 4. Testing

After completing the refurbishment of the receivers, CPU and other systems, the functionality of HUTRAD 2.0 was tested. In these tests, it could be manifested that the radiometers are functional, i.e. the receivers react to brightness temperature changes. Also, all radiometer and temperature data that were produced were correctly recorded into the monitoring workstation. After these functional tests, the following performance tests were conducted: radiometric resolution and stability of the receivers (described in Section 4.1) and thermal stability of the receivers (described in Section 4.2).

### 4.1 Radiometric Resolution and Stability

For testing of the radiometric resolution and stability, the receiver units were installed in their support frame, in the manner shown in Figure 11 on page 18. Two-point calibration of the radiometers was performed using hot and cold calibration targets (blackbody targets). For details of a two-point calibration, see [RD-7]. The cold calibration target was cooled with liquid nitrogen while the hot target was in ambient room temperature (22°C). Below, Table 1 displays the measured (raw) calibration data. Note that the unit of the raw radiometer data is Hertz (Hz). Note further that unlike other radiometers, the 6.8 GHz radiometer unit has a negative response slope. This feature existed also before the refurbishment.

For tests, the internal physical temperature of the receivers was set to 33°C (set value). This produced approximately 10°C difference ( $\Delta$ ) between the inside and outside temperatures of the receivers. Various other values of  $\Delta$  were also tested. There is a practical minimum of approximately  $\Delta \approx 2^\circ\text{C}$  due to limited cooling efficiency of the temperature stabilization system. On the high side, tests up to  $\Delta \approx 22^\circ\text{C}$  were conducted in room temperature, and  $\Delta \approx 30^\circ\text{C}$  was tested in cold (-20...-30 °C) external temperatures, as discussed in Section 4.2 below.

*Table 1. Radiometer output (raw) data in the calibrations; means and standard deviations (integration time 500 ms).*

Channel	Hot calibration (Hz)		Cold calibration (Hz)		Difference, Hot – Cold (Hz)
	mean	std	mean	std	mean
18.7 H	2170.3	0.9	1759.7	0.8	411
18.7 V	2548.0	0.8	2085.7	0.9	462
10.65 H	2878.0	1.8	2082.5	1.2	796
10.65 V	2508.9	1.5	1530.4	1.0	979
6.8 H	2485.1	0.9	3031.3	0.8	-546
6.8 V	2551.8	0.9	3306.4	1.1	-755

After calibration, the radiometric resolutions ( $\Delta T$ ) of HUTRAD 2.0 channels were determined by the standard deviation ( $\sigma$ ) of the radiometer data during hot load calibration. The determined radiometric resolutions are depicted in Table 2 below. For reference, the radiometric resolutions of the original HUTRAD, determined in mid-1990s [RD-2], are also presented. In addition, such equivalent change of the front-end loss has been approximated,

which would explain the difference between the measured radiometric resolution in these two measurements.

*Table 2. Determined radiometric resolutions of HUTRAD channels.*

Channel	$\Delta T$ (K) HUTRAD 2.0	$\Delta T$ (K) original HUTRAD [RD-2]	Approximate change of front-end loss (dB)
18.7 H	0.39	0.28	+1.5
18.7 V	0.47	0.33	+1.6
10.65 H	0.48	0.57	-0.9
10.65 V	0.32	0.55	-2.9
6.8 H	0.30	0.19	+2.4
6.8 V	0.35	0.22	+2.3

Considering the results presented in Table 2, the original design goal for radiometric resolution ( $< 1$  K, [RD-2]) is still fulfilled. However, some differences are evident between the current and the older radiometric resolutions. These differences are deemed to be mostly because of differences in front-end attenuations. Another minor reason is the different receiver temperatures in HUTRAD 2.0 measurements (33°C) conducted in laboratory and in the original HUTRAD measurements (15-20°C) conducted outside during a field campaign. Assuming that the receiver noise is linearly dependent on the physical temperature, the difference in receiver temperatures explains approx. 0.2 dB increase in the HUTRAD 2.0 measurement. The differences in front-end losses are generated by the following differences of the receiver front-end configurations:

- Mechanical switches with 0.2 dB loss were included in the original 6.8 GHz and 10.65 GHz configurations between antennas and Dicke switches. These switches were removed some years after measurements reported in [RD-2].
- Original HUTRAD included parabolic reflector antennas with dual polarization output while HUTRAD 2.0 has lens-loaded horn antennas with Orthomode Transducer (OMT).
- The Dicke switches for 6.8 GHz and 18.7 GHz were changed for HUTRAD 2.0. The losses of the new 18.7 GHz switches are approximately the same as in the original receiver. The losses of the original 6.8 GHz switches were exceptionally low, and comparable switches were not any more available. Therefore, the losses of the new switches are significantly higher (approx. 0.5 dB) than the original ones.
- The waveguide section of the 18.7 GHz receiver is somewhat longer in HUTRAD 2.0 than in the original system. Also, the RF cable harness of 6.8 GHz and 18.7 GHz receivers have a different configuration.
- Performance degradation of components over the years.

## 4.2 Temperature stability

### 4.2.1 Stability Test in Cold Test Laboratory

To assess the performance of HUTRAD 2.0 in cold environmental conditions, the radiometers were tested in the cold test laboratory of Metropolia University of Applied Sciences (Vantaa, Finland). The test setup is shown in Figure 12. The receivers were located in the testing room of the cold temperature laboratory, whereas the CPU, UPS, and 24 V power supply were located in the control room with normal room temperature. Thus, the configuration resembled very well the conditions in the measurement aircraft. The cables between the CPU and the receivers were routed through a small hole in the wall between the testing room and the control room. The receivers were placed into a physical configuration that resembled the aircraft configuration although without the aircraft rack and the downwards tilt associated to that.



*Figure 12. Cold environment test to study the internal thermal stability of the receivers.*

The cooling system of the testing room produced a light wind during the entire test; this was a constant and nearly random-directed, light but very noticeable air movement. The air movement accelerated the heat flow between the surface of the units and the air in the room, similarly to the conditions expected in aircraft use. The receivers were placed on a wooden pallet (Figure 12). The test proceeded as follows:

1. In the first part of the test, the set-point of receivers' internal temperature was set to +10°C. The room temperature was set to -20°C and the receivers were able to hold their internal temperature, settling near +9.7°C. The Peltier elements were working at 35-46 % of their maximum power. The measured temperatures (room and receivers' internal) are shown in Figure 13 and Figure 14, respectively.
2. In the second part of the test, the room was cooled to -30°C, which was achieved at about 14:36 o'clock. The set-point for receivers' internal temperature was lowered to 0°C, because it was clear that the +10°C inside temperature could not be maintained. The room temperature and the receivers' internal temperatures are shown in Figure 15 and Figure 16, respectively, from about 15:15 o'clock onwards. It can be seen that the temperature stabilization system is on its limits and especially the 10.65 GHz system cannot maintain the 0°C temperature. The warming up of the room was gradually started at around 16:00 o'clock.

Based on these results, updates of the radiometers were planned and implemented (as discussed in the next Section) to improve the thermal stability of the receivers in extreme cold temperatures. This need for update was clear especially for the 10.65 GHz unit, but also for the two other ones.

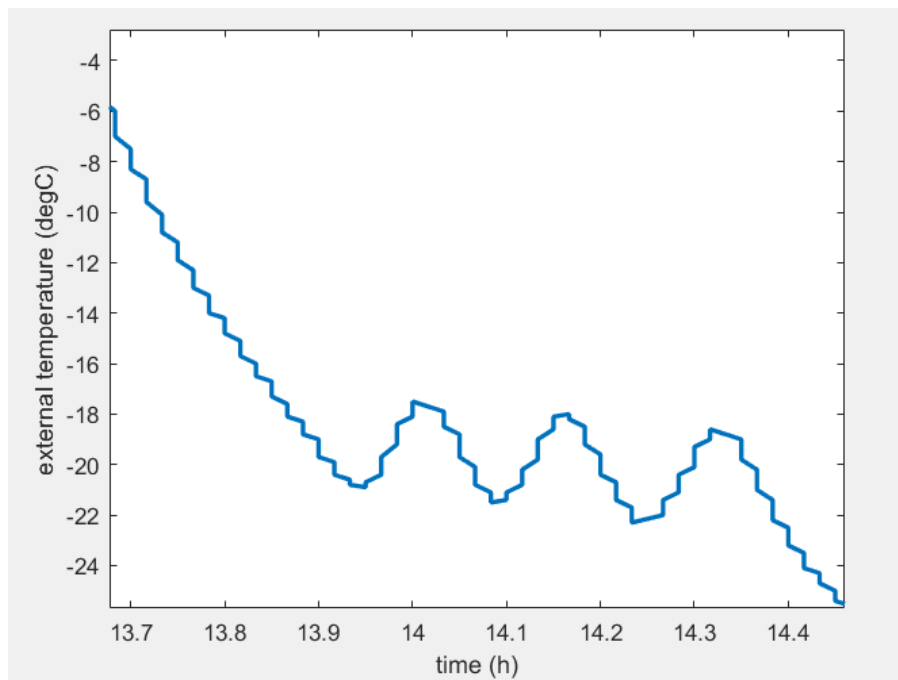


*Figure 13. Test room temperature during part 1 of the cold environment test. Initially, the set point of the room temperature was set to -20°C. The set point was reached at around 13:55 o'clock, although some oscillation of the room temperature is present. At about 14:20 o'clock, the set point was set to -30°C.*

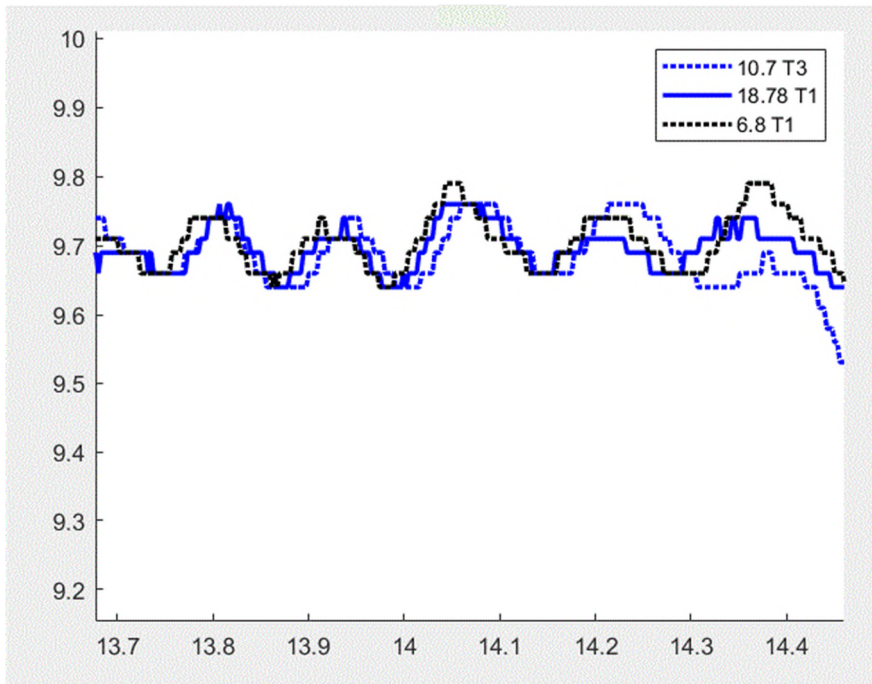


Figure 14. The internal temperature of the receivers (air sensor) during part 1 of the cold environment test.

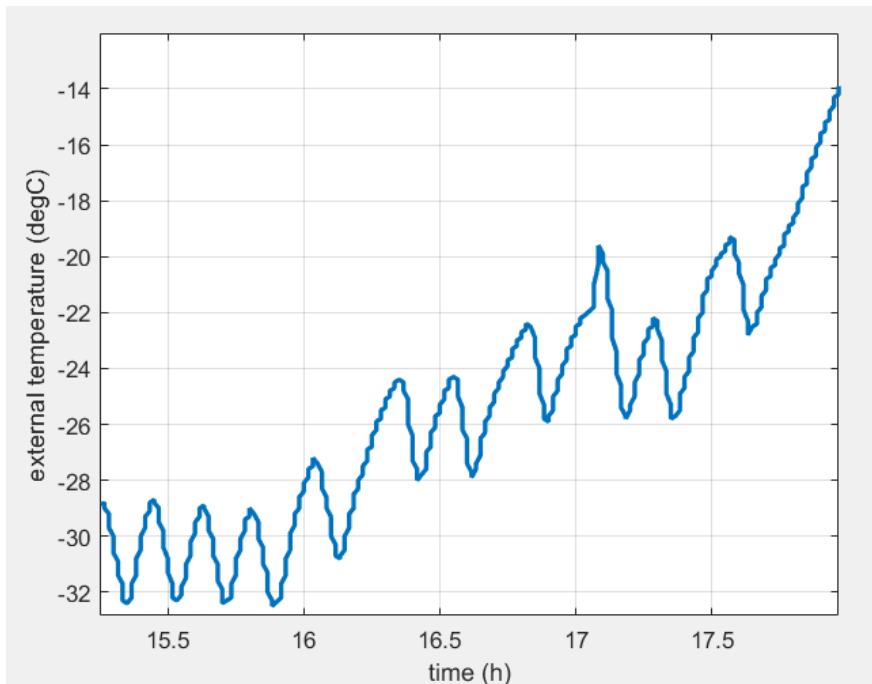


Figure 15. Room temperature during part 2 of the cold environment test. The room temperature is initially near to -30°C. At 15:50 o'clock, a process to warm up the room was started; the room temperature was increased step by step. The temperature oscillation is due to the imperfect features of the room's cooling and warming system.

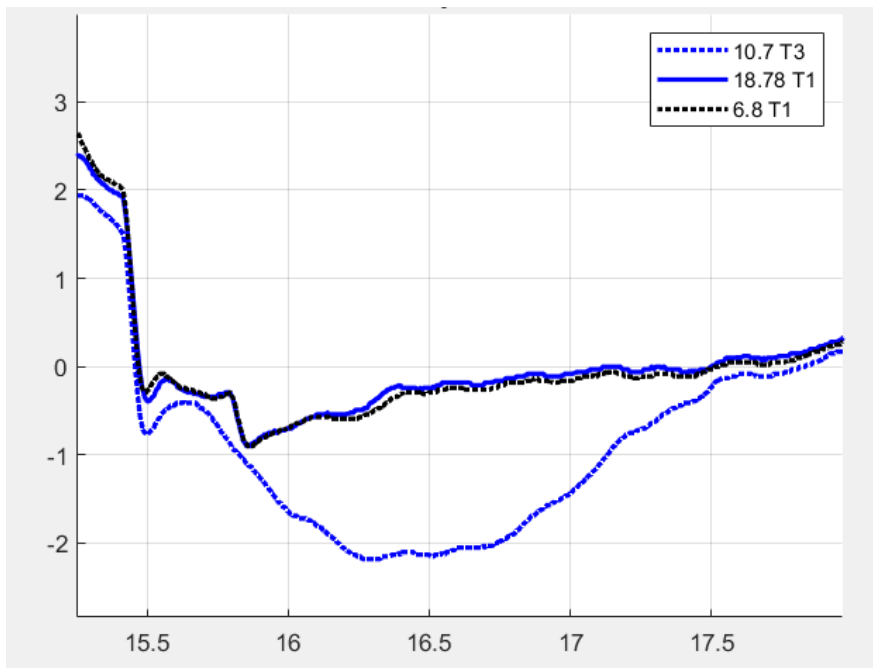


Figure 16. Receivers' internal temperature (air sensor) during part 2 of the cold environment test, where the internal set point was set to 0°C. By 16:00 o'clock the 18.7 GHz and 6.8 GHz units reached -0.8°C internal temperature (Peltier power about 30 %), but the 10.7 GHz unit did not stabilize equally well.

#### 4.2.2 Stability Tests in Room Temperature

As a result of the test results reported above in Section 4.2.1, HUTRAS 2.0 system's performance to maintain the thermal stability of the receivers was improved by two means: 1) thermal insulation of the receiver enclosures was further improved and 2) additional internal heating resistor was implemented in each receiver. Each resistor produces 7.5 W heating power to assist the heating by the Peltier elements. The heating resistor of each receiver can be switched on and off using a small toggle switch, which is mounted outside the receiver enclosure (in the rear panel). The resistor value is 30 Ω, and it is installed to dissipate heat primarily to the air rather than to the metal tray.

After the resistors were installed, the stabilization test was repeated in normal laboratory conditions (normal room temperature), with the heating resistors continuously turned on. Below, Figure 17 - Figure 21 show time series of the receivers' temperatures during this test. Internal receiver temperature of +45°C (i.e.,  $\Delta \approx 23^\circ\text{C}$ ), reached by the end of the test, stabilized rather well (the Peltier elements operated at, nominally, 42-66 % power depending on the unit, as shown in Figure 21). The temperature sensors placed in the airflow within the receivers show that a stabilization period of approx. 1.5 hour would be sufficiently long to reach thermal stability (see Figure 17 and Figure 18). However, the sensors mounted on the metal trays show that longer period, approx. 2 hours would be needed to reach a stabilization level of about 0.1°C (see Figure 19 and Figure 20). Turning on the internal heating resistors increases the total current consumption of the system by ~1.5 A. However, this has no impact on the brightness temperature measurement data in any of the receivers.

As shown by Figure 17, the 18.7 GHz unit exhibits the greatest rate of temperature increase. It also had the largest Peltier power margin ( $P_{\text{peltier}} = 42\%$  with set point temperature of  $+45^{\circ}\text{C}$  in the stable state). This is partly due to higher power dissipation of the 18.7 GHz receiver compared to the others; it is a superheterodyne receiver with two Gunn oscillators while the other receivers are of direct detection type. The 10.65 GHz unit is the slowest to warm up, and also its Peltier margin is the smallest ( $P_{\text{peltier}} = 66\%$ ).

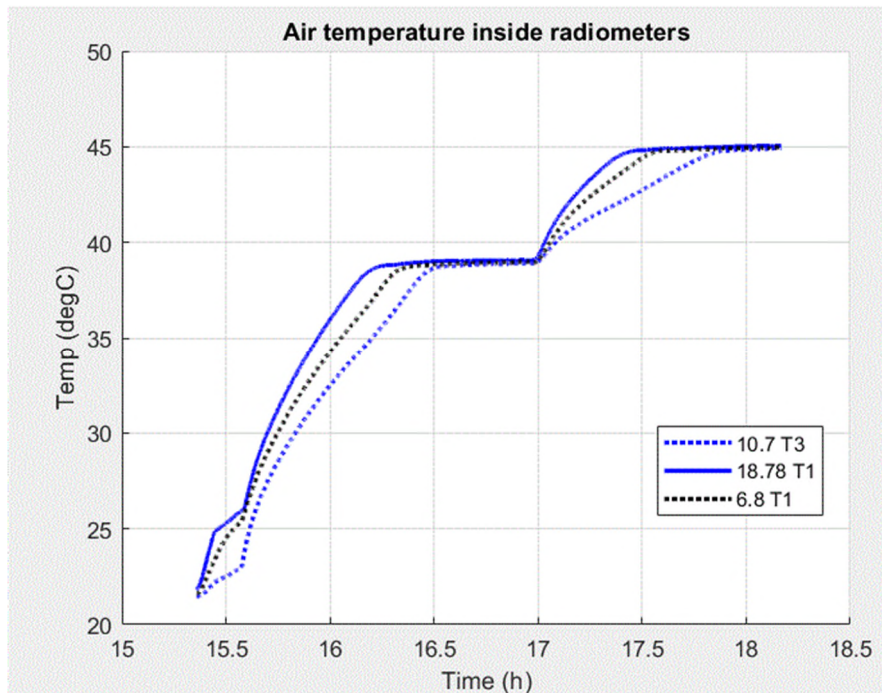


Figure 17. Temperature of the air sensors of the receivers' stability testing in a normal room temperature. Air sensors of the 10.7 GHz, 18.7 GHz and 6.8 GHz receivers were T3, T1, and T1, respectively. The set-point temperatures were  $+39^{\circ}\text{C}$  (first part of the test until 17:00 o'clock) and  $+45^{\circ}\text{C}$  (second part from 17:00 o'clock onwards).

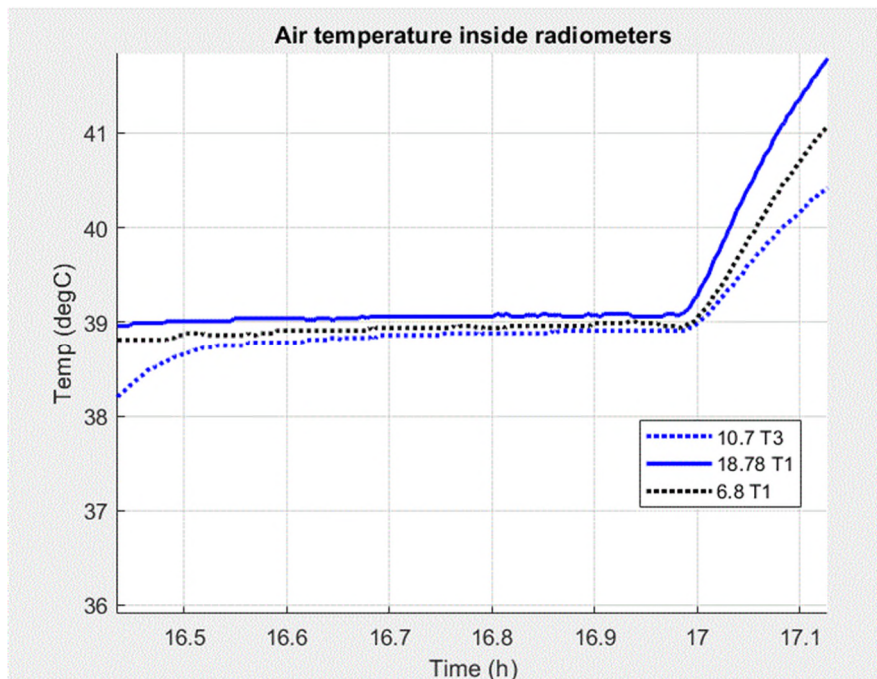


Figure 18. Zoomed-in version of the preceding figure (temperature of the air sensors of the receivers when testing in normal room temperature).

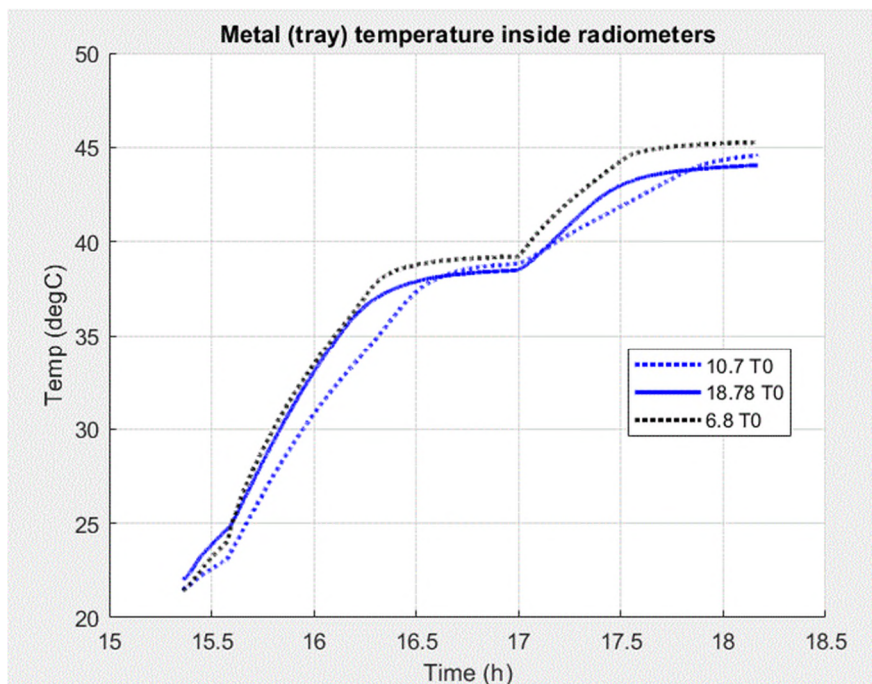


Figure 19. Temperature of the metal-tray-mounted sensors (numbered  $T_0$ ) of the receivers during testing in normal room temperature.

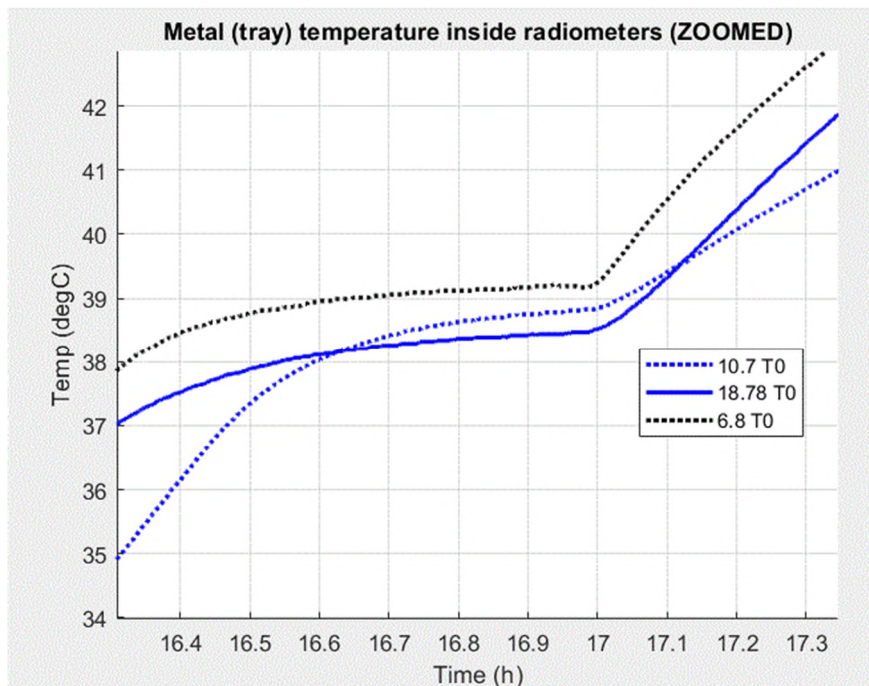


Figure 20. Zoomed-in version of the preceding figure (temperature of the metal tray-mounted sensors) of the receivers during testing in normal room temperature.

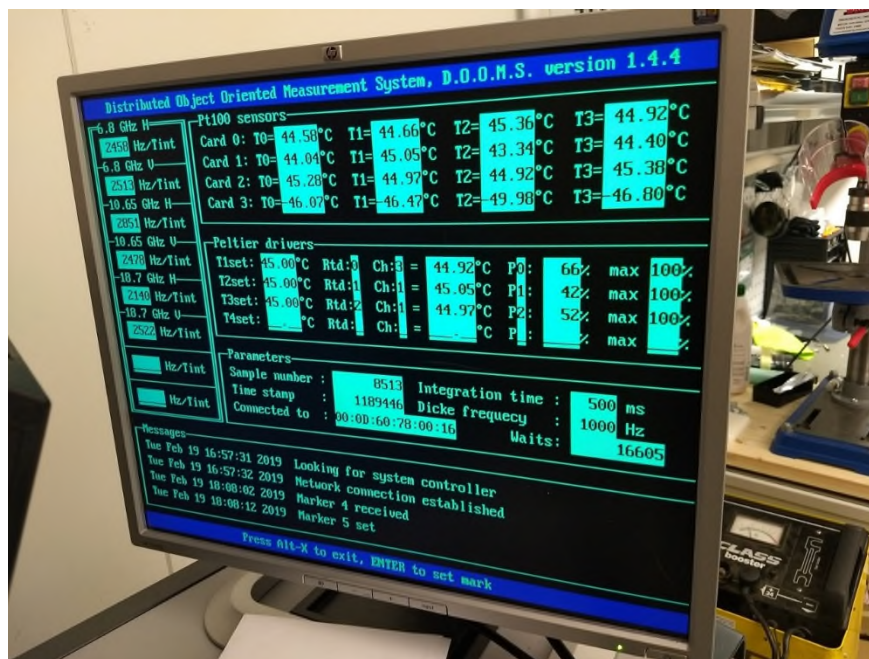


Figure 21. Monitor readings at the end of the test at normal room temperature. The order of the rows in the fields “Pt100 sensors” and “Peltier drivers” is 10.7 GHz (top), 18.7 GHz (middle), and 6.8 GHz (bottom).

## 5. Conclusions

In the work reported in this document, the 6.8 GHz, 10.65, and 18.7 GHz channels of a legacy HUTRAD radiometer system were repaired and refurbished into HUTRAD 2.0 system. As tested, HUTRAD 2.0 works as expected and sufficiently well to perform radiometer measurement with high quality. There are some differences in the radiometric resolution (with respect to results obtained in 1995), mostly and most probably due to the modifications of antennas and front-end components. As tested, the system is ready to be installed on Twin Otter aircraft and to be used for airborne measurements in the Arctic.

## **Appendix 2: Campaign Implementation Plan**

**CIMREx**

**CIMR Airborne Arctic campaign**

**Deliverable 2**

# Campaign Implementation Plan

---

**ESTEC Contract No:** 4000125503/18/NL/FF/gp

Issue / Revision: 1 / 0

Date: 15 January 2019

Prepared by:

Juha LEMMETYINEN  
Finnish Meteorological Institute, Finland

Gunnar SPREEN  
University of Bremen, Germany

René FORSBERG  
National Space Institute, Denmark

With comments from:

Rasmus TONBOE  
Danish Meteorological Institute

---

*This page is intentionally left blank.*

## Document change log

Issue/ Revision	Date	Observations
1.0	15 January 2019	First issue

*This page is intentionally left blank.*

## Table of Contents

<b>1</b>	<b>INTRODUCTION</b>	<b>2</b>
<b>2</b>	<b>INSTRUMENTATION</b>	<b>3</b>
2.1	HUTRAD	3
2.1.1	RADIOMETRIC CALIBRATION	4
2.1.2	GEOREFERENCING	5
2.2	GPS AND ATTITUDE SENSOR	7
2.3	OPTICAL AND INFRARED CAMERA	7
2.4	LOGISTICS AND INSTALLATION	8
<b>3</b>	<b>TEST SITE</b>	<b>10</b>
<b>4</b>	<b>DATA ACQUISITION PLAN</b>	<b>11</b>
4.1	AIRBORNE OPERATIONS	11
4.1.1	TRANSFER FLIGHT	13
4.1.2	SCIENCE FLIGHTS	13
4.2	INSTRUMENT CALIBRATION	16
4.3	SCHEDULE	16
<b>5</b>	<b>DATA PRODUCTS</b>	<b>17</b>
5.1	HUTRAD L1 BRIGHTNESS TEMPERATURES	17
5.2	VIDEO CAMERA MATERIAL	17
<b>6</b>	<b>PERSONNEL</b>	<b>18</b>
<b>7</b>	<b>REFERENCES</b>	<b>18</b>

## 1 Introduction

This document provides the detailed plan of the Copernicus Imaging Microwave Radiometer (CIMR) Arctic Airborne campaign. It forms the second deliverable of the ESA project 4000125503/18/NL/FF/gp.

This document gives the details of the airborne experiment, including all aspects related to ground operations (installation of instruments, calibration, removal of instruments) and airborne data acquisitions. The document is structured as follows:

- Section 2: Instrumentation. This section gives details on the instruments applied in the campaign, i.e. the HUTRAD microwave radiometer, GPS and attitude detector, and other ancillary instruments, and describes plans for instrument logistics and installation/removal
- Section 3: Test sites. The section describes the intended test sites to be covered by airborne measurements
- Section 4: Data acquisition plan. this section describes the intended flight patterns, schedules, instrument operation and calibration
- Section 5: Data products. This section describes the data products to be generated, i.e. the HUTRAD L1 calibrated and georeferenced brightness temperatures

## 2 Instrumentation

### 2.1 HUTRAD

The original Helsinki University of Technology Radiometer (HUTRAD) was developed in the 1990's at the Laboratory of Space Technology of the Helsinki University of Technology (Hallikainen et al., 1996). The original system consisted of dual-polarized radiometer receivers at six frequencies (6.8, 10.7, 18.7, 23.8, 36.5, and 94 GHz). The complement of frequencies was designed to correspond to those available on existing and planned satellite microwave sensors, including the Special Sensor Microwave Imager (SSM/I) and the proposed ESA Multifrequency Imaging Microwave Radiometer (MIMR). The HUTRAD system is divided in two independent subsystems, the so-called high- and low frequency subsystems (HF and LF, respectively). The LF system was finalized in 1995 and used in the ESA European Multi-sensor Airborne Campaign (EMAC'95). The 36.5 GHz receiver of the HF subsystem was later designed to be fully polarimetric (Lahtinen et al., 2003). In previous airborne operations (e.g. Colliander et al., 2006; Lemmetyinen et al., 2009) the radiometers were installed in a backward-profiling configuration of a SC-7 Skyvan research aircraft, with a nominal incidence angle of  $\sim 50^\circ$  (Figure NN).

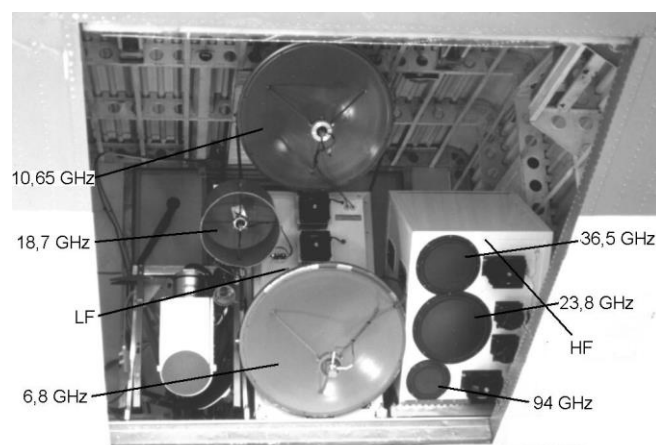


**Figure 1:** The original HUTRAD system installed in the rear cargo bay of an SC-7 Skyvan aircraft. The low-frequency (LF) system has been refurbished for use in CIMREx.

In CIMREx WP100, LF-system containing frequencies 6.8, 10.65 and 18.7 GHz was refurbished for installation in a de Havilland DHC-6 Twin Otter aircraft. The smaller aircraft necessitated redesign of the receiver housings and mechanical interfaces, as well as acquisition of new antennas which were integrated into the receiver housings (the original antennas were Cassegrain-type reflector antennas). On the Twin Otter, the receivers are installed in a side-looking configuration.

The characteristics of three refurbished receivers refurbished for CIMREx are listed Table 1 (NOTE: the radiometric parameters correspond to the original HUTRAD design)

**Table 1:** Main characteristics of HUTRAD system.

Frequency (GHz)	6.825		10.65		18.7	
Polarization	V	H	V	H	V	H
Bandwidth (MHz)	310	310	120	120	750	720
Sensitivity <sup>1)</sup> (K)	0.11	0.09	0.22	0.24	0.1	0.09
$\theta_{3dB}$ (°) <sup>2)</sup>	14.7	11.4	9.2	6.7	5.2	4.1
Footprint dimensions <sup>3)</sup> (L x W) (km)	0.7 x 0.4		0.4 x 0.2		0.2 x 0.1	

- 1) Theoretical radiometric resolution for Dicke-type radiometer with 300 K antenna temperature and 0.5 s integration time
- 2) Simulated beamwidth with refurbished antennas
- 3) Dimensions of footprint ellipse on level ground for 1 km flight altitude

### 2.1.1 Radiometric calibration

The calibration of the HUTRAD system is performed using a two-point calibration. Absorptive material at ambient temperature is used to cover the entire aperture of antennas to create a ‘hot’ calibration target. The ‘cold target’ is achieved using similar material cooled to ~77 K using liquid nitrogen. In practice, metal containers with microwave absorbing material on the bottom surface have been applied – these are lifted in front of the radiometer antenna aperture and kept in place for sufficient time to achieve a reliable calibration measurement (in practice, calibration times of 30s to one minute have been applied). The physical temperature of the ‘hot’ target is measured using a precision thermometer, and assuming the absorber acts as a perfect blackbody, this gives directly the brightness temperature. Similarly, the ‘cold’ target is assumed to be at the boiling point temperature of liquid nitrogen (77 K under nominal pressure conditions).



**Figure 2:** Calibration of HUTRAD receiver using a calibration target (metal container containing absorptive material) in front of the antenna aperture. Two targets are used; one is kept at ambient temperature, the other is cooled with liquid nitrogen prior to calibration.

The output of HUTRAD is expressed as integrated detector voltages over the defined integration time. Assuming a linear behaviour of the system, the detector voltage  $V_{out}$  is assumed to depend on the receiver total gain  $G$ , the measured antenna (brightness) temperature  $T_A$  and detector offset  $U$  so that

$$V_{out} = G \cdot T_A + U \tag{1}$$

By measuring two differing antenna temperatures, the parameters  $G$  and  $U$  can be solved, and used to convert recorded voltages to antenna temperatures.

The HUTRAD system does not include a possibility for internal receiver calibration; therefore, emphasis has been placed on the thermal stabilization of the receivers in order to minimize receiver gain and noise temperature variations in between calibrations. In order to verify the stability of the instrument, calibrations have been performed optimally before and after a science flight. One to three calibration rounds (ambient target / cold target) have been performed per receiver to mitigate for possible errors in the manual handling of the calibration targets. In previous studies (e.g. Lemmetyinen et al., 2009; Lemmetyinen et al., 2015) the absolute accuracy, estimated from pre- and post flight calibrations, was estimated to be better than 2 K for the low frequency systems.

### 2.1.2 Georeferencing

The size and location ‘footprint’ of the HUTRAD instrument on the ground surface is determined by the antenna beamwidth (estimated by the half-power beamwidth  $\theta_{3dB}$ ), altitude from ground level  $h_0$ , incidence angle  $\theta_a$ , the aircraft attitude (yaw-pitch-roll) and location (**Figure 3**).

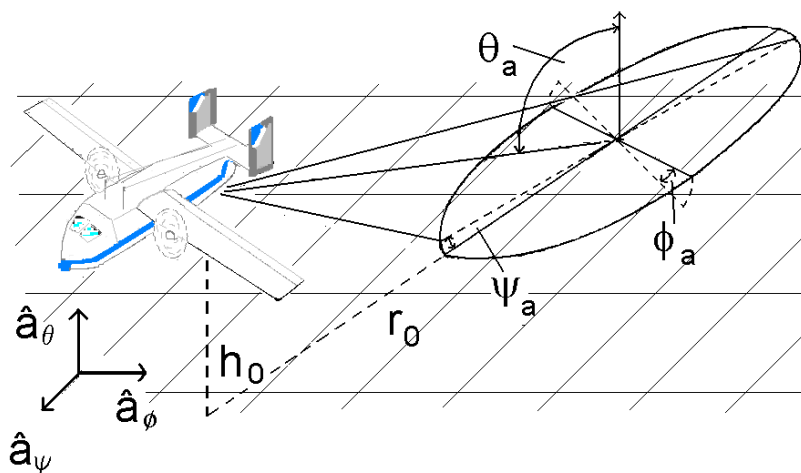


**Figure 3:** The geometry of the field of view of the HUTRAD instrument. Note that the setup on the de Havilland DHC-6 Twin Otter is side-looking.

Assuming a flat surface target, the footprint size in the parallel direction (major axis of footprint ellipse for a back-looking instrument) is given by

$$a = \frac{a_2 - a_1}{2} \quad (2)$$

Where

$$a_1 = h_0 \cdot \tan(\theta_a - \theta_{3dB}/2); a_2 = h_0 \cdot \tan(\theta_a + \theta_{3dB}/2); \quad (3)$$

The size of the footprint in the perpendicular direction (semi-major axis of ellipse) is

$$b = \sqrt{aR \cdot \tan(\theta_{3dB}/2)} \quad (4)$$

Where R is the direct distance to the footprint centrepoint given by

$$R = h_0 \cdot \cos(\theta_a) \quad (5)$$

For a side-looking instrument, these are naturally vice-versa. Note that for calculation of the footprint size of the refurbished HUTRAD system, the differing beamwidth in the horizontal and vertical plane should be accounted for (Table 1.). Furthermore, although the above equations give an estimate of the area where most of the microwave energy observed by the radiometer originates from, a more accurate estimate can be obtained by projecting the true beam pattern of the antennas on the ground plane.

In the above equations, the attitude of the aircraft determines the true incidence angle  $\theta_a$ . The attitude information is also used to calculate the orientation of the footprint ellipse, including deviation from the aircraft yaw ( $\psi_a$ ) and deviation of antenna beam ellipse from the level ground plane ( $\phi_a$ ).

A preliminary desing of the HUTRAD installation in the rear cargo hold of the Twin Otter aircraft is presented in **Figure 4**.

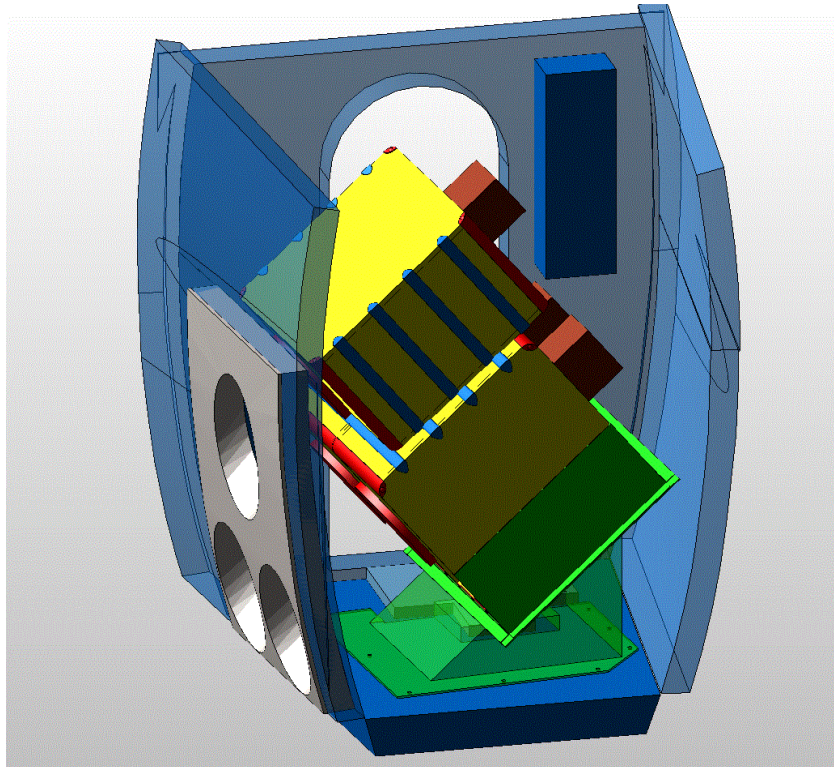


**Figure 4:** Installation of refurbished HUTRAD receivers in rear cargo hold of the Twin Otter aircraft. Image courtesy of Harp Technologies Ltd.

## 2.2 GPS and attitude sensor

Two precise geodetic GPS receivers (Javad type) will be providing the basic navigation for the aircraft. Using precise orbits and the IGS GNSS global reference network, postprocessed positions will be accurate to 5 cm. For aircraft attitude, roll, pitch and heading at  $0.01^\circ$  accuracy are measured using a high-end iMAR-RQH inertial survey system, with backup from an OXTS MEMs-based IMU. Both IMU will be supplied with precise GPS signals for UTC timing, and driving the embedded navigation and attitude Kalman filters. The iMAR-RQH system will also be used to test gravity measurement capability, a novel feature of this high end system, which could be a spin-off from the flights (numerous gravity flight campaigns have earlier been conducted in the region).

## 2.3 Optical and infrared camera

The optical sensor for the CIMREx will be a GoPro camera, with backup by a IQeye 703 digital camera (2048x1536 pixels) All cameras will be mounted in the nadir-looking cargo bay of the Twin-Otter aircraft, just below the HUTRAD instrument.

A thermographic Infratec VarioCAM HDx head 600 camera (Figure 5) will be installed in the bay under the HUTRAD radiometer system. The VarioCAM HDx 600 is based on an uncooled microbolometer FPA detector with  $640 \times 480$  IR pixels. It has a wide temperature measuring range that makes it suitable for universal measuring and monitoring tasks, including aerial thermography. It has an industrial-grade lightmetal housing (IP67), which makes operation possible in harsh environments. The camera is powered either by 12 to 24V

DC or by an 230V AC adapter. Data is recorded by an industrial mini-PC ICS POC-320. The camera can be remotely operated by a notebook connected by Ethernet (preferred) or WiFi.



**Figure 5:** Infratec VarioCAM HDx head 600 infrared camera.

Spectral range	(7.5 ... 14) $\mu\text{m}$	
Detector	Uncooled microbolometer focal-plane array	
Detector format (IR pixels)	(640 $\times$ 480)	
Temperature measuring range	(-40 ... 600) $^{\circ}\text{C}$	
Measurement accuracy	$\pm 2$ $^{\circ}\text{C}$ or $\pm 2\%$	
Temperature resolution (@ 30 $^{\circ}\text{C}$ )	Up to 0.03 K	
Frame rate	Full-frame: 30 Hz (640 $\times$ 480), sub-frame: 60 Hz (384 $\times$ 288)	
Lens		<i>Alternative:</i>
Focal length	10 mm	20 mm
Field of view	57.1 $^{\circ}$ $\times$ 44.4 $^{\circ}$	30.4 $^{\circ}$ $\times$ 23.1 $^{\circ}$
Focus	Motor-driven, automatic or manual, accurately adjustable	
Dynamic range	16 bit	
Power supply	AC adapter, or (12 ... 24) V DC, or PoE	
Storage and operation temperature	(-40 ... 70) $^{\circ}\text{C}$ , (-25 ... 55) $^{\circ}\text{C}$	
Protection degree	IP67, IEC 60529	
Impact strength, vibration resistance in operation	25 G (IEC 68 - 2 - 29), 2 G (IEC 68 - 2 - 6)	
Dimensions, weight	(221 $\times$ 90 $\times$ 94) mm, 1.15 kg	
Further functions	Camera internal emissivity correction, shutter free operation	

## 2.4 Logistics and installation

The installation of the HUTRAD system is planned on the Nordlandair Twin Otter aircraft. The installation of HUTRAD will take place in Akureyri, Iceland. All equipment will be transferred by air freight to Iceland for installation. The installation and a test flight is to be done in the period 22-24 FEB in the Nordlandair hangar. DU Space will provide 19" racks for the HUTRAD equipment and navigation/camera equipment, and general 12/24/220 V power from the aircraft. The HUTRAD itself will be powered directly from the 28V aircraft power. All cargo should be sent airfreight to:

Norlandair  
Akureyri Airport  
IS-600 Akureyri, Iceland  
Att. Arnar Fridriksson, [arnar@norlandair.is](mailto:arnar@norlandair.is), tel. +354 615-3963

Liquid nitrogen (LN2) required for calibrations will be available at airports in Akureyri (via AGA) and Longyearbyen (via Pole Position Logistics Ltd.). An amount of 30 L will be ordered to Akureyri and 180 L to Longyearbyen. This should allow for the required number of calibrations, taking also into account dissipation of the LN2.

Note: *Pole Position logistics requires approximately **10 days of advanced notice** for LN2 delivery in Longyearbyen.*

The permissions for flights and research in Svalbard and operations in Greenland will be handled by DTU Space in cooperation with Norlandair. Permissions include the following:

- Norwegian CAA – permission to operate foreign aircraft in Norwegian Air Space
- Research in Svalbard – online registration, pre-approval of research
- Sysselmanden in Svalbard – research and flight permission
- Greenland Government – mandatory information on governmental flights (ESA task)
- Tele Greenland – landing and overnight at Danmarkshavn
- Arctic Command – Permission for alternate landings at Station Nord or Daneborg
- Danish Police – dispensation for entering Greenland bases from Svalbard (non-Schengen area)

### 3 Test site

The Arctic Ocean north of Svalbard forms the main area for data collection. The precise location of science flights will finally be determined by ice conditions (location of the marginal ice zone, MIZ). Based on ice climatologies it is anticipated, however, that suitable ice conditions are to be found within flight distances of Svalbard. **Figure 6** depicts the ice extent over the polar Arctic during the historical sea ice minima in February 2018. Also the 30-year median extent of sea ice (1981-2010) is depicted. While the median ice edge reaches to cover the Svalbard archipelago almost entirely, conditions in February 2018 saw large areas of open water immediately to the North and North-West of the islands. It is probable that conditions in February 2019 will not deviate significantly from these conditions, and that suitable ice can be found within the range of the Twin Otter aircraft (~1400 km). This is supported by the sea ice frequency of occurrence climatology map in Figure 7. Within 500 km distance to Longyearbyen sea ice always could be found in February for the 30 years 1987 to 2016 (white areas) and there is a good chance to find sea ice even closer (blue shaded areas). It should be noted that also measurements of open water are desirable to provide a reference to sea ice.

Instrument installation will take place in Akyreyri, Iceland. There is an opportunity for data collection during the transfer flight from Iceland to Svalbard along the Greenland coast, capturing diverse ice conditions.

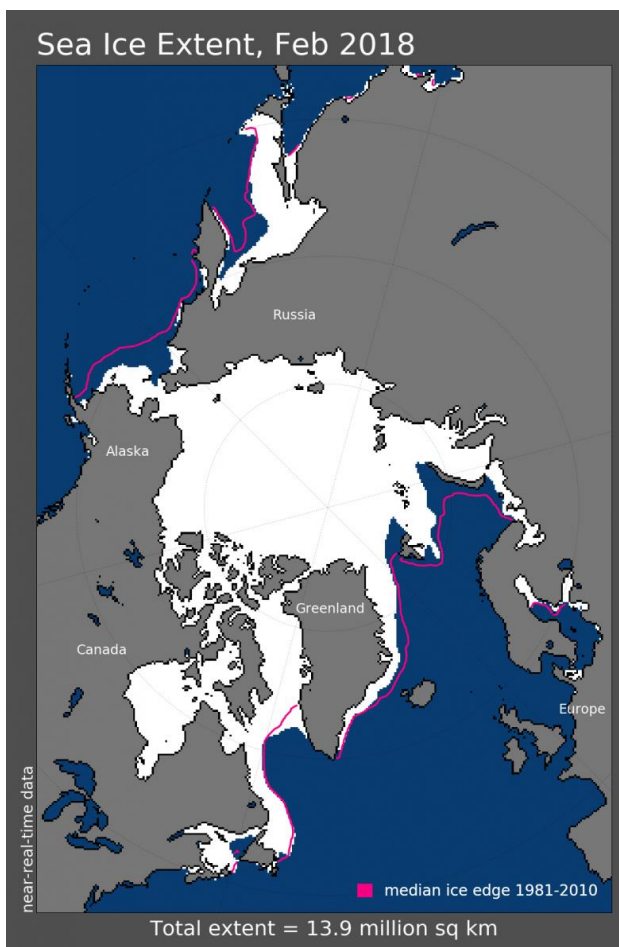


**Figure 6:** Sea ice extent over polar Arctic in February 2018. Median ice edge during 1981-2010 indicated by red line. Courtesy of NSIDC/Univ. Colorado. Intended area of science data collection indicated by blue box.

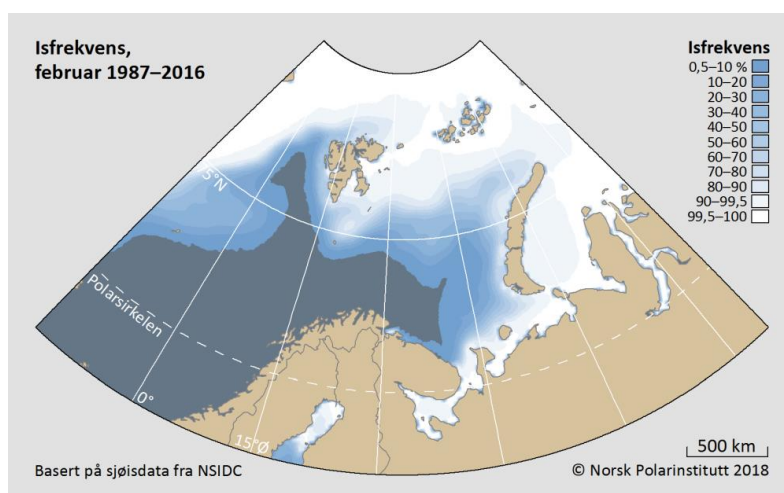


**Figure 7:** Likelihood of sea ice occurrence in February around Svalbard during the 30-year time period 1987 to 2016. An ice frequency of 100% (white) means that sea ice (> 15% ice concentration) prevailed at that location during all 30 years and 0% (blue) means during none of the years. Map from <http://www.npolar.no/en/facts/the-marginal-ice-zone.html>, more information about the data can be found here: <https://doi.org/10.21334/npolar.2014.a89b2682>

## 4 Data acquisition Plan

### 4.1 Airborne operations

The airborne operations are planned to capture gradients in SST, different sea ice floe size distributions and concentrations. Scientific data will be collected in two phases: during the transfer flight from Iceland to Svalbard as well as during dedicated science flights from Longyearbyen. **Figure 8** and Table 2 depict the preliminary CIMREx flight plan (submitted for flight permits) including the transfer from Akureyri (AEY) via Danmarkshavn (DMH) weather station to Longyearbyen (LYR), and flight operations from Longyearbyen. A refueling stop at Constable Point airport (CNP) is required during the transfer flight in Greenland.

The flight programme involve several transects over the multiyear to marginal ice zone and open water in Greenland, as well as two primary flight tracks in Svalbard, to the north (mix of FY and MY ice) and to the east (predominantly thinner FY ice).

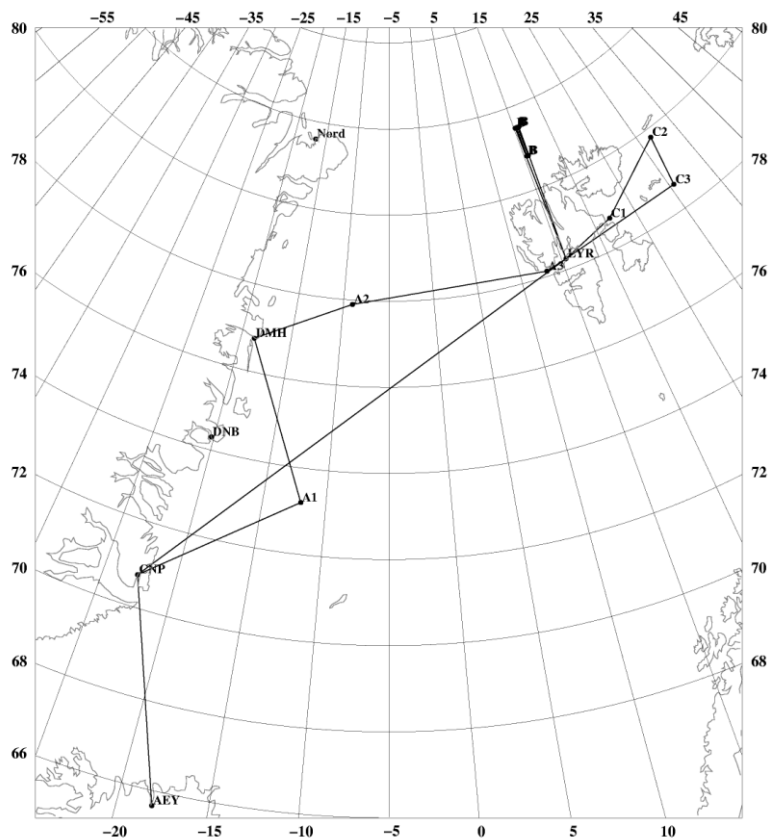


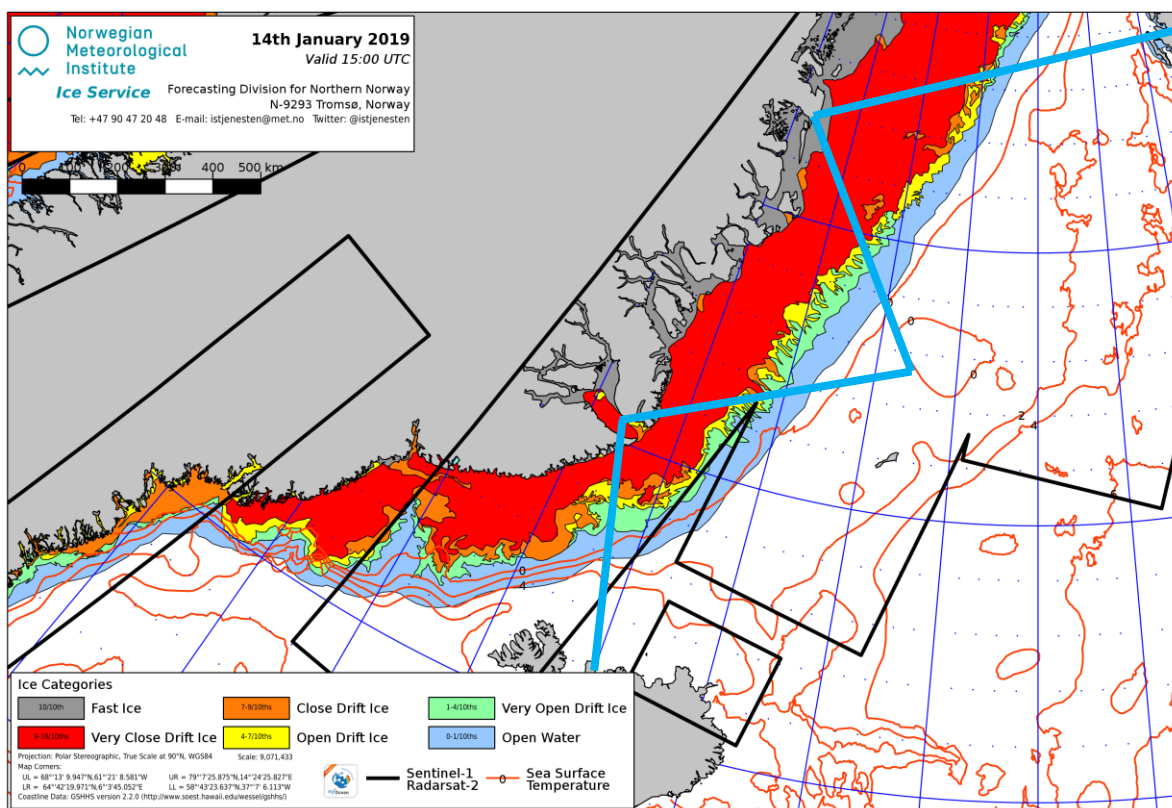
Figure 8: Preliminary CIMREx flight plan.

Table 2: tentative flight plan (Jan 9, 2019)

DATE	Day	AIRCRAFT OPS POF	Airborne time	LODGING
February 21	Thu	DTU + Finland pax to Iceland		Akureyri
21-23	Fri-Sun	Installation of instruments, test flight	<1 hr	-
25	Mon	Measurement/transit flights AEY-CNP-DMH	7 hr	Danmarkshavn
26	Tue	Local flight and transit to Svalbard	3+4 hr	Longyearbyen
27	Wed	Flight #1 north of Svalbard	5 hr	-
28	Thu	Flight #2 east of Svalbard	5 hr	-
March 1-3	Fri-Sun	Backup weather days, backup flights	?	-
2	Mon	Transit flight LYR-CNP (high level transit over open ocean), CNP-AEY	5+3 hr	Akureyri
3	Tue	Unmount equipment	-	-
4	Wed	DTU + Finland pax return	-	-

### 4.1.1 Transfer flight

The transfer flight from Akyreyri, Iceland, to Longyearbyen in Svalbard will provide an opportunity to observe sea ice off to the East coast of Greenland. A flight trajectory comprising of several crossings of the ice edge is planned (**Figure 9**), allowing to capture ice at different levels of concentration as well as open water with possible gradients in Sea Surface Temperature (SST).



**Figure 9:** Sea ice chart over Greenland coast, January 2019. Svalbard visible in top right. A preliminary flight line indicated in blue, allowing multiple crossings over ice edge, capturing diverse ice types as well as open water with sea surface temperature gradients.

### 4.1.2 Science flights

Several science flights are planned near the Svalbard archipelago. While the final test sites will be defined closer to the campaign, already the ice situation in January 2019 allows to plan for tentative test areas which will represent open water as well as drift ice of various concentrations (**Figure 10**). The science flights will comprise of several transects crossing the marginal ice zone (MIZ) into the thicker pack ice. The precise location of these transects will be defined based on ice conditions in February-March 2019. The aim is to cover the transition from open water crossing the MIZ into the closed ice pack as often as possible under different ice conditions. If possible different ice regimes (young ice, first-year ice, multiyear ice, flat and deformed ice) will be targeted.

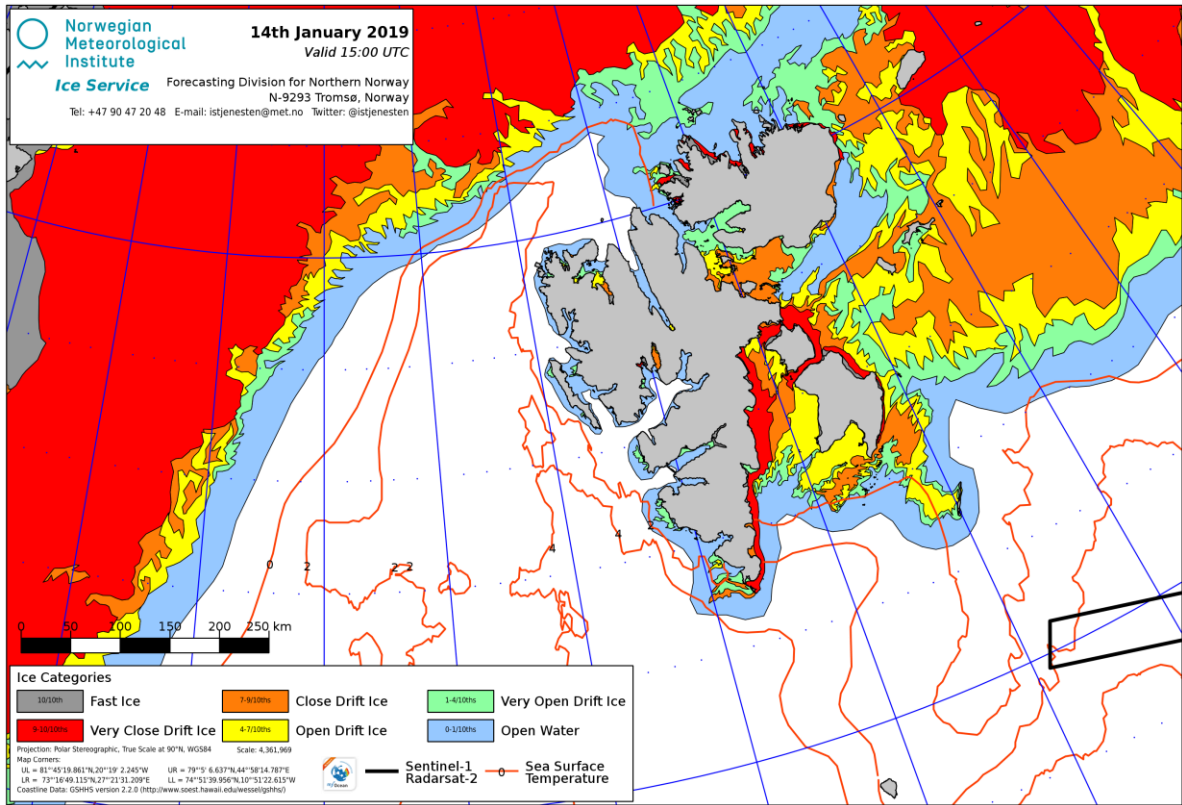


**Figure 10:** Sea ice chart Svalbard, January 2019. Possible test areas representing different ice conditions indicated in blue (a: open water; c-d: drift ice with varying concentrations)

**Figure 11** shows the estimated dimension (length x width) of HUTRAD footprints as a function of flight altitude, considering level flight and level ground (sea) surface. At an altitude of 300m, the estimated dimensions are less than 200 m on all frequencies.

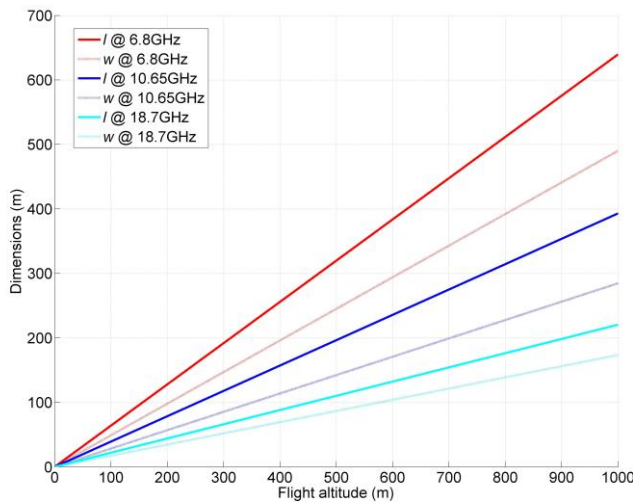


**Figure 11:** Estimated dimensions (l x w) of HUTRAD footprints for different frequencies as a function of flight altitude from sea level.

In tentatively two dedicated test areas (tentatively one off Danmarkshavna and one off Svalbard), a “mow-the-lawn” pattern will be flown with aim to cover the equivalent area of a CIMR footprint using several parallel transects, performed in an equivalent observation orientation to CIMR (**Figure 12**). Whether the whole area can be covered seamlessly will depend on available flight time at each test site, and the determined flight altitude, which determines the size of the HUTRAD footprint at ground level. Based on past experience, an approximately 20% overlap of footprints is advisable in order to achieve full coverage. However, seamless coverage may not be necessary to achieve the goals of the flights, in particular over relatively homogeneous targets such as open water or fast ice. The required number of transects may also be prohibitive (see **Table 3**).

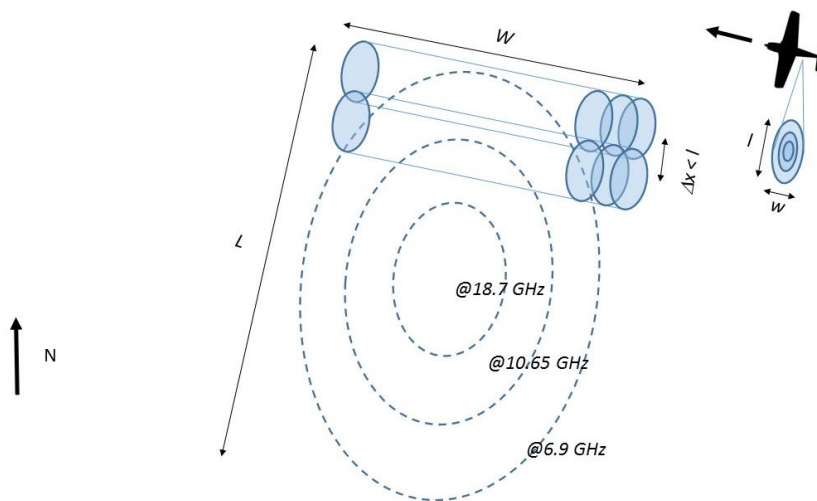


**Figure 12:** Schematic of flight transects over area equivalent of CIMR footprint.

**Table 3** shows the HUTRAD footprint size, and calculated number of parallel flight transects required to seamlessly cover each footprint of CIMR, using equivalent footprints of HUTRAD at flight altitudes of 300 and 1000 m. To ensure seamless cover, a 20 % overlap is anticipated.

**Table 3:** The HUTRAD 3 dB beamwidth and calculated footprint for each channel. Estimated number of parallel transects for seamless overlap of CIMR footprints.

Frequency (GHz)	6.8		10.65		18.7	
Polarization	V	H	V	H	V	H
$\theta_{3dB}$ (°)	14.7	11.4	9.2	6.7	5.2	4.1
HUTRAD Footprint dimensions (l x w)	690 x 390 m @1000 m 190 x 120 @300 m		400 x 220 m @1000 m 120 x 70 m @300 m		220 x 140 m @1000 m 70 x 40 m @300 m	
CIMR footprint dimensions (L x W)	19 x 11 km		13 x 7 km		6 x 4 km	
Number of required transects for seamless coverage (20 % overlap)	34 @1000 m		40 @1000 m		38 @1000 m	

## 4.2 Instrument calibration

Calibrations of HUTRAD using ‘hot’ and ‘cold’ calibration targets are planned, as default, before and after each science flight and before the transfer flight in Iceland. It is currently unclear if calibration can be arranged also after the transfer flight directly upon arrival in Svalbard. Full calibrations cannot be performed during refuelling in Greenland due to lack of liquid nitrogen.

When full calibration using ‘cold’ targets cooled by liquid nitrogen cannot be arranged, instrument stability will be verified by measuring the ‘hot’ target in ambient temperature. This allows to estimate absolute receiver bias close to the target temperature (e.g. 263 K at -10°C) which gives a reasonable estimate of bias for observations close to equivalent brightness temperatures.

Other flight instruments do not require on-site calibration.

## 4.3 Schedule

The planned schedule is depicted below, with instrument installation beginning in Akyreyri on March 21st. March 1-3 are reserved for weather/backup days for the two science flights.

**Table 4:** Campaign schedule.

	February 2019									March 2019							
	20	21	22	23	24	25	26	27	28	1	2	3	4	5	6	7	8
Travel																	
Installation and preparation																	
Transfer flights																	
Science flights																	
Backup days																	

## 5 Data Products

### 5.1 HUTRAD L1 brightness temperatures

The calibrated and georeferenced HUTRAD brightness temperatures are provided in csv-files. Each data sample contains the integrated observations collected during the defined integration time (default 0.5 seconds), calculated to brightness temperature using calibration parameters. In addition the measured internal temperatures of radiometer receivers are provided. Each data sample is provided with a timestamp, associated aircraft location (lat, lon, altitude), aircraft attitude (yaw, pitch, roll), the calculated footprint location (lat, lon) on the Earth surface as well as the footprint size (major and semi-major axis of resolution cell ellipse) and deviation of ellipse from ground plane and aircraft yaw direction.

### 5.2 Video camera material

The video and infrared camera material will be provided in standard video format

## 6 Personnel

The following personnel are planned to participate in the campaign.

**Table 5:** Personnel participating in campaign and assigned roles.

Person	Affiliation	Flight crew	Instrument operator	Ground support / Iceland	Ground support / Svalbard
(Pilot)	Nordlandair	x			
(co-pilot)	Nordlandair	x			
René Forsberg	DTU-Space		x		
Tim Jensen	DTU-Space			x	
Juha Lemmetyinen	FMI		x	x	x
Sampo Salo	HARP		x	x	x
Samuli Nyman	Aalto		x		x
Tânia Casal	ESA				x

## 7 References

- Colliander, A., J. Lahtinen, S. Tauriainen, J. Pihlflyckt, J. Lemmetyinen, and M. Hallikainen, 2007. Sensitivity of airborne 36.5-GHz polarimetric radiometer's wind-speed measurement to incidence angle. *IEEE Trans. Geosci. Remote Sens.*, 45(7): 2122-2129
- Hallikainen, M., M. Kemppinen, K. Rautiainen, J. Pihlflyckt, J. Lahtinen, T. Tirri, 1996. Airborne 14-channel microwave radiometer HUTRAD. *IEEE 1996 International Geoscience and Remote Sensing Symposium Proceedings*, pp. 2285-2287, Lincoln, USA, 1996.
- Lahtinen, J., J. Pihlflyckt, I. Mononen, S. J. Tauriainen, M. Kemppinen and M. T. Hallikainen, 2003. Fully Polarimetric Microwave Radiometer for Remote Sensing. *IEEE Trans Geosci. Remote Sens.*, 41(8), 1869-1878.
- Lemmetyinen J., C. Derksen, J. Pulliainen, W. Strapp, P. Toose, A. Walker, S. Tauriainen, J. Pihlflyckt, J-P. Kärnä, and M. Hallikainen, 2009. A comparison of airborne microwave brightness temperatures and snowpack properties across the boreal forests of Finland and western Canada. *IEEE Trans. Geosci. Remote Sens.*, 47(3): 965-978
- Lemmetyinen, J., Derksen, C., Toose, P., Proksch, M., Pulliainen, J., Kontu, A., Rautiainen, K., Seppänen, J., and Hallikainen, M., 2015. Simulating seasonally and spatially varying snow cover brightness temperature using HUT snow emission model and retrieval of a microwave effective grain size. *Remote Sens. Environ.*, 156, 71-95.
- Skourup, H., S. B. Simonsen, L. Sandberg Sørensen, A. Di Bella, R. Forsberg, S. M. Hvidegaard, and V. Helm: ESA CryoVEx/EU ICE-ARC 2016 Airborne field campaign with ASIRAS radar and laser scanner over Austfonna, Fram Strait and the Wandel Sea. DTU Space Technical Report, 2018.

## **Appendix 3: Data Acquisition Report**

**CIMREx**

**CIMR Airborne Arctic campaign**

**Deliverable 3**

# Data Acquisition Report

---

**ESTEC Contract No:** 4000125503/18/NL/FF/gp

Issue / Revision: 1 / 2

Date: 29 August 2019

Prepared by:

René FORSBERG and Andreas STOKHOLM  
National Space Institute, Denmark

Juha LEMMETYINEN  
Finnish Meteorological Institute, Finland

Gunnar SPREEN  
University of Bremen

Samuli NYMAN  
Aalto University, Finland

Sampo SALO  
Harp Technologies Ltd., Finland



DTU Space  
National Space Institute



*This page is intentionally left blank.*

## Document change log

Issue/ Revision	Date	Observations
1.0	10 April 2019	1 <sup>st</sup> internal draft
1.1	1 July 2019	Internal draft
1.2	29 August 2019	1 <sup>st</sup> issue

*This page is intentionally left blank.*

## Table of Contents

<b><u>1</u></b>	<b><u>INTRODUCTION</u></b>	<b><u>6</u></b>
<b><u>2</u></b>	<b><u>INSTRUMENTATION</u></b>	<b><u>7</u></b>
<b>2.1</b>	<b>HUTRAD2.0</b>	<b>7</b>
<b>2.2</b>	<b>GPS AND ATTITUDE SENSORS</b>	<b>8</b>
<b>2.3</b>	<b>OPTICAL AND INFRARED CAMERAS</b>	<b>9</b>
<b><u>3</u></b>	<b><u>FLIGHT OPERATIONS</u></b>	<b><u>11</u></b>
<b><u>4</u></b>	<b><u>DATA PRODUCTS</u></b>	<b><u>13</u></b>
<b>4.1</b>	<b>HUTRAD</b>	<b>13</b>
4.1.1	RAW DATA FILES	13
4.1.2	HUTRAD L1 BRIGHTNESS TEMPERATURES	13
4.1.3	HUTRAD CALIBRATION	15
<b>4.2</b>	<b>INFRARED CAMERA MATERIAL</b>	<b>17</b>
<b>4.3</b>	<b>VIDEO CAMERA MATERIAL</b>	<b>19</b>
<b><u>5</u></b>	<b><u>REFERENCES</u></b>	<b><u>22</u></b>

## 1 Introduction

This document provides a report of the data collected during the Copernicus Imaging Microwave Radiometer Arctic Airborne campaign (CIMREx). It forms the third deliverable of the ESA project 4000125503/18/NL/FF/gp.

CIMREx was designed to support the EU Copernicus High Priority Polar Candidate Mission, Copernicus Imaging Microwave Radiometer (CIMR), to sample the sea ice microwave emissions from various sea ice regimes around Svalbard and Greenland. The measurements were carried out with the newly refurbished Finnish HUTRAD 2.0 radiometer, measuring the brightness temperature from the sea ice at various frequencies (6.8, 10.65 and 18.7 GHz) at vertical and horizontal polarizations, providing basic information on the ability for high-resolution measurements of sea ice concentration and related snow/ice properties for the future CIMR satellite. Refurbishment of HUTRAD was performed as a part of the CIMREx activities by Harp Technologies Ltd. In addition to the side-looking HUTRAD passive microwave measurements, also infrared and visual imaging was carried out, along with precise aircraft navigation with geodetic GPS and inertial navigation units.

The CIMREx campaign took place between February 28-March 11, 2019. The first data were collected during initial transitions from Akureyri, Iceland, via Greenland, to the main campaign site at Svalbard. Three dedicated data collection flights were carried out around Svalbard on March 7 and 8.

This document gives the details of the airborne experiment, including aspects related to ground operations (mainly radiometer calibrations) and airborne data acquisitions. The document is structured as follows:

- Section 2: Instrumentation. This section gives details on the instruments applied in the campaign, i.e. the HUTRAD2.0 microwave radiometer, the infrared camera, and other ancillary instruments
- Section 3: Data collection
- Section 4: Data products. This section describes the generated data products, including description of methods used for calibration.

## 2 Instrumentation

### 2.1 HUTRAD2.0

The HUTRAD2.0 instrument (called HUTRAD hereafter) was refurbished in Task 1 of CIMREx. For the campaign, the refurbished system with receivers at 6.8, 10.54 and 18.7 GHz was installed in the cargo compartment of a de Havilland DHC-6 Twin Otter aircraft, with radiometer aperture facing outward from the left side carbo door. The nominal incidence angle at level flight was  $50^\circ$  from nadir. The installation, as well as on-ground performance verification of the system, was performed in the premises of Norlandair in Akureyri, Iceland (**Figure 1**).



**Figure 1:** Ground performance check of the HUTRAD prior to installation (left). HUTRAD installed in the left cargo door of the Norlandair de Havilland DHC-6 Twin Otter (right).

The characteristics of three HUTRAD receivers refurbished for CIMREx are listed Table 1 (NOTE: the radiometric parameters correspond to the original HUTRAD design).

**Table 1:** Main characteristics of the refurbished HUTRAD2.0 system.

Frequency (GHz)	6.825		10.65		18.7	
Polarization	V	H	V	H	V	H
Bandwidth (MHz)	310	310	120	120	750	720
Sensitivity <sup>1)</sup> (K)	0.11	0.09	0.22	0.24	0.1	0.09
$\theta_{3\text{dB}}$ (deg) <sup>2)</sup>	14.8	11.2	9.1	6.6	5.2	3.9
$\theta_{9\text{dB}}$ (deg) <sup>2)</sup>	25.0	18.5	15.1	10.8	8.6	6.4

1) Theoretical radiometric resolution for Dicke-type radiometer with 300 K antenna temperature and 0.5 s integration time

2) Simulated beamwidth with refurbished antennas

## 2.2 GPS and attitude sensors

The CIMREx campaign GPS navigation data was logged both in real-time on the navigation PC (used by the pilots for the precise mow-the-lawn flights), as well as by two Javad Delta geodetic GNSS receivers connected to front and aft GPS antennas. The Javad receivers were processed post-mission by *ppp* techniques using IGS precise orbits to produce 3D accuracies on the ~10 cm level. Heights above the ellipsoid have been converted to height above sea level by the EGM2008 geoid.

Attitude of the aircraft during flight was determined by a high-grade iMAR RQH-1004 navigation system, as well as an OXTS integrated MEMS-based navigation system. The iMAR unit was used on the science flights (March 7 and 8), while the OXTS provide attitude on the other flights (the agreement between the two systems were at the ~0.1° level, except for the installation bias ~0.5°). Timing for the final files containing WGS84 coordinates, heights above ellipsoid and msl, and pitch, roll, heading are based on UTC (not GPS time, which is 18 sec ahead of UTC).

Measurements with the iMAR IMU doubled also as an opportunity test for gravity measurements along the some of the flight lines; gravity information will together with existing data improve the geoid, and thus also improve the determination of sea ice thickness from space over ice-covered regions.

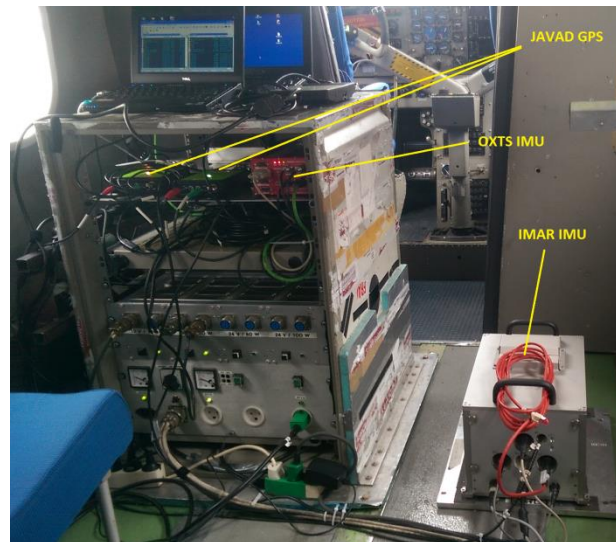


**Figure 2:** The navigation and power rack in CIMREx

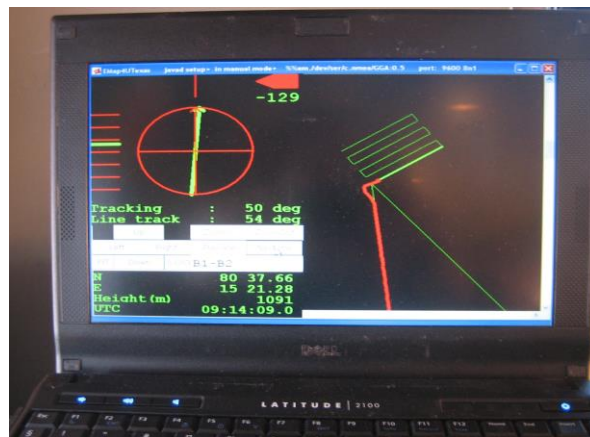


**Figure 3:** Mow-the-lawn real time flight display (separate monitor for the pilots)

### 2.3 Optical and infrared cameras

A thermographic Infratec VarioCAM HDx head 600 camera (Figure 4) was installed in the bay under the HUTRAD radiometer system. The VarioCAM HDx 600 is based on an uncooled microbolometer FPA detector with  $640 \times 480$  IR pixels. It has a wide temperature measuring range that makes it suitable for universal measuring and monitoring tasks, including aerial thermography. It has an industrial-grade lightmetal housing (IP67), which makes operation possible in harsh environments. The camera is powered either by 12 to 24V DC or by an 230V AC adapter. Data is recorded by an industrial mini-PC ICS POC-320. The camera can be remotely operated by a notebook connected by Ethernet (preferred) or WiFi. Characteristics of the camera are given in **Table 2**.

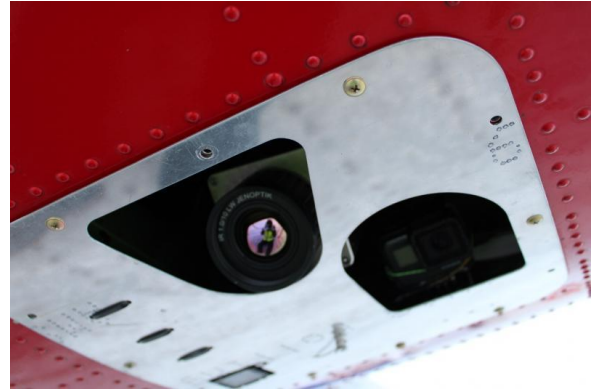


**Figure 4:** left: Infratec VarioCAM HDx head 600 infrared camera (Credit: Infratec). Right: installation in Twin Otter together with GoPro (Credit: Sampo Salo)

**Table 2:** Main characteristics of the VarioCAM HDx head 600 infrared camera.

Spectral range	(7.5 ... 14) $\mu\text{m}$	
Detector	Uncooled microbolometer focal-plane array	
Detector format (IR pixels)	(640 $\times$ 480)	
Temperature measuring range	(-40 ... 600) $^{\circ}\text{C}$	
Measurement accuracy	$\pm 2$ $^{\circ}\text{C}$ or $\pm 2\%$	
Temperature resolution (@ 30 $^{\circ}\text{C}$ )	Up to 0.03 K	
Frame rate	Full-frame: 30 Hz (640 $\times$ 480), sub-frame: 60 Hz (384 $\times$ 288)	
Lens		<i>Alternative:</i>
Focal length	10 mm	20 mm
Field of view	57.1 $^{\circ}$ $\times$ 44.4 $^{\circ}$	30.4 $^{\circ}$ $\times$ 23.1 $^{\circ}$
Focus	Motor-driven, automatic or manual, accurately adjustable	
Dynamic range	16 bit	
Power supply	AC adapter, or (12 ... 24) V DC, or PoE	
Storage and operation temperature	(-40 ... 70) $^{\circ}\text{C}$ , (-25 ... 55) $^{\circ}\text{C}$	
Protection degree	IP67, IEC 60529	
Impact strength, vibration resistance in operation	25 G (IEC 68 - 2 - 29), 2 G (IEC 68 - 2 - 6)	
Dimensions, weight	(221 $\times$ 90 $\times$ 94) mm, 1.15 kg	
Further functions	Camera internal emissivity correction, shutter free operation	

Several GoPro cameras were operated during the transfer and science flights. Cameras were mounted primarily in an opening of the cargo bay floor of the Twin-Otter aircraft, just below the HUTRAD instrument. Cameras were installed at both slant angles and in a nadir looking configuration. Due to the cold conditions (down to -28 $^{\circ}\text{C}$ ) some freeze-up of the bottom-mounted GoPro-cameras happened (especially the newer GoPro7 unit turned out to be very sensitive to cold), so slant photography from inside the cabin was also done on some occasions.

### 3 Flight operations

A summary of the conducted flight operations is given in Table 3. Compared to the Campaign Implementation Plan, the CIMREx schedule was delayed by one week to allow for finalization of the HUTRAD refurbishment. Installations at Akureyri airport began on February 28. After installation and ground performance checks of all instruments, the system was ready for a test flight on March 3. During the test flight, in particular the capability of the HUTRAD system to maintain receiver internal temperatures was assessed. Transfer to Svalbard was performed in three legs from Mar 4 to Mar 5. After bad weather on Mar 6, two science flights (test sites B and C) were sampled on Mar 7, with a landing for refuelling and calibration between the flights. The last designated test site (test site D) was sampled on Mar 8. After prohibitive flying weather on Mar 9, the transfer flight back to Akureyri (two legs) was done on Mar 10.

**Table 3:** Summary of CIMREx flight operations.

<i>Date</i>	<i>Description</i>	<i>Take off</i>	<i>Landing</i>	<i>Airborne</i>	<i>Block time</i>	<i>Sum</i>	<i>Comments</i>
Mar 3	Test flight	16:38	17:09	0:31	0:41	0:41	AEY
Mar 4	Transfer flight 1	10:47	13:02	2:15	2:25	6:12	AEY-CNP
	Transfer flight 2	14:12	17:08	2:56	3:06		CNP-DMH
Mar 5	Transfer flight 3	12:12	15:29	3:17	3:27	9:39	DMH-LYR
Mar 7	Science flight 1	08:04	11:44	3:40	3:50	17:48	Test site B
	Science flight 2	13:16	17:25	4:09	4:19		Test site C
Mar 8	Science flight 3	09:36	12:45	3:09	3:19	21:07	Test site D
Mar 10	Transfer flight 4	08:06	13:21	5:15	5:25	29:10	LYR-CNP (no meas)
		14:04	16:32	2:28	2:38		CNP-AEY

**Figure 5** depicts all flight transects including the transfer flight to and from Svalbard. An original plan to make more profiles across the NE Greenland marginal ice zone had to be modified, due to daylight constraints for VFR flights to Danmarkshavn weather station (DMH). Also, for the return flight from Svalbard to Constable Point airport (CNP), no measurements were possible due to the extremely long transit, necessitated by recent Schengen border control issues. Measurements were resumed for the last leg from Constable Point to Akureyri.

**Figure 6** depicts the tracks sampled during the three main science flights. The science flights had the primary objectives to collect relatively low (320 m) profiles over sea ice and higher level (1050 m) profiles in dedicated “mow-the-lawn” patterns, where an equidistant ~20 km long line pattern were flown both in “forward” and “backward” directions, with a line spacing (~2.5 km) designed to give optimal coverage of brightness temperature variations over the pattern. The mow-the-lawn areas were selected to have a different degree of open water and floes of first year (FY) or multi-year (MY) ice.



Figure 5: CIMREX-2019 flight tracks

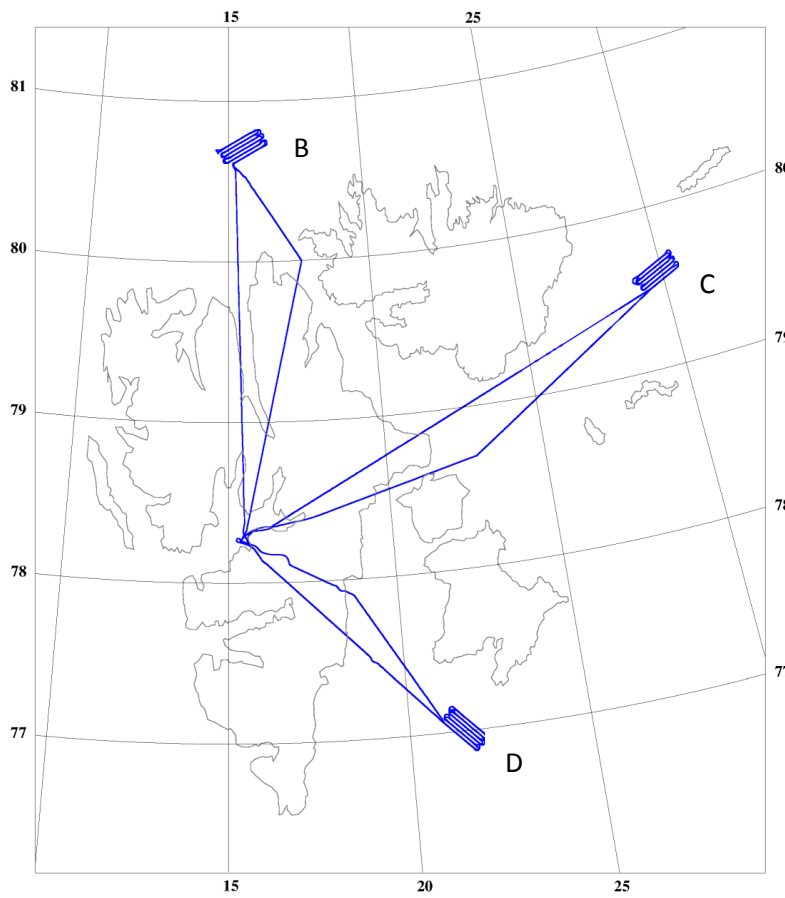


Figure 6: Svalbard flight tracks March 7-8. The test sites were labeled B, C and D.

## 4 Data Products

### 4.1 HUTRAD

#### 4.1.1 Raw data files

Raw data files contain the HUTRAD raw detector counts (Hz), receiver internal temperatures (°C), power supply to temperature control Peltier elements (% of max cooling/heating) and timing of manual markers. The data, in ascii format, are not a part of the CIMREx data package but can be provided by separate request. Note that these data include data also from instrument calibrations, which are excluded from the L1 product files.

#### 4.1.2 HUTRAD L1 brightness temperatures

The calibrated and georeferenced HUTRAD brightness temperatures are provided in .xlsx -files. In addition to the three science flights, data are provided for Transfer flights 1-4. Data from each flight was calibrated using a two-point calibration performed either before or after each flight. **Table 4** provides a summary of the assembled L1 brightness temperature data files.

**Table 4:** Summary of HUTRAD L1 data files

Datafile name	Flight	Size (Mb)	Comments
20190304_hutrad_xferflight1.xlsx	Transfer 1	5.3	Mar 4 / Akureyri
20190304_hutrad_xferflight2.xlsx	Transfer 2	7.5	Mar 4 / Akureyri
20190305_hutrad_xferflight3.xlsx	Transfer 3	8.5	Mar 5 / Longyearbyen
20190310_hutrad_xferflight4.xlsx	Transfer 4	19.5	Mar 10 / Akureyri
20190307_hutrad_scienceflight1.xlsx	Science 1	9.6	Mar 7 (noon) / Longyearbyen
20190307_hutrad_scienceflight2.xlsx	Science 2	11.5	Mar 7 (evening) / Longyearbyen
20190308_hutrad_scienceflight3.xlsx	Science 3	8.8	Mar 8 (evening) / Longyearbyen

Each data sample contains the integrated observations collected during the defined integration time (default 0.5 seconds), calculated to brightness temperature using calibration parameters. In addition the measured internal temperatures of radiometer receivers are provided. Each data sample is provided with a timestamp, associated aircraft location (lat, lon, altitude), aircraft attitude (yaw, pitch, roll), the calculated footprint location (lat, lon) on the Earth surface as well as the footprint size (major and semi-major axis of resolution cell ellipse corresponding to 9 dB FOV) and orientation. **Table 5** describes the data format of the files, which applies to all provided HUTRAD data. Note that while brightness temperatures and location data are given according to the applied integration time, data for receiver temperatures (columns 19 to 30) are available only for times when the temperatures were sampled (every 10 seconds).

**Table 5:** Content of HUTRAD L1 data columns.

Column	Description	Unit
1	timestamp as time of day (hours) of given date	h.ddddd
2	IFOV centre lat	NN.dddd
3	IFOV centre lon	EE.ddddd
4	IFOV major axis orientation from north	deg
5	IFOV centrepoint local incidence angle	deg
6	IFOV polarization rotation from nominal	deg
7	IFOV (9dB) ellipse semi-major axis @ 6.8 GHz	m
8	IFOV (9dB) ellipse semi-minor axis @ 6.8 GHz	m
9	IFOV (9dB) ellipse semi-major axis @ 10.65 GHz	m
10	IFOV (9dB) ellipse semi-minor axis @ 10.65 GHz	m
11	IFOV (9dB) ellipse semi-major axis @ 18.7 GHz	m
12	IFOV (9dB) ellipse semi-minor axis @ 18.7 GHz	m
13	Tb channel 1 (6.8 GHz) H pol	K
14	Tb channel 1 (6.8 GHz) V pol	K
15	Tb channel 2 (10.65 GHz) H pol	K
16	Tb channel 2 (10.65 GHz) V pol	K
17	Tb channel 3 (18.7 GHz) H pol	K
18	Tb channel 3 (18.7 GHz) V pol	K
19	6.8 GHz receiver internal temperature 0	°C
20	6.8 GHz receiver internal temperature 1	°C
21	6.8 GHz receiver internal temperature 2	°C
22	6.8 GHz receiver internal temperature 3	°C
23	10.65 GHz receiver internal temperature 0	°C
24	10.65 GHz receiver internal temperature 1	°C
25	10.65 GHz receiver internal temperature 2	°C
26	10.65 GHz receiver internal temperature 3	°C
27	18.7 GHz receiver internal temperature 0	°C
28	18.7 GHz receiver internal temperature 1	°C
29	18.7 GHz receiver internal temperature 2	°C
30	18.7 GHz receiver internal temperature 3	°C
31	aircraft location lat	NN.dddd
32	aircraft location lon	EE.ddddd
33	aircraft height above sea level	m
34	aircraft yaw	deg
35	aircraft pitch	deg
36	aircraft roll	deg
37	marker	-

The information on HUTRAD FOV orientation and footprint size, calculated based on the simulated 9 dB beamwidth, can be applied for data visualization and estimation of the area on the target area represented by each given brightness temperature reading. Figure 7 depicts a visualization of the HUTRAD 18.7 GHz vertically and horizontally polarized brightness temperatures measured during science flight 3 on March 8, 2019.

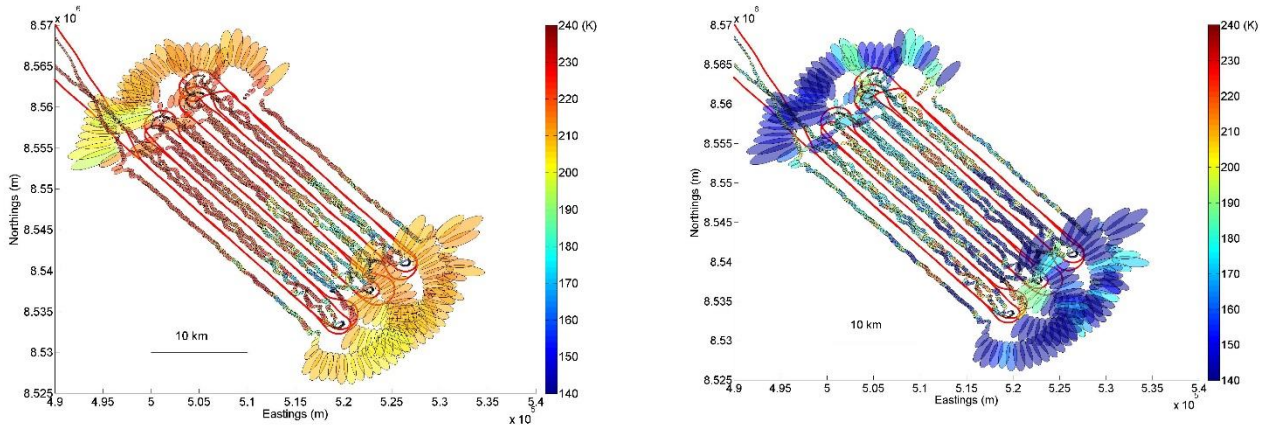


**Figure 7:** HUTRAD 18.7 GHz, vertical (left) and horizontal (right) polarization data over test area of Science flight 3.

#### 4.1.3 HUTRAD calibration

During CIMREx, the absolute calibration of the HUTRAD system was performed using a two-point calibration. Absorptive material at ambient temperature was used to cover the entire aperture of antennas to create a ‘hot’ calibration target. The ‘cold target’ was achieved using similar material cooled to  $\sim 77$  K using liquid nitrogen. In practice, metal containers with microwave absorbing material on the bottom surface were applied – these were lifted manually in front of the radiometer antenna aperture (**Figure 8**) and kept in place for a sufficient time to achieve a reliable calibration measurement; during CIMREx, a one minute calibration time was applied. The physical temperature of the ‘hot’ target was measured using a precision thermometer, and assuming the absorber acts as a perfect blackbody, this gives directly the brightness temperature. Similarly, the ‘cold’ target is assumed to be at the boiling point temperature of liquid nitrogen (77 K under nominal pressure conditions).



**Figure 8:** Calibration of HUTRAD receiver using a calibration target (metal container containing absorptive material) in front of the antenna aperture. Two targets are used; one is kept at ambient temperature, the other is cooled with liquid nitrogen prior to calibration.

The HUTRAD system does not include a possibility for internal receiver calibration; therefore, emphasis has been placed on the thermal stabilization of the receivers in order to minimize receiver gain and noise temperature variations in between calibrations. In order to verify the stability of the instrument, calibrations have been performed optimally before and after a science flight. In previous studies (e.g. Lemmetyinen et al., 2009; Lemmetyinen et al., 2015) the absolute accuracy, estimated from pre- and post flight calibrations, was estimated to be better than 2 K for the low frequency systems. During CIMREx, a full calibration with the ‘cold’ target was not possible on every occasion, due to logistical difficulties in arranging liquid nitrogen in remote locations. On those occasions, a verification of instrument stability was made using the ‘hot’ calibration load. **Table 6** summarizes the calibrations (with and without LN2) made during CIMREx. The flight to which each calibration is applicable is indicated; while it is technically possible to apply any calibration parameters to any flight data as long as receiver temperatures have been identical, it is preferred to use unique parameters for each mission due to small changes in the final stabilization temperature after each warm-up of the receivers. The exception is Transfer flight 4, when LN2 calibration was not possible; calibration parameters from Mar 8 are applied.

After verification of calibrations made on Mar 5 and Mar 6, a notable amount of RFI was found on the 6.8 GHz observations. This possibly has possibly affected calibration accuracy at 6.8 GHz on those dates, as well as the calibration in the morning of Mar 7 before Science flight 1. After landing from Science flight 1, the aircraft orientation on the platform of Longyearbyen airport was altered by 180 degrees (radiometers facing North instead of South). The level of RFI was seen to decrease notably (to below detection level). The possible source of RFI were KSAT and EISCAT installations to the South of Longyearbyen airport; significant RFI peaks at 6.8 GHz appear also in the flight data in the vicinity of the airport when facing South.

Another feature detected in post processing of calibration parameters was that parameters for 18.7 GHz, H-pol, were out of the expected range for the morning calibrations made on Mar 7 and Mar 8. It is possible this is due to insufficient heating and stabilization times, which has affected some components of the 18.7 GHz receiver. Pending further investigation, it is recommended the morning calibration parameters are not to be applied for the 18.7 GHz receiver. Consequently, the present L1 data have been calibrated with the Mar 7 noon parameters (Science flight 1), the average of noon and evening parameters (Science flight 2) and the evening parameters of Mar 8 (Science flight 3). As a precaution, the morning parameters were not applied for any receiver, although calibration parameters were within expected bounds for all other channels than 18.7 GHz H-pol.

**Table 6:** Summary of HUTRAD calibrations and instrument verifications

Date / time of calibration	Location	Applicable flight	LN2 (yes/no)	Comments
Mar 4	Akureyri	Transfer 1 (Transfer 2)	yes	Calibration parameters used also for transfer 2 due to lack of later LN2 calibration
Mar 4	Constable Point	Transfer 1, Transfer 2	no	
Mar 4	Danmarkshavn	Transfer 2	no	
Mar 5	Danmarkshavn	Transfer 3	no	
Mar 5	Longyearbyen	Transfer 3	yes	RFI detected at 6 GHz
Mar 6	Longyearbyen	NA	yes	Multiple calibrations at different receiver temperatures
Mar 7 (morning)	Longyearbyen	Science 1	yes	Calibration parameters at 18.7 GHz H-pol out of expected range; possible insufficient stabilization time
Mar 7 (noon)	Longyearbyen	Science 1, Science 2	yes	
Mar 7 (evening)	Longyearbyen	Science 2	yes	
Mar 8 (morning)	Longyearbyen	Science 3	yes	Calibration parameters at 18.7 GHz H-pol out of expected range; possible insufficient stabilization time
Mar 8 (evening)	Longyearbyen	Science 3	yes	
Mar 10	Danmarkshavn	Transfer 4	no	No possibility for LN2 calibration upon departure
Mar 10	Akureyri	Transfer 4	no	No possibility for LN2 calibration upon departure

## 4.2 Infrared camera material

The IR camera was installed on a metal plate in the hatch below HUTRAD together with a GoPro camera (Section 4.3). The same 55° incidence angle as for HUTRAD was used. The larger opening angle (57° x 44°) of the IR camera compared to HUTRAD allowed the HUTRAD footprints of all frequencies to always stay within the IR camera imagery.

An internal non-uniformity-calibration (NUC) was used for the IR camera in an interval of 5 minutes during the Flight. The long interval was chosen because this calibration takes about one second to perform during which the recording stops. The data was acquired at a rate of 30Hz to have a significant overlap at all flight heights. This was supposed to be used for a later correction of the data set for inferring the incidence angle dependency of the surface and improving sharpness of the image using many acquisitions of the same temperature regime borders. To reduce the size and processing time of the data set only every 60th image was converted into the final distribution format. The output is comma separated values starting at line 23 with some metadata before. The GPS data as well as the height is inside the file as well. However, the GPS time is missing in the CSV files while the mentioned time is the local time set in the acquisition computer. The clock has a strong time drift of about 2s per day, thus the time offset between the HUTRAD data file and the CSV files is mentioned in the table below.

During the first two transfer flight the camera was by mistake focused on a fixed distance of 2 m which, due to the large sensor size, resulted in a quite blurry image where no contours of ice can be identified. The use of this data is restricted to overall average temperature of about  $1.06 \times \text{flight height}$ . However, this information is not extracted.

The data taken on the three science flights including the entire mow-the-lawn patterns worked flawlessly. On the third transfer flight some clouds contaminated the data during about one third of the flight. The fourth transfer flight was entirely cloud covered.

**Table 7:** Summary of collected infrared camera material

Date	Flight Name	File Name	Duration (min)	Size (GB)	Comment ,time offset (to)
Mar 3	-	Not used	52	-	Unfocused,105s
Mar 4	Transfer 1/2	Not used	380	-	Unfocused,107s
Mar 5	Transfer 3	IR_T3.tar.gz	200	2.6	,109s
Mar 7	Science 1	IR_S1.tar.gz	229	3.3	,113s
Mar 7	Science 2	IR_S2.tar.gz	182	2.4	,113s
Mar 8	Science 3	IR_S3.tar.gz	172	2.4	,115s
Mar 10	Transfer 4	IR_T4.tar.gz	165	2.0	Mainly cloud covered, 119s



**Figure 9:** Installation of infrared VarioCAM (top) and visual GoPro cameras on a metal plate, which is installed in the hatch below HUTRAD.

### 4.3 Video camera material

The CIMREx campaign visual imagery was done use GoPro3 and GoPro7 cameras, doing nadir and slant imagery from the nadir hatch below the HUTRAD. Unfortunately the very cold conditions froze up the cameras in many instances, in spite of being turned on continuously 24/7. Especially the new GoPro7 unit turned out to be close to useless under the Arctic conditions, a surprise since the GoPro3 has worked fine on earlier CryoVEx campaigns in the north. A Garmin unit was purchased an alternative camera in Svalbard, and mounted slant-looking inside the cabin. The table below shows the acquired data, at either 5 sec (most flights) or 2 sec (initially). *Note that the image acquisition time is given in the jpg-file info, not in the file name (which is download time; due to Win10 conventions).*

The infrared camera (InfraTec VarioCAM with Irbis3 software; see section 4.2) supplied by University of Bremen functioned well during the campaign, but was unfortunately out of focus on the first two Greenland legs. The infrared camera was time-tagged with GPS, and should be used as a reference for the visual imagery (which was only approximately set to UTC). The table below shows the acquired data.

**Table 8: Overview of visual and IR camera operations.**

<i>Flight day</i>	<i>Nadir</i>	<i>Slant visual</i>	<i>Slant cabin</i>	<i>Slant infrared</i>
MAR 3 (test flt)	GoPro3	GoPro7	N/A	ok, out of focus
MAR 4 (Greenland)	GoPro3	GoPro7 (stopped last hr)	N/A	ok, out of focus
MAR 5 (Fram Strait)	None (frozen)	None	Limited Canon	ok
MAR7 (N and NE flts)	GoPro3	GoPro7 (froze)	Garmin, 2 <sup>nd</sup> flt	ok
MAR8 (SE flight)	GoPro3	Garmin	GoPro7	ok
MAR10 (transit back)	GoPro3	N/A	GoPro7	only last leg

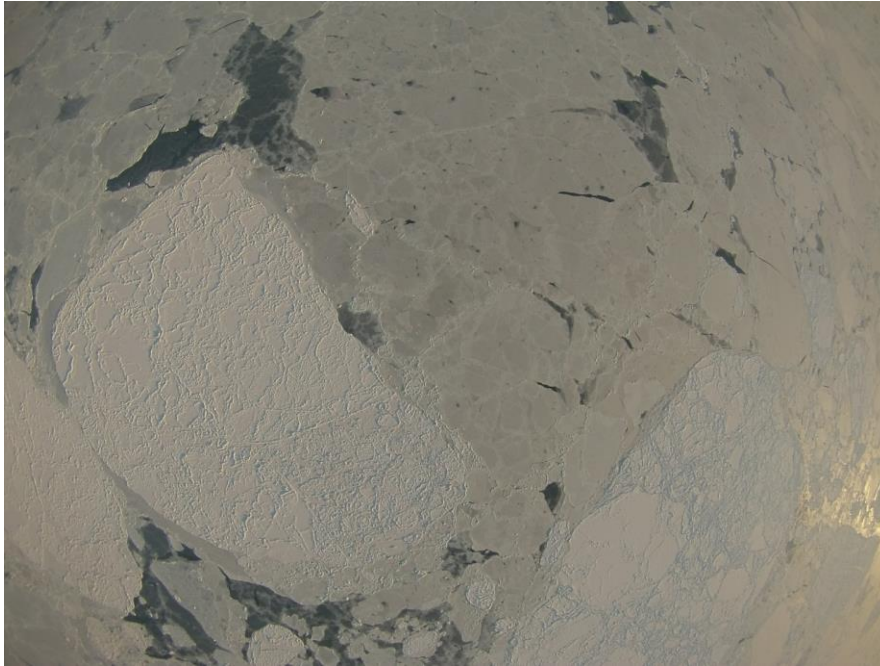


**Figure 10:** Example of GoPro nadir imagery, Svalbard SE flight (MAR8 13:39:50)

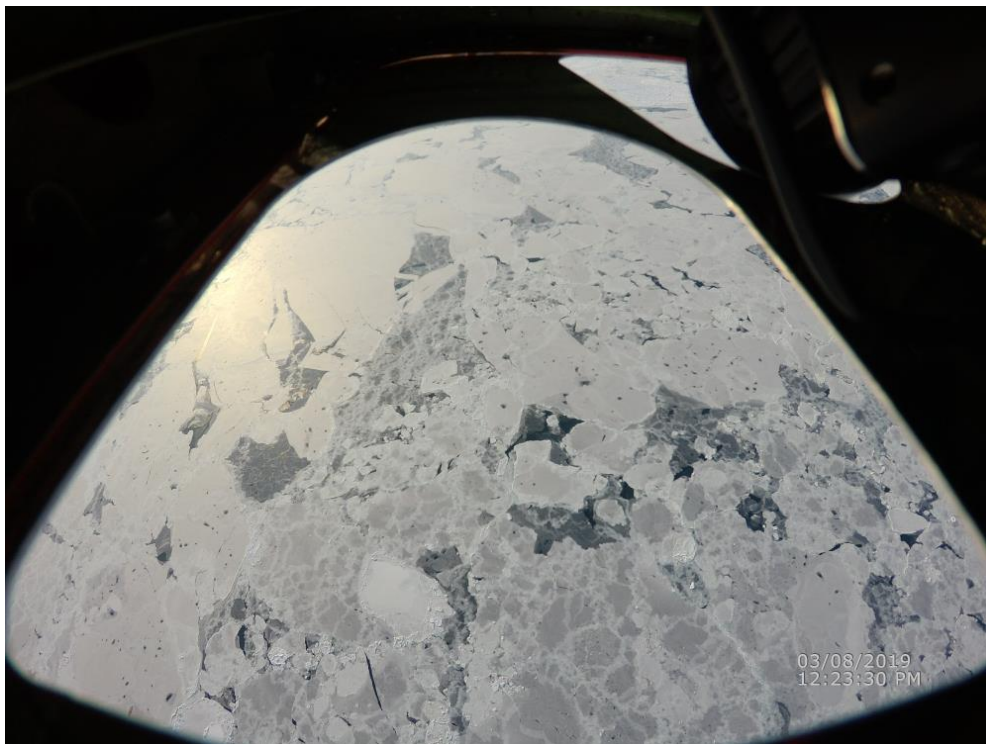


**Figure 11:** Example of slant imagery, hole mounted GARMIN



**Figure 12:** Example of slant-looking imagery from cabin, SE flight

## 5 References

- Lemmetyinen J., C. Derksen, J. Pulliainen, W. Strapp, P. Toose, A. Walker, S. Tauriainen, J. Pihlflyckt, J-P. Kärnä, and M. Hallikainen, 2009. A comparison of airborne microwave brightness temperatures and snowpack properties across the boreal forests of Finland and western Canada. *IEEE Trans. Geosci. Remote Sens.*, 47(3): 965-978
- Lemmetyinen, J., Derksen, C., Toose, P., Proksch, M., Pulliainen, J., Kontu, A., Rautiainen, K., Seppänen, J., and Hallikainen, M., 2015. Simulating seasonally and spatially varying snow cover brightness temperature using HUT snow emission model and retrieval of a microwave effective grain size. *Remote Sens. Environ.*, 156, 71-95.